ABSTRACT

Title of Document: IMPACT OF LAND SURFACE VEGETATION CHANGE OVER THE LA PLATA BASIN ON THE REGIONAL CLIMATIC ENVIRONMENT: A STUDY USING CONVENTIONAL LAND-COVER/LAND-USE AND NEWLY DEVELOPED ECOSYSTEM FUNCTIONAL TYPES

Seung-Jae Lee, Doctor of Philosophy, 2010

Directed By: Professor E. Hugo Berbery
Department of Atmospheric and Oceanic Science

Naturally occurring or human induced changes in land surface vegetation have been recognized as one of the important factors influencing climate change. The La Plata Basin in South America has experienced significant changes in structural land-cover/land-use types, and those changes can involve changes in the surface physical properties such as albedo and roughness length, evapotranspiration, infiltration, and water storage eventually affecting the development of precipitation and the hydroclimate of the basin.

In this study, the Weather Research and Forecast (WRF) modeling system was employed to investigate the role of changing land surface conditions in the La Plata Basin. For this purpose, ensembles of seasonal simulations were prepared for a control case and two extreme land cover scenarios: the first one assumes an expansion of the agricultural activities and the second one assumes a “natural” vegetation cover where no croplands are present.

An extreme anthropogenic land-cover change -simulating an extensive agricultural practice- implies that the northern part of the basin, where croplands replace forests and savannah, would experience an overall increase in albedo and reduced surface friction. The two changes lead to a reduction of sensible heat and surface temperature, and a somewhat higher evapotranspiration due to decreased stomatal resistance and stronger near-surface winds. The effect on sensible heat seems to dominate and leads to a reduction in convective instability. The stronger low level winds due to reduced friction also imply a larger amount of moisture advected out of the basin, and thus resulting in reduced moisture flux convergence (MFC) within the basin. The two effects, increased stability and reduced MFC, result in a reduction of precipitation. On the other hand, the southern part of the basin exhibits the opposite behavior, as crops would replace grasslands, resulting in reduced albedo, a slight increase of surface temperature and increased precipitation. Notably, the results are not strictly local, as advective processes tend to modify the circulation and precipitation patterns downstream over the South Atlantic Ocean.

A newly developed land surface classification, so-called Ecosystem Functional Types (EFTs, systems that share homogeneous energy and mass exchanges with the atmosphere), is implemented in the WRF model to explore its usefulness in regional climate simulations of surface and atmospheric variables. Results show that use of the EFT data improves the climate simulation of 2-m temperature and precipitation, making EFTs a good alternative to land cover types in numerical climate models. An additional advantage of EFTs is that they can be calculated on a yearly basis, thus representing the interannual variability of the surface states. During dry years the 2-m temperature and 10-m

wind are more sensitive to changes in EFTs, while during wet years the sensitivity is larger for the 2-m water vapor mixing ratio, convective available potential energy, vertically-integrated moisture fluxes and surface precipitation. This indicates that the impact of land-cover and land-use changes on the climate of the LPB is dependent not only on the wetness of the year, but also on the meteorological or climate variables. Comparisons with observations show that the simulated precipitation difference induced by EFT changes resembles the overall pattern of observed precipitation changes for those same years over the LPB. In the case of the 2-m temperature, the simulated changes due to EFT changes are similar to the observed changes in the eastern part and the southern part of the basin (especially in Uruguay), where the strongest EFT changes occurred.

IMPACT OF LAND SURFACE VEGETATION CHANGE OVER THE LA PLATA BASIN ON THE REGIONAL CLIMATIC ENVIRONMENT: A STUDY USING CONVENTIONAL LAND-COVER/LAND-USE AND NEWLY DEVELOPED ECOSYSTEM FUNCTIONAL TYPES

By

Seung-Jae Lee

Dissertation submitted to the Faculty of the Graduate School of the
University of Maryland, College Park, in partial fulfillment
of the requirements for the degree of
Doctor of Philosophy
2010

Advisory Committee:
Professor E. Hugo Berbery, Advisor
Professor Eugenia Kalnay, Chair
Professor Rachel Pinker
Professor Ning Zeng
Professor Ralph Dubayah, Dean's Representative

Dedication

Psalms 111:2

“Great are the works of the LORD; they are pondered by all who delight in them.”

1 Corinthians 15:42-44

“So will it be with the resurrection of the dead.
The body that is sown is perishable, it is raised imperishable;
it is sown in dishonor, it is raised in glory;
it is sown in weakness, it is raised in power;
it is sown a natural body, it is raised a spiritual body.
If there is a natural body, there is also a spiritual body.”

Acknowledgements

I thank God for His saving, leading, and guarding me.

I am grateful to God's servants who have prayed for me in the LORD.

I am grateful to my family: my wonderful mother (Jeong-Hee Choi), my beautiful wife (Seung-Hyun Park) and my cute children (Eun-Joo: receiving one blessing after another; Eui-Yoon: leading many to righteousness; and Yeon-Sung: remaining in Him). I would like to thank my wife's family for their support and patience.

I thank Professor Berbery for his academic advice, guidance and support in the University of Maryland, College Park. I will never forget his scholarly character and warm smile.

I thank Professor Kalnay for her continuing encouragement and sincere interest in my study. I could rediscover many things in atmospheric and oceanic sciences thanks to her.

I thank Professors Zeng, Pinker, Dubayah, and Dr. Ruiz-Barradas for their valuable comments on my dissertation.

I thank Professors Hudson, Busalacchi, Zhang, Li, and Nigam for their teaching.

I thank department staff for their kind assistance.

Table of Contents

List of Tables

List of Figures

List of Abbreviations

AVHRR – Advanced Very High Resolution Radiomenter

CCSM – Community Climate System Model

CMAP – CPC Merged Analysis of Precipitation

CRU – Climate Research Unit

ENSO – El Niño / Southern Oscillation

GCM – General Circulation Model

GPCP – Global Precipitation Climatology Project

IC – Initial Condition

IGBP – International Geosphere-Biosphere Program

ITCZ – Inter-Tropical Convergence Zone

LAI – Leaf Area Index

LLJ – Low Level Jet

LULCC – Land Use and Land Cover Change

LPB – La Plata Basin

MCCs – Mesoscale Convective Complexes

MF – Moisture Flux

MFC – Moisture Flux Convergence

MODIS – Moderate Resolution Imaging Spectroradiometer

NCAR – National Center for Atmospheric Research

NDVI – Normalized Difference Vegetation Index

NWP – Numerical Weather Prediction

OMR – Observation-Minus-Reanalysis

PBL – Planetary Boundary Layer

RAMS – Regional Atmospheric Modeling System

RCM – Regional Climate Model

SA – South America

SACZ – South Atlantic Convergence Zone

TRMM – Tropical Rainfall Measurement Mission

USGS – United States Geological Survey

VIMF – Vertically Integrated MF

VIMFC – Vertically Integrated MFC

WRF – Weather Research and Forecast

Chapter 1: Introduction

Land-atmosphere feedbacks are highly dependent on the physical properties of the underlying land cover. The reason is that properties like surface albedo, surface roughness, stomatal resistance, radiation stress, and others, affect the way in which water and energy are exchanged. Changes in land cover and land use thus affect the exchange of momentum, heat, moisture, and other gaseous/aerosol materials between the land and the atmosphere. The amount of water in the atmosphere and returning to the earth's surface, in turn, influences many of the key properties of the land surface. Figure 1.1 presents diverse radiative forcing terms and their impacts on global mean radiation. According to the figure, the albedo modification by land-use changes is known to have slightly negative impact on the global mean radiative flux. However, because global average masks regional signals, regional effects of land-use changes can be positive and even much larger in magnitude. This is one of the major reasons why we should study the impact of land-cover/land-use[1] on a particular region.

The impact of land-use land-cover changes (hereafter referred to as LULCCs) on local, regional and global climate has been studied for several land-type conversions on different regions and spatiotemporal scales (e.g. Pielke et al. 2007, Marland et al. 2003). The size and the geographic location of the area where land cover changes are occurring may determine the extent to which the land cover disturbance affects local, regional and global climate (Marland et al. 2003). Smaller areas (e.g., of the order 10

[1] The terms land-cover and land-use refer to "vegetation, structures, or features that cover the land" and "how land is used by human", respectively (http://www.cara.psu.edu/land/landuseprimer.asp). The present study focuses on the former, and uses a combined term "land-cover/land-use" or "land-use/land-cover".

km) of land cover change can result in changes in the local pattern and intensity of precipitation. In tropical regions, where large thunderstorms are frequent, modification of land cover over areas that are of hundreds of kilometers may yield global impacts (Pielke 2001, Werth and Avissar 2002). Over Amazonia, Nobre et al. (1991) concluded that the effects of deforestation led to a reduction in evapotranspiration and the moisture flux convergence, and consequently on precipitation. Deforestation implies changes in the surface water and energy budgets, but also in the low level circulation (e.g., through changes in the surface roughness) and in the moisture flux convergence, all of which produce shifts in the areas of maximum precipitation rather than on the intensity alone (Hahmann and Dickinson 1997).

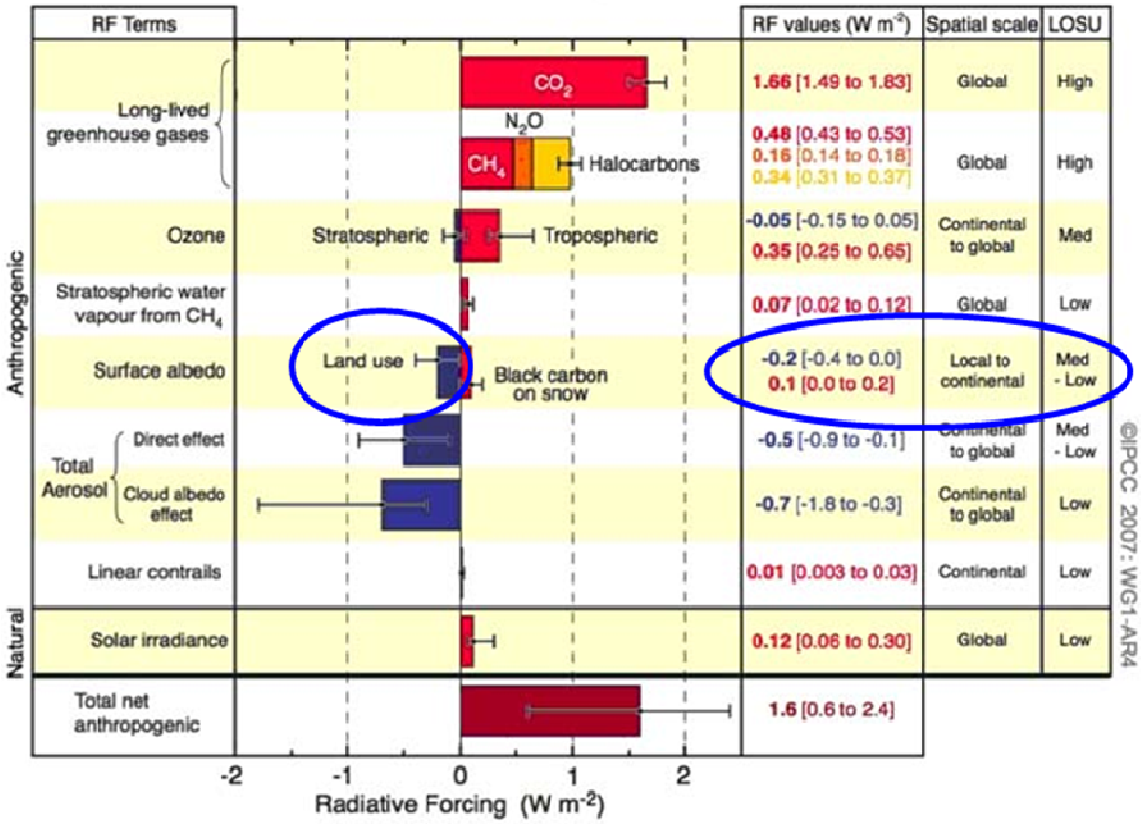

Figure 1.1: Radiative forcing components and their known effects on global mean radiative fluxes (taken from IPCC 2007).

At higher latitudes, like over the U.S. during summer, historical land cover changes produce a strong cooling in the Midwest, and weaker warming towards the Atlantic region (Roy et al. 2003). Weak reductions in precipitation associated with moisture transports are also found in the Midwest. Stohlgren et al. (1998) presented evidence that land use changes in the plains of Colorado influence regional climate and vegetation in adjacent natural areas in the Rocky Mountains, and that increasing irrigated agricultural lands at the expense of grassland and dry cropland may induce a strong cooling surpassing larger-scale temperature changes related with observed increases in greenhouse gases such as CO_2.

The above processes are most relevant for large regions of South America, and have been usually discussed for Amazonia, but not much for the La Plata Basin (LPB, see boundaries in Fig. 1.2). As the second largest basin in South America, the LPB stretches from the subtropics (about 14°S) to middle latitudes (about 38°S). As shown in Figs. 1.2 and 1.3, four subbasins and three large tributary rivers (the Paraná, the Paraguay, and the Uruguay Rivers) make up the whole LPB, each river supplying water resources to surrounding countries (see, e.g., Berbery and Barros 2002).

The Paraná River has its head in the northeast of the LPB and flows southwestward finally arriving at the southern LPB boundary (Fig. 1.3). The Paraguay River starts in the north of the LPB where the world's largest tropical wetland (known as *Pantanal*) is located. It flows southward and joins the Paraná tributary at the southern boundary of the Paraguay subbasin. The Uruguay River starts in the east of the LPB and flows along the boundary between Brazil and Argentina first, and then between Uruguay and Argentina, joining the Paraná tributary at the southern boundary of the LPB.

Only this last portion of the three tributary rivers themselves is called the “La Plata River” (whose Spanish name is “Río de la Plata” meaning “River of Silver”). The La Plata River has an annual-mean discharge at its mouth near Buenos Aires larger than that of the Mississippi (Baethgen et al. 2001). The installed hydropower generating capacity (mostly in the Paraná, a major subbasin) exceeds 20,000 MW, almost double that of the Columbia River basin, which by far has the largest hydropower production among U.S. rivers (Baethgen et al. 2001).

Figure 1.2: The La Plata Basin and its four subbasins.
[Source:
http://www.unesco.org/water/wwap/wwdr/wwdr2/case_studies/img/plata_big.gif]

Figure 1.3: Three large tributary rivers in the LPB.
[Source: http://assets.panda.org/img/original/plata.gif]

Precipitation and other land surface water cycle variables have undergone very large decadal scale changes over the last century in much of the southern part of South America, and within La Plata Basin in particular. These changes, which are well documented, have been as large as 30-40% on the annual means, as shown in Fig. 1.4 (taken from Barros et al. 2000). In comparison with long-term trends in North American precipitation and streamflow, these changes are quite large (e.g. Climate Prediction Center, 2001; Lins and Slack, 1999).

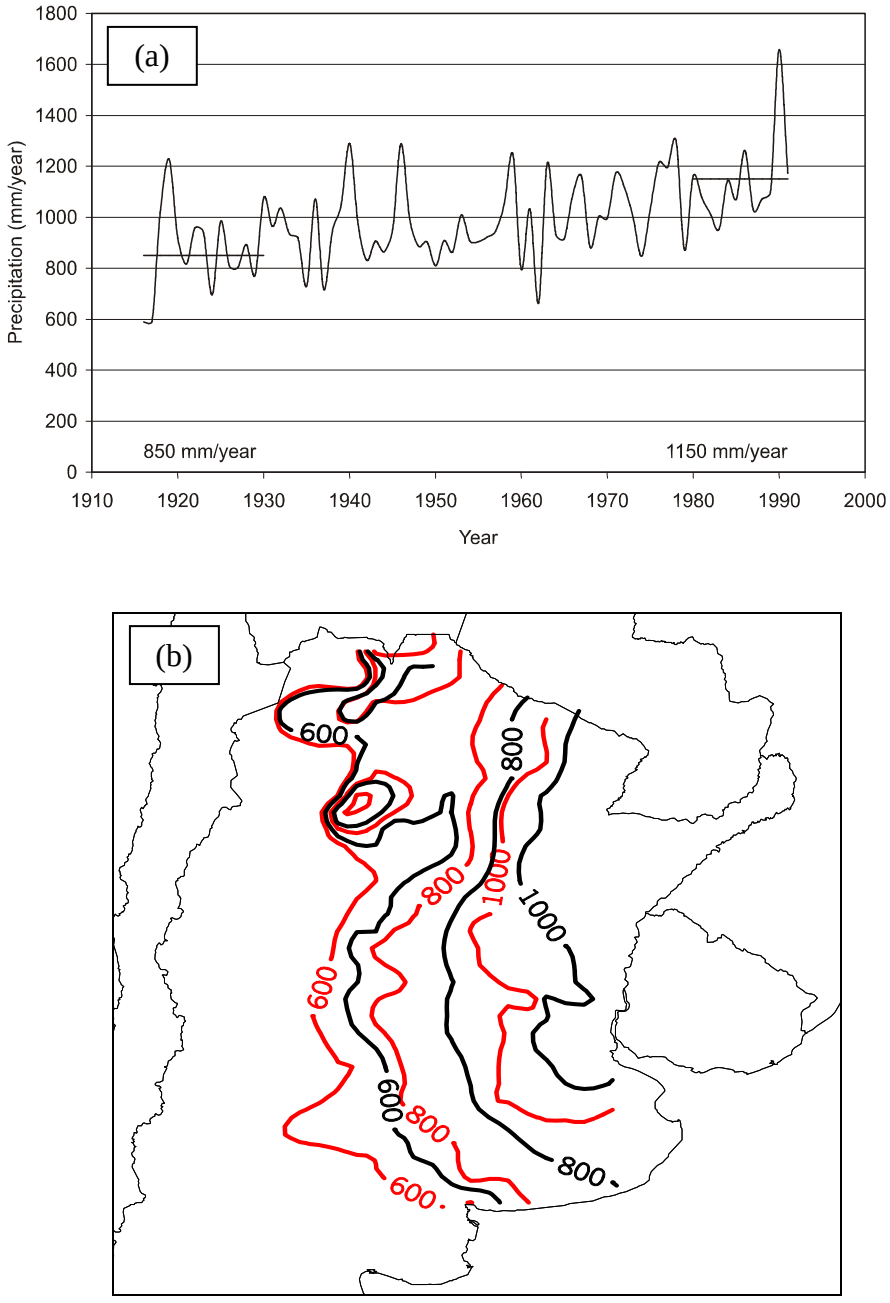

Figure 1.4: (a) Mean annual precipitation in the Humid Pampa; (b) Changes in precipitation from 1950/1969 (black contour) to 1980/1999. Linear precipitation trends 1956-1991 in mm year^{-1} (Barros et al. 2000).

According to Berbery and Barros (2002), interannual and longer time variability of LPB's *streamflow* reveals a high vulnerability of the region to variations in *precipitation*. Table 1.1 taken from Berbery and Barros (2002) shows that small changes in precipitation are amplified in the streamflow signal. If we define the sensitivity of streamflow to basin-averaged precipitation changes as "regional climate elasticity of streamflow", the elasticity was about two from the Table 1.1, indicating that for a given change in precipitation there was a doubling amplification in streamflow (personal communication, Berbery 2007). Table 1.1 also shows that such a high sensitivity was almost unwavering whether analyzed over consecutive years (1998 vs. 1999), interannual scales (El Niño vs. La Niña), or decades (1951-70 vs.1980-99) (Berbery and Barros 2002).

All these things show that the LPB is a subject of interest not only for physical reasons but also for practical ones, and precipitation is a very important variable in the regional climate.

Table 1.1: Basin averaged rainfall rates and river discharge for the La Plata River corresponding to different timescale variability (From Berbery and Barros 2002).

	Rainfall rate (m^3 s^{-1})	Streamflow (m^3 s^{-1})	Evap+Infilt (m^3 s^{-1})
1998	107000	36600	70400
1999	81600	20440	61600
Difference	23 %	44 %	13 %
El Niño	76000	25250	50750
La Niña	71000	21640	49360
Difference	7 %	17 %	3 %
1951-1970	72000	19300	52700
1980-1999	83500	26000	56500
Difference	16 %	35 %	9 %

Chapter 2: Scientific Questions, Hypotheses, and Objectives

The La Plata Basin has experienced considerable land cover change over recent decades. Tucci and Clarke (1998) discussed the intensification of agricultural production and an associated transition from coffee to soybeans and sugarcane in the Upper Paraná basin in Brazil. They report decreases in forested area from 90% to 17% over the four decades from about 1950 to 1990, with the percentage of land use in annual crops increasing from near zero in the early 1960s to almost 60% by 1990. Significant deforestation has also occurred over the last few decades in both the Brazilian and Paraguayan portions of the Paraguay River basin (Baethgen et al. 2001). The forested area in eastern Paraguay decreased from 45% fifty years ago to 15% at the beginning of the 1990s (Baethgen et al. 2001, citing Bozzano and Weik 1992). Moreover, extensive changes in agricultural practices (Paruelo et al. 2005) may have also affected the surface atmosphere exchanges of energy and water. These large changes in land cover can be expected to have major implications for the surface (and perhaps atmospheric) hydrological cycles, and are a major focus of the research agenda of the La Plata Basin (LPB) Regional Hydroclimate Project (Berbery et al. 2005).

There are some regional numerical modeling studies regarding the possible connection between land cover change and hydroclimate in the LPB over longer time period than one month. For instance, Beltrán-Przekurat et al. (2010) showed that changes in near-surface fluxes and temperature depend on the type of land cover conversion and the season. According to their investigation, the general potential effect of agriculture was cooling when the shift was from grasses (photosynthesis pathway C_3) to crops, while warming when the shift was from grasses (photosynthesis pathway C_4), wooded

grasslands or trees to crops. They found a general increase of precipitation for the entire simulation domain with an afforested scenario, and showed that areas of increase and decrease of precipitation were associated with changes in latent heat, roughness length, and areas of moisture convergence. On the other hand, using a hydrological model, Saurral et al. (2008) suggested that the positive trend observed in the Uruguay River streamflow during the second half of the past century should be attributed to increased precipitation, rather than to land cover change. However, because Beltrán-Przekurat et al. (2010) used horizontally small LULCCs and Saurral et al. (2008) did not allow land-atmosphere coupling, the effects of LULCCs on regional climate are still not clear and need to be further investigated over southern South America.

2.1 Scientific questions

Following the premise that precipitation increased in the last thirty years by up to 30-40% over La Plata Basin, perhaps the most important scientific issue associated with the climate and water cycle of La Plata Basin is how variations in precipitation are linked to land-cover and land-use changes. Changes in precipitation can be the result of local feedbacks (e.g., land cover changes/vegetation changes, and related changes in soil moisture) or a response to remote forcings (e.g., sea surface temperature anomalies). Therefore, the overarching scientific questions to be addressed by this research are:

- ***Are there any regional climate responses to land-cover/land-use change over the La Plata Basin? If so, what are the implied mechanisms?***

- ***Are there any better ways to represent land-cover/land-use types and their changes in a regional model?***
- ***What is the importance of land-cover/land-use change effects as related to observed trends in La Plata Basin precipitation?***

2.2 Hypotheses

The overall goal can be addressed based on three basic hypotheses that are presented as possible explanations of the observed changes in precipitation and near-surface temperature.

First, if land-cover/land-use has changed in such a manner as to alter the *reflectivity* and *emissivity* of the surface, then a modification of local surface energy balance and thermodynamic stability should be expected. This hypothesis has another aspect: if changes in land cover took place that changed local surface *roughness length*, then changes in regional atmospheric circulation should be expected. Thus, if local moisture recycling is an important source of precipitable water, then changes in precipitation patterns could also be expected from the two aspects.

Second, it is hypothesized that realistic specification of *land surface characteristics* is important in the numerical model performance, and inaccurate *vegetation information* can give rise to errors in a model simulation of the near-surface variables, the atmospheric boundary layer, and eventually the entire atmosphere.

A null hypothesis is that there is no relationship between land-surface change and pre-

cipitation over the La Plata Basin.

2.3 Specific objectives

The first objective of this study is to setup an efficient *regional-modeling configuration* using the WRF modeling system so that it can be used for subsequent regional climate studies in South America.

The second objective is to assess *the potential impact of the land-cover changes* within LPB on the springtime precipitation climate using idealized extreme land-cover change scenarios. The study aims at understanding the *physical mechanisms* by which local and regional land cover changes give rise to alterations in regional precipitation.

The third objective is to implement *a newly developed land cover classification dataset* that is called “Ecosystem Functional Types (EFTs)” in the WRF modeling system. The EFTs are patches of the land-surface with similar carbon gain dynamics and are based on “functional attributes” of vegetation describing its energy and matter exchange with the overlying atmosphere (Paruelo et al. 2001; Alcaraz-Segura et al. 2009). In this study, the new dataset is incorporated in the WRF modeling system for the first time, and is examined for its utility through comparison with the traditionally used land-cover/land-use dataset.

The fourth objective is to explore *the impact of varying EFTs* on the regional climate over the La Plata Basin for a dry year and a wet year.

2.4 Outline

Chapter 3 describes the model sensitivities to different physical parameterizations and seeks *an optimal combination* of them for realistic precipitation simulation.

Chapter 4 presents the model configuration and evaluation of the model simulations for the period of spring 2002. Chapter 4 discusses results of the model simulations in which *idealized* changes of regional land cover are assumed by modifying model land cover types.

Chapter 5 introduces a new land cover classification (called EFT), implements it into the model and examines its usefulness.

Chapter 6 shows the impact of *historical* EFT changes on the climate of the La Plata Basin.

Chapter 7 summarizes the present study and presents major findings.

Chapter 3: Model Sensitivity Tests

3.1 Introduction

The Weather Research and Forecast (WRF) modeling system (Advanced Research WRF) is a non-hydrostatic and primitive-equation model with state-of-the-art physics options to parameterize subgrid-scale processes and multiple nesting capabilities to increase the resolution over an area of interest (Michalakes et al. 2001). This model has been developed and widely used as a community numerical model, and has been applied in diverse related fields. It is suitable for use in a broad range of applications across scales ranging from meters to thousands of kilometers, and even a global version of the WRF exists. The WRF model is portable and efficient on available parallel computing platforms, and in this chapter the WRF-ARW (version 2.2.1) was used for the numerical simulations.

Since October 2003, the National Center for Atmospheric Research (NCAR) has supported an effort to develop regional climate modeling capability using the WRF model (see information online at www.wrfmodel.org/index.php) and the Community Climate System Model (CCSM) (information online at www.ccsm.ucar.edu/models). The goal is to develop a next-generation community Regional Climate Model (RCM) that can address both downscaling and upscaling issues in climate modeling. As part of the NCAR project, the WRF model has been adapted for simulating regional climate. Seasonal simulations over the United States have shown realistic features, including the low-level jet and diurnal cycle of rainfall in the central states (Leung et al. 2005) and orographic precipitation in the West (Done et al. 2005). A WRF Regional

Climate Modeling Working Group has been established to coordinate RCM research activities (Leung et al. 2006).

3.2 Methodology

The model precipitation is very sensitive to model physical parameterizations. Especially, land surface processes, PBL and cumulus schemes are known to be important in simulation of heavy rainfall events. The best combination of model physical processes for a certain region is not necessarily the best for other regions. Thus, as the first task, this section seeks an appropriate suite of parameterizations for model physical processes suitable for numerical simulations of the springtime precipitation over South America. Diverse numerical experiments were conducted to find an optimal configuration of the model physical processes over the South America. Table 3.1 presents the available options for the optimal model-physics configuration. Our tests were done for surface layer schemes, atmospheric boundary layer schemes, cumulus parameterization schemes, and microphysical schemes. For all simulations, the Noah land surface model (Chen and Dudhia 2001), the Dudhia shortwave radiation (Dudhia 1989) and the RRTM longwave schemes (Mlawer et al. 1997) were used. Only for EXP3, the NOAH LSM model was turned off.

Table 3.1: Numerical experiments on the model sensitivity to various physical parameterization schemes. LSM: Land surface model; SL: Surface layer scheme; PBL: Atmospheric boundary layer scheme; CP: Cumulus parameterization scheme; MP: Microphysical scheme.

Experiment name	LSM	SL	PBL	CP	MP	Remarks
EXP1	NOAH	MO	YSU	BMJ	WSM3	NmYB3
EXP2	NOAH	MO	YSU	KF	WSM3	NmYK3
EXP5	NOAH	MO	YSU	BMJ	WSM6	NmYB6
EXP6	NOAH	MO	YSU	GD	Ferrier	NmYGF
EXP3	Thermal diffusion	MOJ	MYJ	KF	Ferrier	TMMKF
EXP4	NOAH	MOJ	MYJ	BMJ	Ferrier	NMMBF
EXP7	NOAH	MOJ	MYJ	GD	Ferrier	NMMGF
EXP8	NOAH	MOJ	MYJ	KF	Ferrier	NMMKF
EXP9	NOAH	MOJ	MYJ	BMJ	WSM5	NMMB5
EXP10	NOAH	MOJ	MYJ	BMJ	WSM6	NMMB6

MO: Monin-Obukhov scheme (Dyer and Hicks 1970);
MOJ: Monin-Obukhov-Janjic scheme (Janjic 1996, 2002);
YSU: Yonsei University scheme (Hong et al. 2006);
MYJ: Mellor-Yamada-Janjic scheme (Janjic 1990, 1996, 2002);
BMJ: Betts-Miller-Janjic scheme (Janjic 1994, 2000);
KF: Kain-Fritsch 2 scheme (Kain and Fritsch 1990; Kain and Fritsch 1993);
GD: Grell-Devenyi scheme (Grell and Devenyi 2002);
WSM3: WRF Single Moment 3-class scheme (Hong et al. 2004);
WSM6: WRF Single Moment 6-class scheme (Hong and Lim 2006).

For the experiments, the model is run with a single domain on a continental scale. Figure 3.1 presents the domains and a representation of the topography. The Andes mountain range is located along the west coast and its average height is about 4 km. The Brazilian Highlands along the central east coast and the Guiana Highlands near the northern boundary are seen. Relatively low lands are formed among the three high terrain features.

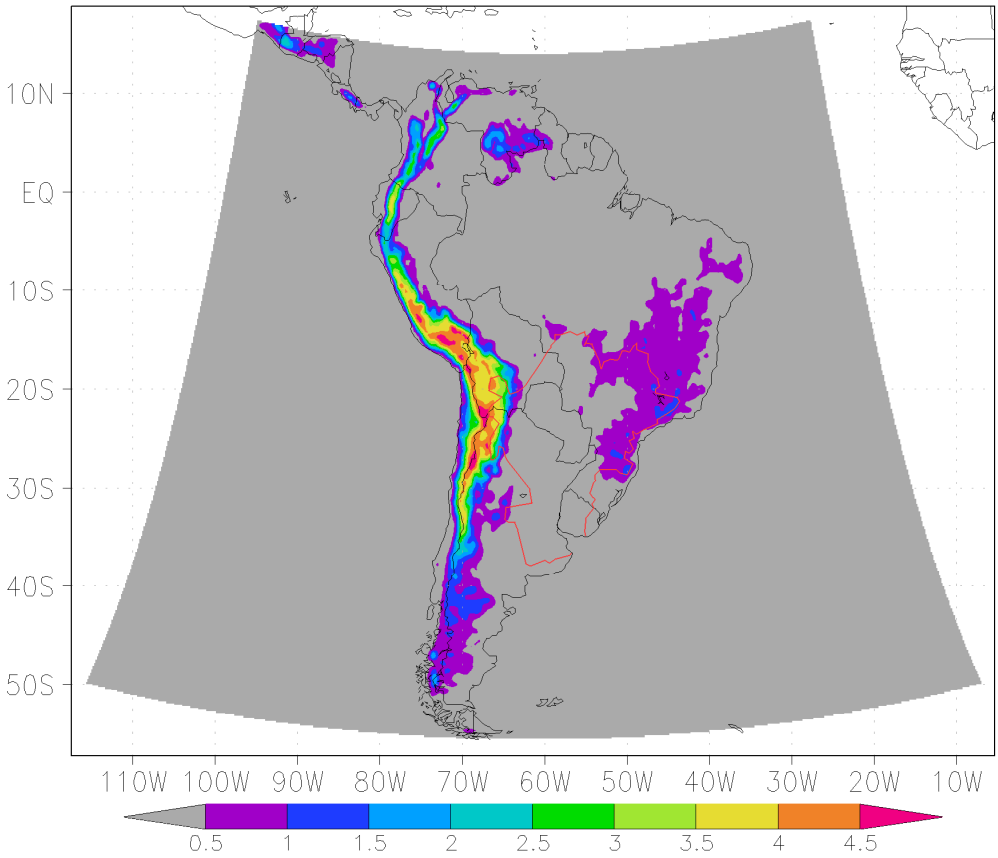

Figure 3.1: The WRF model domains and the La Plata Basin (red line). Model topography is shaded with contour intervals indicated at the bottom and horizontal resolution is 36 km.

All simulations are conducted from 0000 UTC 1 September 2002 to 0000 UTC 30 September 2002, with NCEP/NCAR reanalysis data providing initial and boundary conditions. Grid interval is 36 km with 27 vertical levels from the surface to 10 hPa. NCEP/NCAR Reanalysis data (Kalnay et al. 1996) are used for initial and 6-hourly boundary conditions. A 180-s time step is used. The USGS (United States Geological Survey) terrestrial data sets of 5' resolution were used to be similar to the resolution of the nested model domain. Surface vegetation properties are prescribed following 24 unique USGS land use categories with different surface albedo, emissivity, roughness length, stomatal resistance values assigned to each category. Soil data are prescribed using 16-category USGS dataset and the layers are 0 – 10 cm, 10 – 40 cm,

40 – 100 cm, and 100 – 200 cm from the top down.

To evaluate the model's performance, independent measurements of precipitation were obtained in the form of satellites estimates. TRMM (Tropical Rainfall Measurement Mission) rainfall data, which have better spatial resolution than GPCP (Global Precipitation Climatology Project) and CMAP (CPC Merged Analysis of Precipitation) data were employed. The higher resolution is more proper to verify the simulation results of the relatively high resolution model. The TRMM rainfall data has a higher spatio-temporal resolution of 0.25° x 0.25° than other satellite estimates of precipitation like Xie and Arkin (1997) data and GPROF4.0 dataset (Negri et al. 1994), and in this study three-hourly TRMM products were used.

3.3 An optimal combination of model physical parameterizations

Figure 3.2 shows the monthly averaged precipitation field from TRMM data during September 2002. It exhibits distinct heavy rainfall regions during the period. Regions of interest are identified and denoted by 'R' followed by a number. The LPB is the research interest area and is denoted by the red contour in the figure. R1, 2 and 3 show very strong convective precipitation regions in ITCZ and the most severe rainfall in the model domain. R4 shows rainfall in northwestern South America including Colombia. R5 shows comparatively weak but widespread rainfall over the Amazon Basin in the central Brazil. R7, rainfall in the LPB, is more intense than in R4. R6, 8 and 9 show precipitation over sea and R9 is most intense among them. R6 is associated with the well-known South Atlantic Convergence Zone (SACZ), where cloud or precipitation is generated and elongated along a northwest-southeast oriented swath.

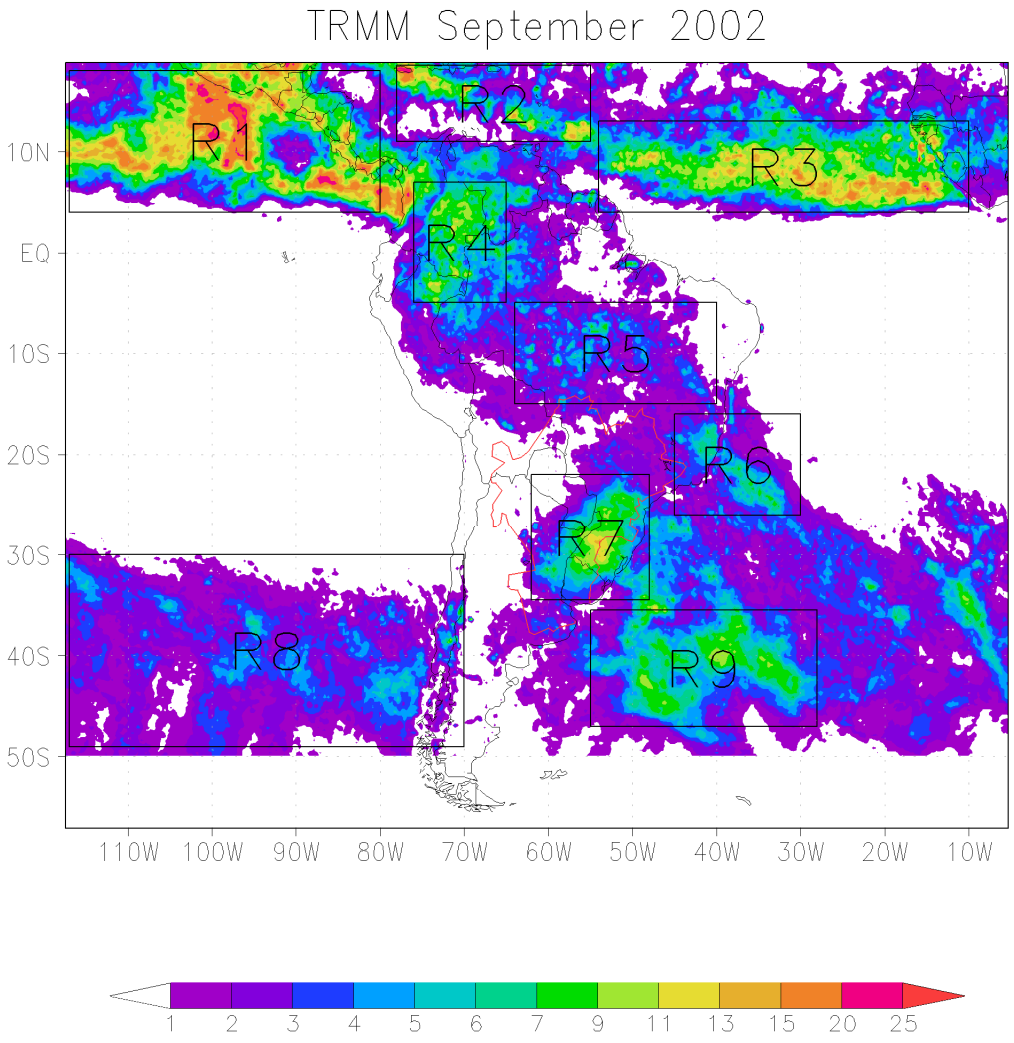

Figure 3.2: Monthly averaged TRMM precipitation (in mm day^{-1}) field for September 2002. The rectangle boxes indicate major rainfall areas and show their location and intensity features. The red line shows La Plata Basin (LPB).

Figure 3.3 presents the horizontal distribution and intensity of the monthly-mean model precipitation simulated by each experiment shown in Table 3.1. It should be noted that R2 is outside the model domain (see e.g., Fig. 3.3c) and it does not appear in all the simulated precipitation fields. Since the LPB is our major interest area, the simulation of rainfall in this area (R7) is especially important. All experiments captured the precipitation signal in the R7, but the rainfall intensity is weaker than the observed. EXP3 among them showed the best performance for rainfall amount in

LPB, but it has no vegetation processes and no snow scheme. It also uses fixed values for a deep-layer average temperature, snow cover and soil moisture, which is a land-use- and season-dependent constant. Thus, this simple 5-layer scheme is not appropriate in this study which requires explicit vegetation effects in the numerical model. EXP3 and 8 underestimated the rainfall amount in the region.

From Fig. 3.3, on the whole, EXP4, 9 and 10 are thought to be good candidates among all the ten simulations. The three experiments have the MYJ PBL and the BMJ cumulus scheme in common. The MYJ scheme predicts turbulent kinetic energy, which is used to obtain eddy diffusivities in the convective boundary layer, while the YSU scheme uses prescribed eddy diffusivity profiles and counter-gradient terms in the situation of convective boundary mixing. The WSM6 scheme was extended from the WSM5 scheme and considers an additional variable (graupel) and ice-phase processes. The WSM6 scheme predicts 6 microphysical variables, while the Ferrier scheme essentially predicts two variables, i.e., water vapor and total condensate. The KF scheme produced lower precipitation than the BMJ, and this might be because the BMJ scheme has been skillfully optimized through tuning work over years at an operational weather forecasting center. More information can be found in Skamarock et al. (2008).

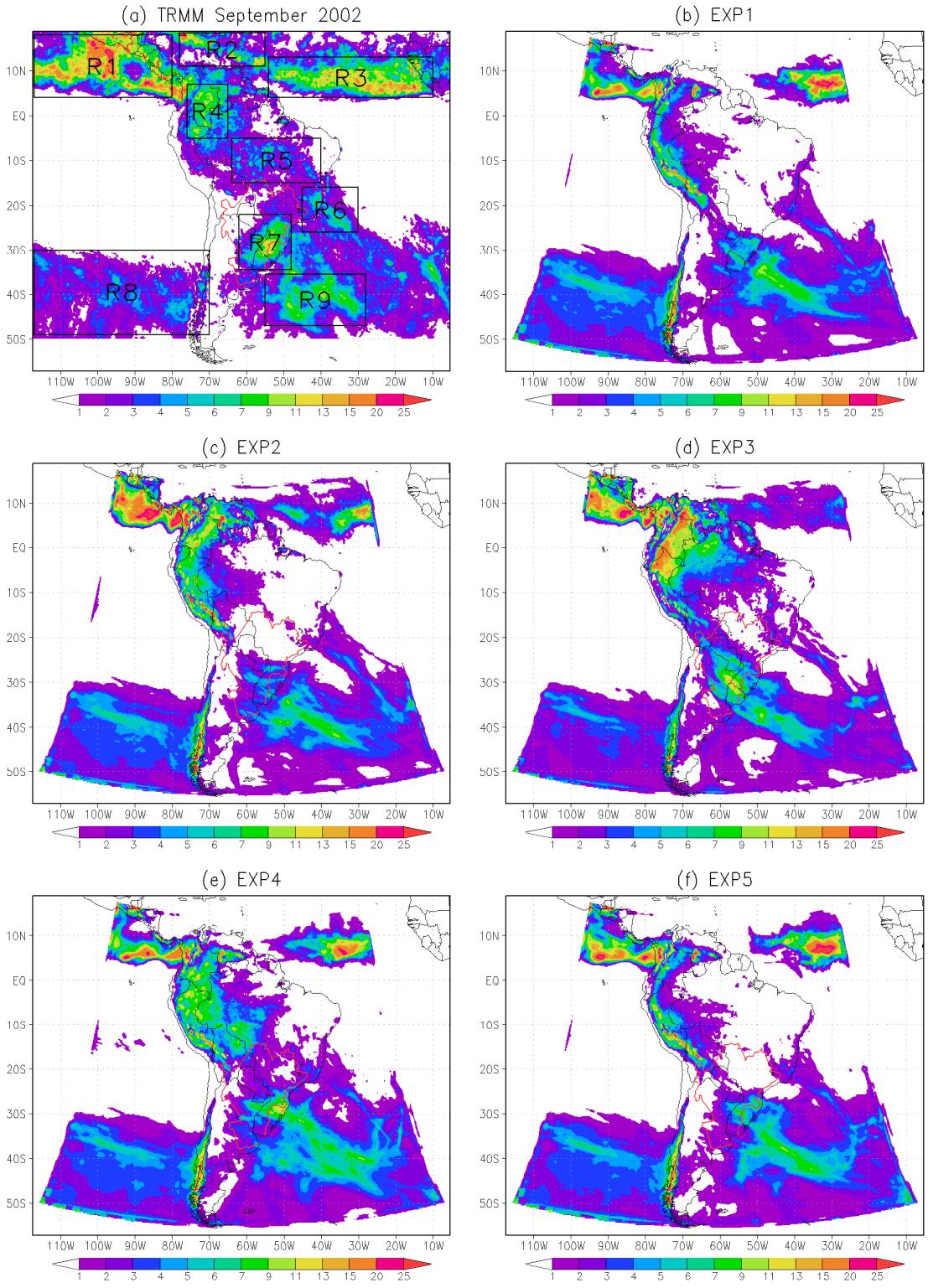

Figure 3.3: Model-simulated total precipitation (in mm day^{-1}) using each experiment shown in Table 3.1.

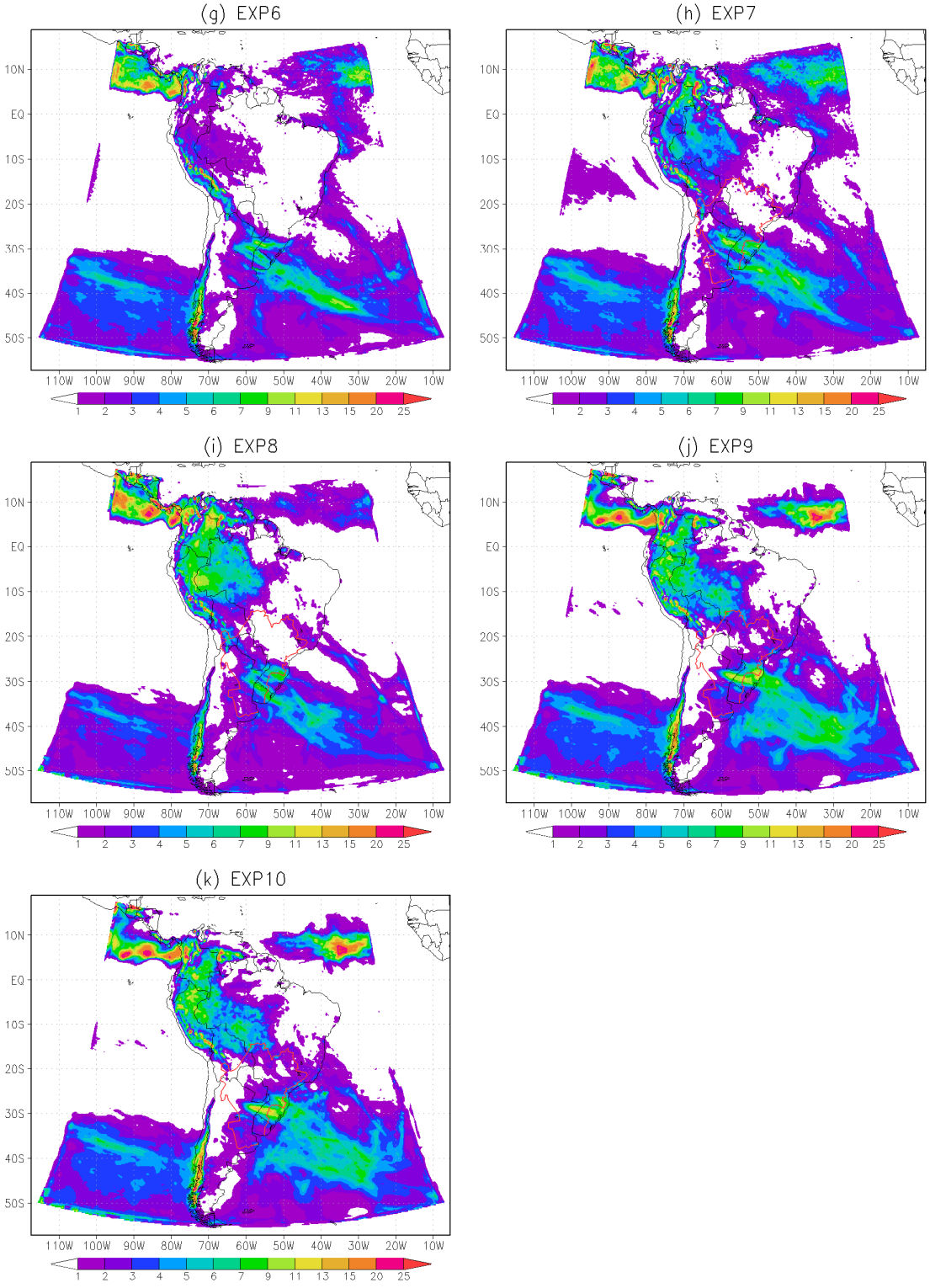

Figure 3.3: (Continued.)

In spite of overall better simulations than the others, EXP4 has a few relative shortcomings. The first thing is overestimated precipitation in the northwestern SA. Especially, it is noted that there is excessive and bull's-eye-like rainfall in mountainous areas in Peru. Excessive rain over the Andes Mountain range is a shortcoming that EXP1, 4 and 5 have in common. The second is little precipitation in the north of the LPB, i.e., over central and eastern Brazil. EXP9 and EXP10 ameliorated the two problems of EXP4 mentioned above. EXP9 and EXP10 reduced the overestimated precipitation in the western SA as well as the bull's-eye-like rainfall in mountainous areas in Peru. They produced more precipitation in the north of the LPB, where EXP4 underestimated the precipitation area. The simulated ITCZ heavy rainfall bands are also better than EXP4. EXP10 (and EXP9) increased precipitation in R1 region and over sea in front of Suriname. When it comes to R7, EXP4 is a little bit better than EXP9 and 10. The precipitation area over the eastern ocean adjacent to the LPB became wider when EXP10 is used.

Figure 3.4 shows the Hovmöller diagram for precipitation total for those three experiments. All of them show similar patterns in the diagram, but the evaluation of precipitation west and east of 70°W shows different characteristics. The west shows light rainfall by non-convective larger-scale processes, while the east shows heavy rainfall by convective smaller-scale processes (not shown). Also, many features in both sides show an eastward propagation of precipitation with time. To the east of 70°W, the eastward displacement of the precipitation features is related to the eastward movement of mid-latitude synoptic storms which include Mesoscale Convective Complexes (MCCs). The light rain on the west side of 70°W seems to be induced by mid-latitude synoptic waves. Some features at 70°W show considerable persistence

with time. The persistent precipitation features at 70°W correspond to a forced lifting on the windward slope of the Andes Mountain ridges, and are overestimated by experiments EXP4, 9 and 10.

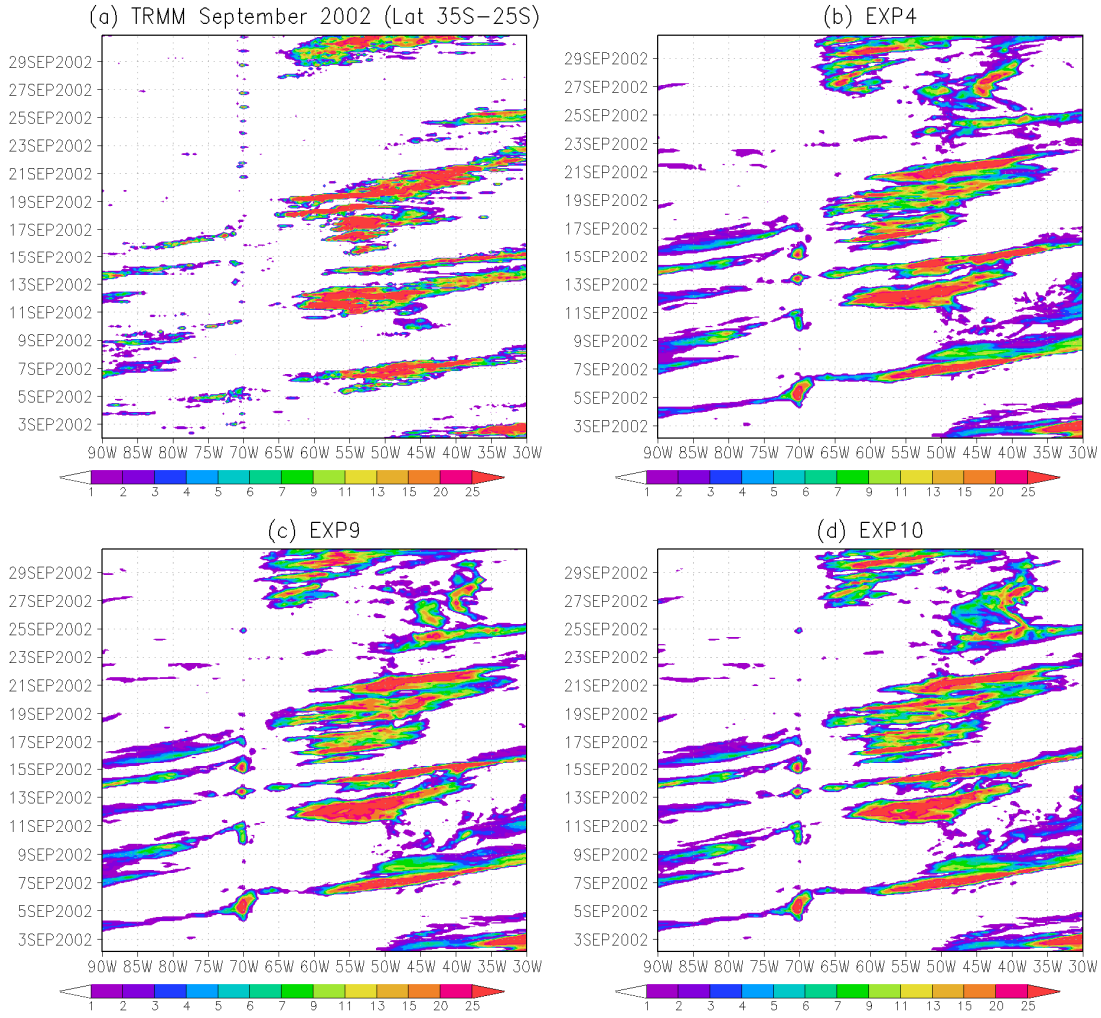

Figure 3.4: The Hovmöller diagram for September-2002 precipitation total (in mm day^{-1}) averaged over 35°S to 25°S in EXP4, 9, and 10.

Figure 3.5 shows time series comparisons of the daily-precipitation for major precipitation events during September 2002. The precipitation was averaged over an area, 57°W-51°W in longitude and 31.5°S-27°S in latitude. Figure 3.5a shows two peaks in observed precipitation. EXP3, 7 and 8 missed the first peak, but EXP9 and 10 was close to observed maximum at 1200 UTC 06 September. EXP10 captured very closely the second peak of the observed precipitation. Figure 3.5b shows five peaks in precipitation amount. All experiments did not capture or highly underestimated the first two peaks. EXP4, 5, 9 and 10 have good correspondence with the third peak, and EXP4 showed the best performance in this event. Figure 3.5c shows a series of precipitation events with four peaks of precipitation amount larger than Figs. 3.5a,b. Model precipitation from all experiments was underestimated compared with the observed precipitation especially between 19 and 20 September. EXP 4, 9 and 10 captured reasonably the pattern of the four peaks, and EXP10 showed the best performance in this event.

Lastly, Fig. 3.6 shows the time series of accumulated precipitation averaged over the area (57°W-51°W, 31.5°S-27°S) where maximum precipitation occurred within the LPB. The accumulated precipitation continues to increase through 20 September, and then has a flat portion (no rain) for about ten days. It starts increasing again near the end of the month. Compared to the TRMM observations, less accumulated precipitation was produced in all the experiments. Among them, EXP4, 9 and 10 have relatively good agreements with observations and have similar behaviors to the flat portion of the observed graph. Especially, EXP10 has the biggest accumulated precipitation, and also captures well the feature of increase in precipitation near the end of the month.

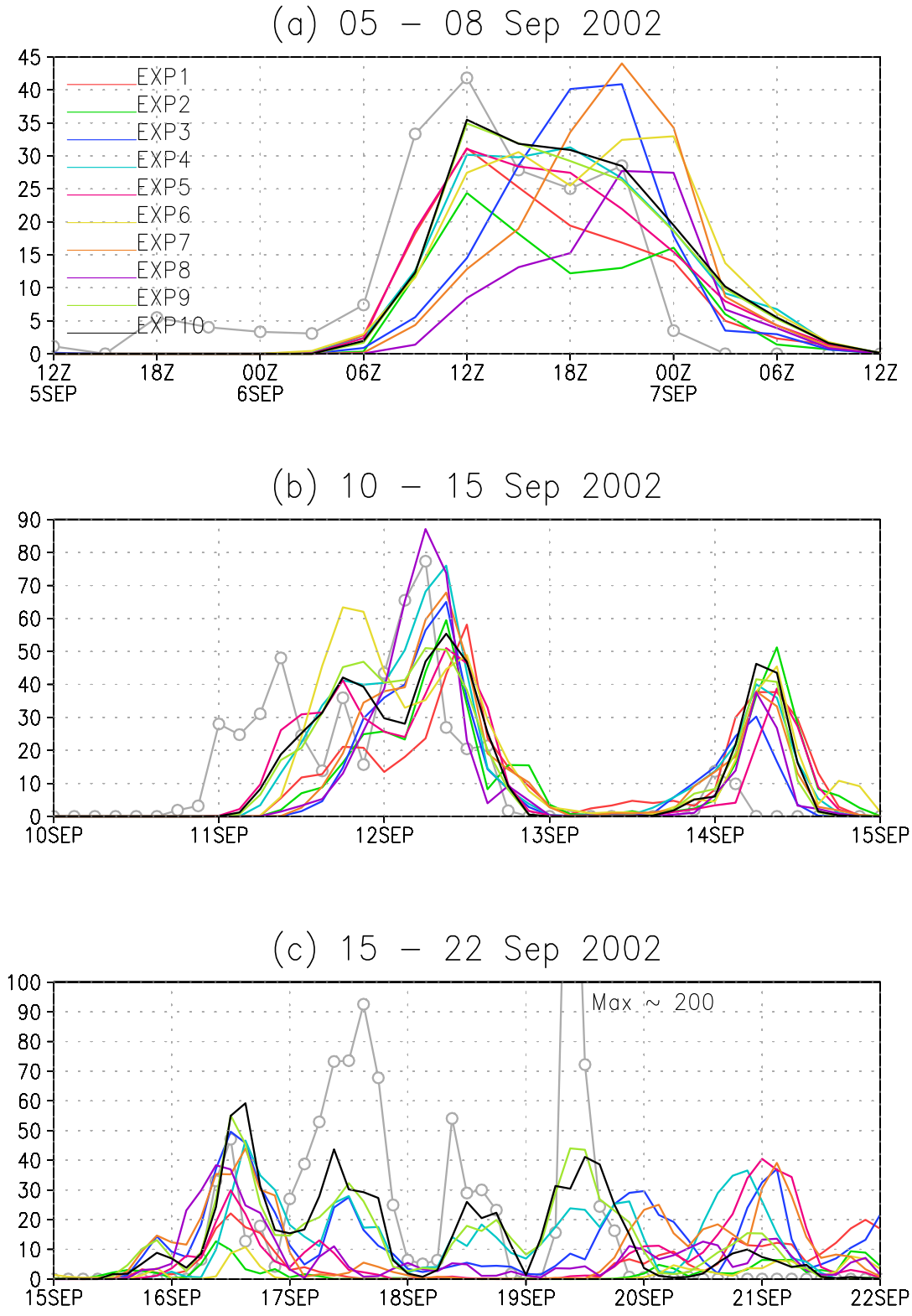

Figure 3.5: Time-series of precipitation total (in mm day^{-1}) averaged over an area, 57°W-51°W in longitude and 31.5°S-27°S in latitude. Gray lines with open circles denote TRMM observation. 'Max ~ 200' means precipitation with its maximum being 200 mm day^{-1}.

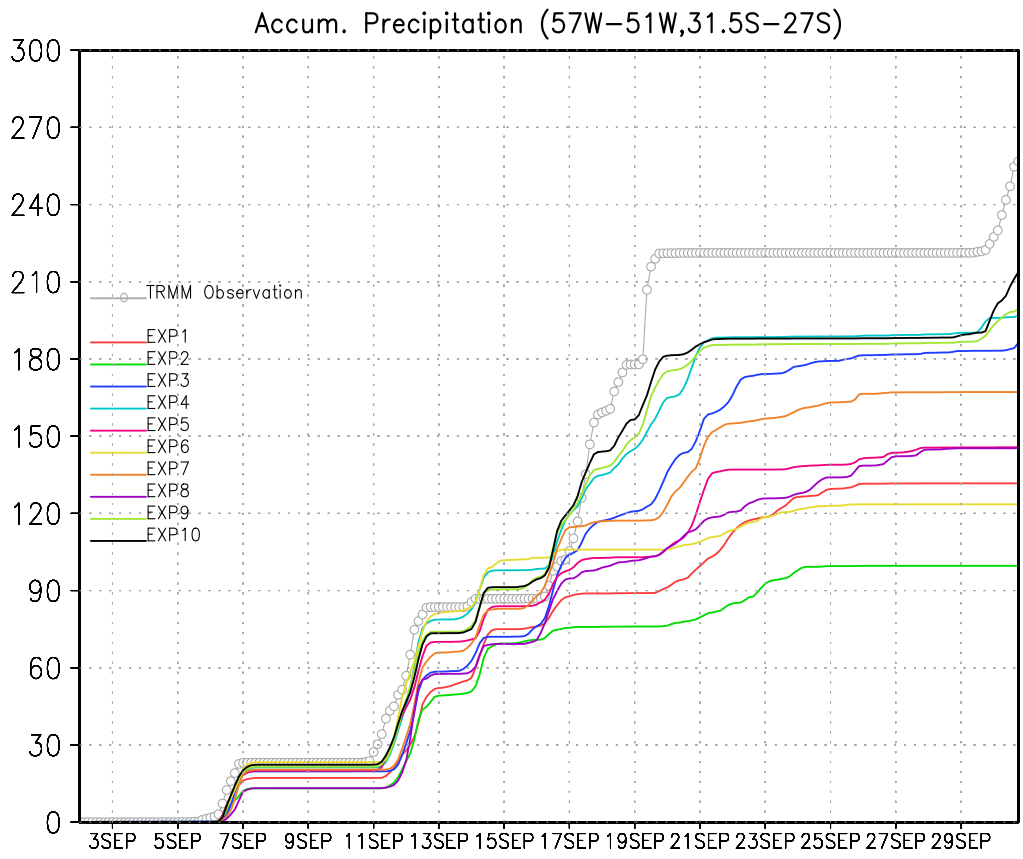

Figure 3.6: Accumulated precipitation averaged over the area (57°W-51°W, 31.5°S-27°S) where maximum precipitation occurred within the LPB.

Considering all the features discussed above, we can conclude that the most appropriate model physics configuration is EXP10, which is composed of the Dudhia shortwave scheme (Dudhia 1989), the WRF Single Moment 6-class microphysics (Hong and Lim 2006), the Betts-Miller-Janjic cumulus scheme (Janjic 1994, 2000), the Mellor-Yamada-Janjic boundary layer scheme (Janjic 1990, 1996, 2002), the Monin-Obukhov-Janjic surface layer scheme (Janjic 1996, 2002), and the Noah land surface model (Chen and Dudhia 2001). This configuration is a reasonable choice to best simulate the springtime precipitation in this region. Thus, from now on, the model physical configuration of EXP10 will be used for all the numerical model simulations in the present study. Table 3.2 summarizes the model dynamical configuration as well as physical configuration. Additional information on the model sensitivity is provided in Appendix A from the viewpoint of a mixed physics ensemble.

Table 3.2: The specification of the WRF modeling system with a suite of physical parameterization schemes recommended in this chapter.

Grids	Single domain (36 km for 692x470 gird points)
Numerics	Primitive equations based on the non- hydrostatic frame
Vertical resolution	27 vertical levels with model top of 10 hPa
Lateral boundary condition	Time and inflow/outflow dependent relaxation
Later boundary update	6-hour interval by NNRPs
Time integration	One month (180s interval)
Horizontal diffusion	Fourth order diffusion
Precipitation physics	WSM6 microphysics (Hong and Lim 2006)
Deep convection	BMJ cumulus scheme (Janjic 1994, 2000)
PBL and surface layer	MYJ PBL scheme (Janjic 1990, 1996, 2002) and MOJ surface layer scheme (Janjic 1996, 2002)
Land surface physics	NOAH LSM (Chen and Dudhia 2001)
Short wave radiation	Dudhia shortwave scheme (Dudhia 1989)
Long wave radiation	RRTM (Mlawer et al. 1997)

3.4 Summary

In this chapter, model sensitivity tests were carried out to find the optimal physics configuration for the best precipitation simulation performance. The recommended physics combination is composed of Dudhia shortwave scheme, WSM6 microphysics, BMJ cumulus scheme, MYJ PBL scheme, MOJ surface layer scheme, and NOAH LSM.

Simulations of the 2002 austral spring season in South America using a mesoscale regional WRF model of 36 km single domain mode with the recommended physics suit was successful. Monthly averaged precipitation distribution and intensity were satisfactory when compared to high-resolution satellite rainfall data (TRMM).

In the dissertation, study time period is a normal spring season (September – November 2002) and thus the model sensitivity tests were conducted for the same period. Although EXP10 is not necessarily the best choice for other seasons or years, but still it could be a good candidate (or starting point) to try in case of other model domains and seasons too.

Chapter 4: Influence of Land-Cover and Land-Use Changes on the Climate of the La Plata Basin

4.1 Introduction

The research presented in this chapter is based on the analysis of model simulations performed with the Weather Research and Forecast (WRF) modeling system (Advanced Research WRF, version 2.2.1). Sensitivity experiments were carried out to determine how vegetation types over La Plata Basin may influence the surface and near-surface conditions, the boundary layer and the processes that control the regional climate during austral spring. To this end, multiple three-month simulations from 1 September 2002 to 30 November 2002 were performed. The initial boundary conditions and the 6-hour lateral boundary conditions were taken from the NCEP/NCAR Reanalysis data (Kalnay et al. 1996). The model was run on a continental scale with a two-way interaction nested grid over the La Plata Basin. Model physical parameterizations follow the recommended suit in Chapter 3 (Table 4.1).

Figure 4.1 presents the two domains, which have a grid spacing of 36 km and 12 km respectively, and 27 vertical levels from the surface up to 10 hPa. Also presented in the figure is the model topography, with the Andes Mountains along the west coast with an average height of about 4 km. The Brazilian Highlands (with a height of about 1000-1500 m) along the central east coast of Brazil are also relevant for the climate of the La Plata Basin, and finally the Guiana Highlands (with heights also around 1500 m) are shown near the northern part of the continent. Relatively low

lands are present among the three high terrain features, and particularly over large expanses of the La Plata Basin.

Table 4.1: The specification of the WRF modeling system used in Chapter 4.

Grids	Double nested domain (36km for 770x495 and 12km for 756x615 gird points)
Numerics	Primitive equations based on the non- hydrostatic frame
Vertical resolution	27 vertical levels with model top of 10 hPa
Later boundary condition	Time and inflow/outflow dependent relaxation
Lateral boundary update	36 km : 6-hour interval by NNRPs 12 km : 6-hour interval by 36 km forecasts
Time integration	3 months for both 36 km and 12 km meshes (180s intervals in the coarse grid)
Horizontal diffusion	Fourth order diffusion
Precipitation physics	WSM6 microphysics (Hong and Lim 2006)
Deep convection	BMJ cumulus scheme (Janjic 1994, 2000)
PBL and surface layer	MYJ PBL scheme (Janjic 1990, 1996, 2002) and MOJ surface layer scheme (Janjic 1996, 2002)
Land surface physics	NOAH LSM (Chen and Dudhia 2001)
Short wave radiation	Dudhia shortwave scheme (Dudhia 1989)
Long wave radiation	RRTM (Mlawer et al. 1997)

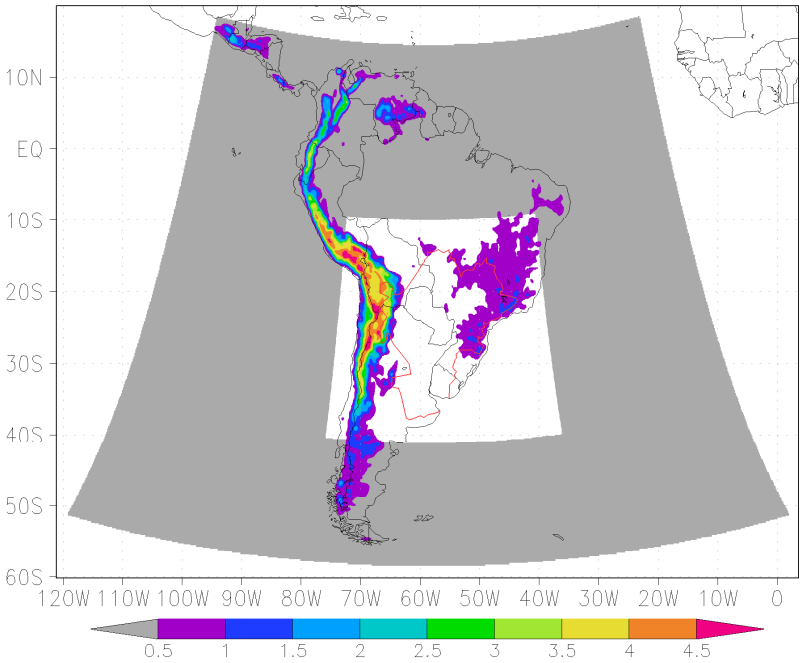

Figure 4.1: The WRF model domain and the topography used in the study. Mother and nested domains have a horizontal resolution of 36 km and 12 km, respectively. The contour of the La Plata Basin is also shown. The contour intervals for topography are indicated at the bottom in km unit.

It is a well known fact that in order to attain reliable results, multiple simulations are needed to produce a stable result. Therefore several simulations for each type of experiment were carried out following a lagged averaged technique (e.g., Hoffman and Kalnay 1983), in which each ensemble member simulation starts at lagged initial times (1 day apart). In this chapter, three four-member ensembles are prepared for one control run and two experimental runs. In order to evaluate the differences between two ensemble means, a test of significance was applied. A two-tailed t-test statistic for the difference between ensembles was employed for significance at the 90% level (see Appendix B). It is assumed that the ensemble members are independent on each other and not paired. The null hypothesis is that there is no statistically significant difference between two ensembles.

4.2 Model evaluation

The model's performance was evaluated in terms of precipitation and 2-meter temperature. For the first one, a dataset of gridded observed precipitation produced by the Climate Prediction Center (Shi et al. 2000) was used. This product consists of daily rain gauge observations interpolated to a 1° × 1° latitude-longitude grid covering South America. The analysis was complemented with the Tropical Rainfall Measurement Mission (TRMM) rainfall satellite data defined over a 0.25° × 0.25° regular grid (Huffman et al. 2007). Differences between the two datasets should be expected and give a sense of the existing uncertainties in measuring precipitation over South America. However, the analysis of both datasets is desired as certain areas do not have enough rain gauge density to give reliable values when interpolated to a grid, while satellite products depend on calibrations with rain gauges to ensure a good qual-

ity product.

Figure 4.2 presents the September-November 2002 three-month averages for both estimates of observed precipitation and the ensemble control precipitation. The two observational datasets (Figs. 4.2a,b) have a close resemblance over land with maxima over the northwestern part of the continent, including Colombia and western Amazonia, over La Plata Basin and over southern Chile. Differences in magnitude are noticed over Colombia where precipitation estimated from the raingauges is weaker than that from TRMM. One possible reason is that the raingauges included in the dataset may be sparse. Over LPB, TRMM precipitation has somewhat higher values and slightly more structure than the raingauge-based product due to its higher resolution.

Comparison of the control ensemble (Fig. 4.2c) with both observational estimates indicates a remarkable resemblance in the pattern, with similar regions of maximum precipitation. The springtime precipitation fields from the WRF simulations show that the model was able to capture the observed pattern and magnitude with reasonable success. This is particularly so for the Intertropical Convergence Zone (ITCZ) over land and ocean (Figs. 4.2b,c) and southern Chile. The precipitation center over La Plata Basin is reproduced as well, although with smaller magnitude in the simulations. The model has more difficulty to capture the South Atlantic Convergence Zone (SACZ) as it tends to put the precipitation further south and merged with another band at approximately 30-45° S. Although partial over- or under-estimation of precipitation magnitude is found, this is common to many other models as reported in the literature (e.g., Berbery and Collini 2000; Misra et al. 2002; Rojas and Seth 2003; Seth and Rojas 2003).

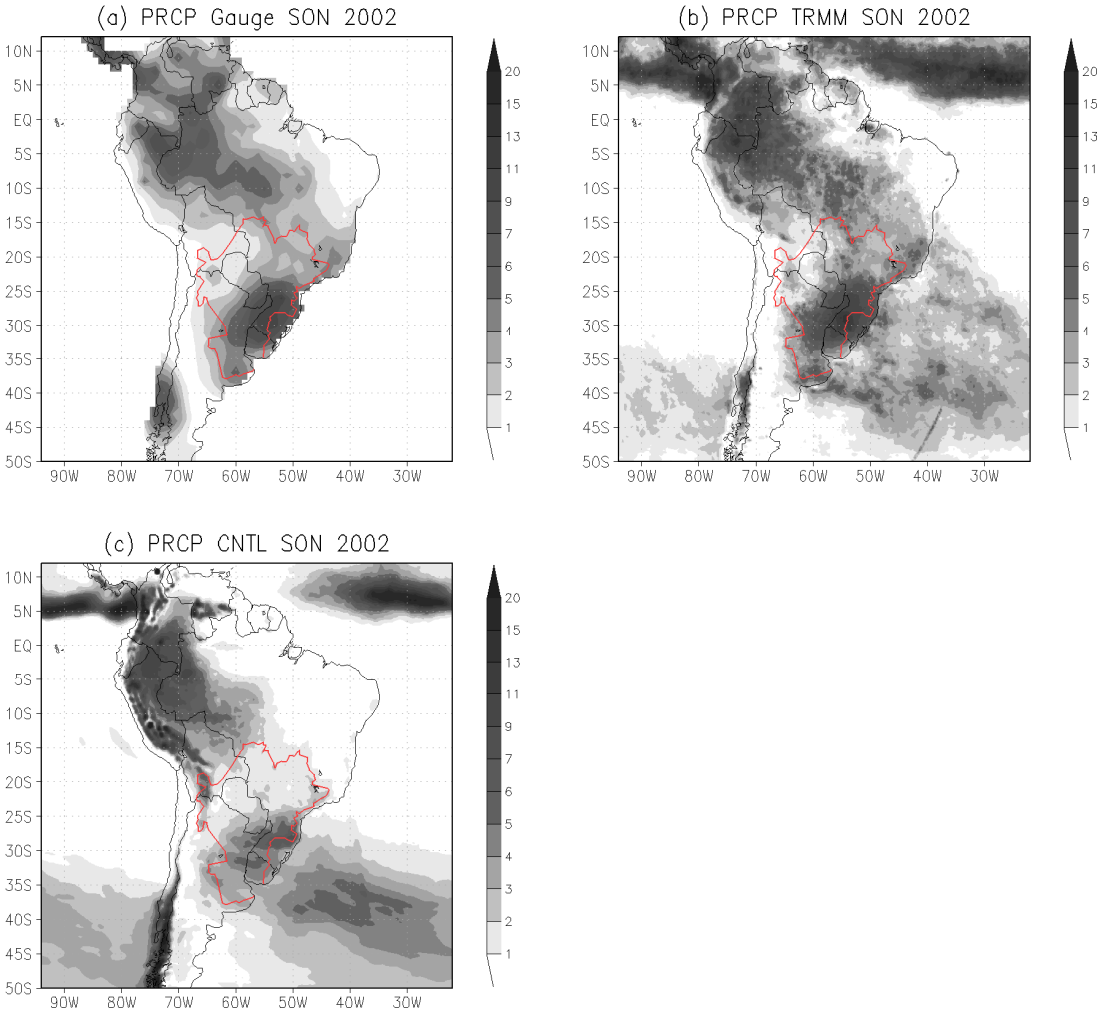

Figure 4.2: Three-month (SON 2002) averaged precipitation (mm day^{-1}) from (a) gridded raingauge observations, (b) TRMM, and (c) the WRF model CNTL experiment.

Given the emphasis of this research on surface processes, there was also interest in assessing the performance of the model's 2-m temperature, for which the dataset of the Climate Research Unit (CRU) of the University of East Anglia was employed (Brohan et al. 2006**)**. Stations measuring temperature are even sparser than those measuring precipitation, and this dataset may have unreliable values over large ungauged regions (like Amazonia) and mountainous areas, thus, the evaluation should not be more than qualitative. Figure 4.3 shows the three-month (SON 2002) averaged

2-m temperature for CRU temperature, the model ensemble, and their difference. The overall patterns of observed and model temperatures are similar, with the model exceeding the observations by 1-4 °C over the central part of the continent and slightly colder than observations near the coastlines. Most importantly, the differences are notably small within La Plata Basin, our research area. The spatial distribution and gradients having a northeast-southwest direction are also similar to the observed in LPB.

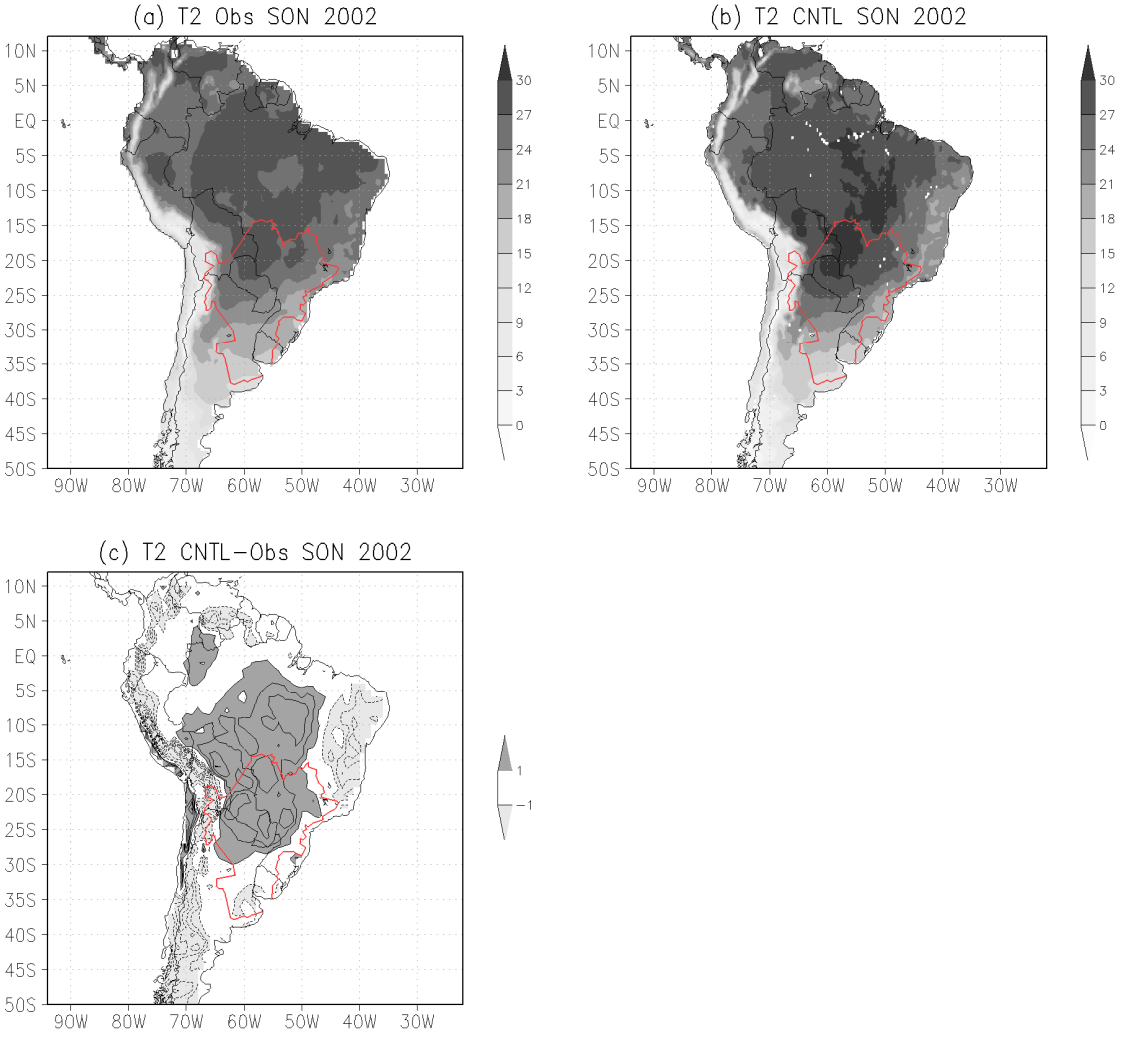

Figure 4.3: Three-month (SON 2002) averaged 2-m temperature (°C) from (a) surface observations (CRU), (b) the CNTL experiment, and (c) their difference. The contour interval is 1 °C and the zero contour is suppressed in (c).

4.3 Design of experiments for land-cover/land-use change impact

Land cover types are prescribed following 24 unique United States Geological Survey (USGS) categories each with different physical properties like surface albedo, roughness length, emissivity and stomatal resistance, among others. The USGS land cover distribution (presented in Fig. 4.4) is dominated by evergreen broadleaf forests over the Amazon basin, barren types over mountainous regions and shrublands over Patagonia. In the center region, and covering much of La Plata Basin, there is a mix of forests, croplands, and grasslands, and this region ("The Pampas") is among the most fertile regions in the Americas.

Three sets of simulations for the period from September to November 2002 were performed. The first set consists of the ensemble discussed in the previous section, and it will be identified in the text as CNTL. The control runs employed the actual USGS vegetation types that represent a current land cover pattern (Fig. 4.4) with cropland as well as natural vegetation (savanna, evergreen broadleaf forest and grasslands in the upper, middle, and lower parts of LPB, respectively).

Two other sets of idealized simulations were prepared in order to assess the impact of land cover change on the regional climate of LPB: one that assumes an extreme increase in croplands (this set will be called CROP), while the other assumes an arbitrary natural vegetation map without croplands (this set will be called NATR). The purpose of defining these two scenarios is to assess *the ranges of variability* that could be expected due to land cover changes. For the CROP experiments, the three natural vegetation types within La Plata Basin (savanna, evergreen broadleaf forest and grass-

lands) were replaced by dry croplands (rain fed agriculture). For NATR experiments, current croplands were replaced by natural vegetation, as if there had not been an anthropogenic land cover effect. In both cases, all changes were restricted within the basin, and are linked with changes in surface albedo, roughness length, emissivity, stomatal resistance, and rooting depth. In the Noah land surface model of the WRF system version 2.2.1, leaf area indices are fixed as 4.0 for all types of vegetation. Table 4.2 describes the specific values of major surface physical parameters used in the experiments. It is well known that land cover changes have been extensive over the Amazon basin and other nearby areas that may also affect the climate of LPB, but these other factors are not part of our current study.

Figure 4.5 presents the LPB regions affected by the modified land cover types along with the corresponding changes in some of the physical properties. In the places where the changes have been from savanna to cropland (Region I) there is a decrease of the surface roughness (Fig. 4.5c and Table 4.2) and practically no change in the albedo (Fig. 4.5b and Table 4.2). The larger changes occur over the region where evergreen broadleaf forest is replaced by cropland (Region II); here, in addition to the reduced surface roughness there is also a noticeable increase in albedo. The area with changes from grassland to cropland (Region III) reveals a decreased albedo and a small reduction in surface roughness. Region I and III do not have any changes in surface emissivity, while over Region II the surface emissivity is decreased from 95% to 92% (Fig. 4.5d and Table 4.2). In all three areas the low level wind is expected to be increased due to the reduction in surface roughness.

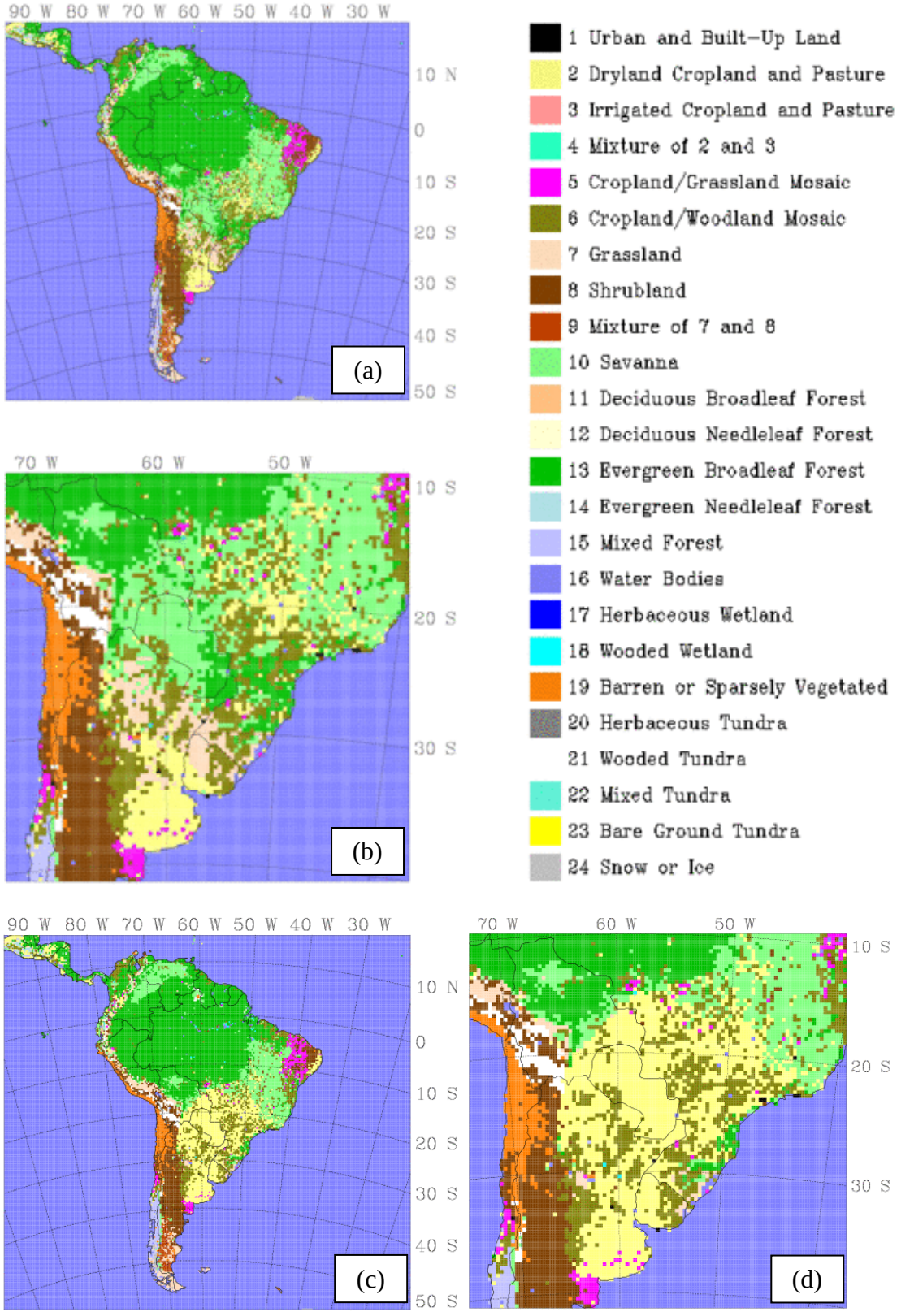

Figure 4.4: Land use/land cover maps used for the control experiments (CNTL) for (a) the mother domain of 36-km grid spacing, and (b) for the nested domain with a grid spacing of 12-km. The land cover types are defined on the right. (c) and (d) are for CROP.

Table 4.2: Values of major surface physical parameters used in the numerical model.

Type of land cover	Surface albedo [%]	Surface roughness [cm]	Stomatal resistance [s m^{-1}]	Surface emissivity [%]
Savanna	20	15	70	92
Evergreen broadleaf forest	12	50	150	95
Grassland	23	10	40	92
Dry cropland and pasture	20	5	40	92

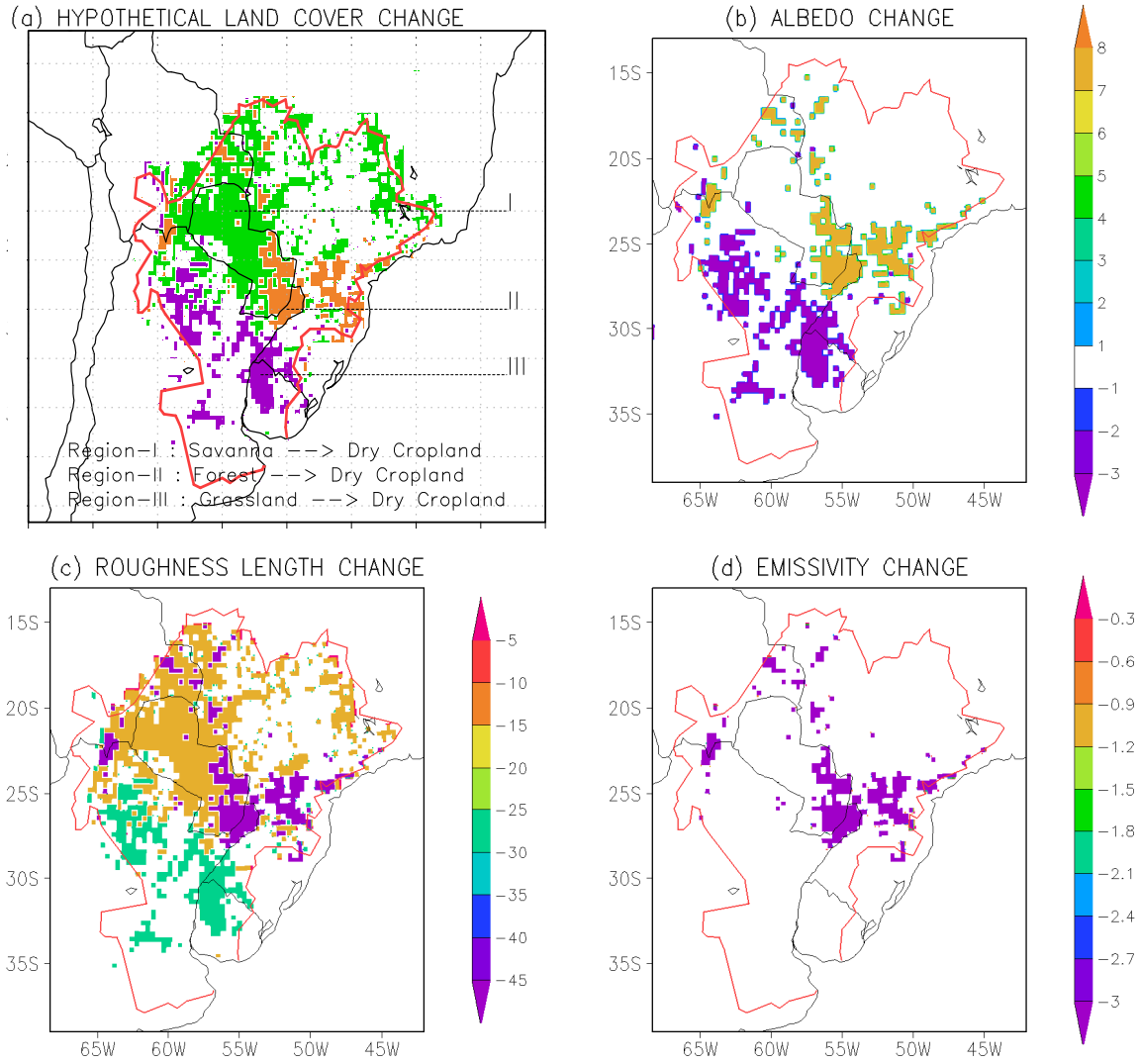

Figure 4.5: (a) The changes in land cover/land use when replacing Savanna (I), rain-forest (II: evergreen broadleaf forest), and grasslands (III) to dry cropland over LPB. Changes in (b) albedo (%), (c) roughness length (cm), and (d) emissivity (%) over Region I, II, and III.

4.4 Analysis of the CROP experiment

In order to examine the changes to the mechanisms that may affect the regional climate, in this section we will look at the surface fluxes, the convective instability, the low level winds, and the moisture transports into the region.

4.4.1 The diurnal cycle of the surface energy balance

The local effects are first investigated by examining the simulated mean diurnal cycle of the surface energy budget for the three regions where natural vegetation was replaced by crops. According to Fig. 4.6a, over the region covered by savanna (Region I) the surface energy budget is dominated by the sensible heat flux that compensates about two thirds of the net radiation, with latent heat flux and ground heat flux accounting for the remainder. The figure also suggests that the ground heat flux is relatively large compared with the other regions, and even of a magnitude close to that of the latent heat. Changes from savanna to cropland have a very small impact in the local surface energy balance, with a slight increase in sensible heat flux and a slight decrease of latent heat flux, the two in the range of $\pm$ 10 W m^{-2} during daytime (Fig. 4.6b). Changes in net radiation due to the land cover change are almost negligible.

The LPB region covered by evergreen broadleaf forest (Region II) shows a very different energy balance (Fig. 4.6c). While the maximum net radiation is similar to that over savanna, now the balance is achieved with a significant contribution of the latent heat flux and a smaller contribution of the ground heat flux. When the land cover is changed to cropland, the effect on the energy balance becomes noticeable (Fig. 4.6d), with a reduction of the net radiation and of the sensible heat flux (about -50 to -60 W

m^{-2} during daytime). On the other hand, the latent heat flux becomes larger, meaning an increase of evapotranspiration due to a decreased stomatal resistance (Table 4.2 and Chen and Dudhia 2001) and enhanced near-surface winds (Ek et al. 2003, Raymond et al. 2004, Back and Bretherton 2005). Chen and Dudhia (2001) showed that the canopy evapotranspiration is enhanced when stomatal resistance is decreased, and Raymond et al. (2004) suggested the so-called atmospheric wind speed-evaporation feedback where in a region and period of increased mean surface winds, precipitation is enhanced because of increased surface latent heat fluxes. In addition, the evapotranspiration depends on temperature, and the reduction of sensible heat fluxes indicates a reduction of temperature (Chen and Dudhia 2001, Ek et al. 2003). Therefore, the increase of latent heat fluxes is possible from decreased temperature, and more possibly through a combined effect of all these relationships.

The region covered with grassland (Region III) has smaller net radiation than the other two regions during daytime (Fig. 4.6e). The ratio latent-to-sensible heat flux also becomes larger, more than doubling the magnitude of the first one with respect to the second one. In other words, the relative contribution of the latent heat flux becomes more relevant than in the other regions at the expense of the sensible heat flux. The ground heat flux remains relatively small and is not a major factor in the energy balance. The changes to cropland result in an increase of the net radiation that is equally balanced by the sensible and latent heat fluxes (Fig. 4.6f). In this case the changes in ground heat flux are nearly zero.

Region II exhibits an increase in net radiation at night (Fig. 4.6d) and this is related with a surface emissivity decrease over that region. Net radiation is not necessarily proportional to albedo change because it is dependent not only on incoming and out-

going shortwave radiation, but also on downward and upward long wave radiation, which relies on surface emissivity. Table 4.2 shows that evergreen broadleaf forest has surface emissivity of 95%, while the other three types of vegetation have surface emissivity of 92%. Thus, the Region II changing from evergreen broadleaf forest to dry cropland has an increased net radiation due to the decreased surface emissivity (Fig. 4.6d). This explains why a decrease of 3% in albedo in Region III produces a similar magnitude of change in net radiation as does 8% albedo increase in Region II. Without the surface emissivity change effect, the maximum reduction of net radiation in Region II would be about -50 W m^{-2} at 15 UTC as seen in Fig. 4.6d.

In summary, over savanna the net radiation is largely balanced by the sensible heat flux because the region has smaller moisture availability (not shown). On the other hand, in the two other regions (forest and grassland) latent heat is the primary factor to balance the net radiation. The largest change in the surface energy balance occurs in the region transformed from evergreen broadleaf forest to dry cropland, and the smallest change in the surface energy balances occur over the region changed from savanna to cropland.

Regions II and III exhibit opposite changes in the net radiation and heat fluxes (Figs. 4.6d,f). Region II shows a decrease in the net radiation and sensible heat fluxes due to the increased surface albedo (Fig. 4.5b) and decreased absorption of incoming solar radiation by the surface. Note that the amount of reduction in the sensible heat flux is more than two times larger than the increase in the latent heat flux. Region III has an increase in the net radiation and the sensible heat fluxes because of the reduced surface albedo (Fig. 4.5b) and increased absorption of shortwave radiation by the surface. However, both regions experience increased latent heat fluxes.

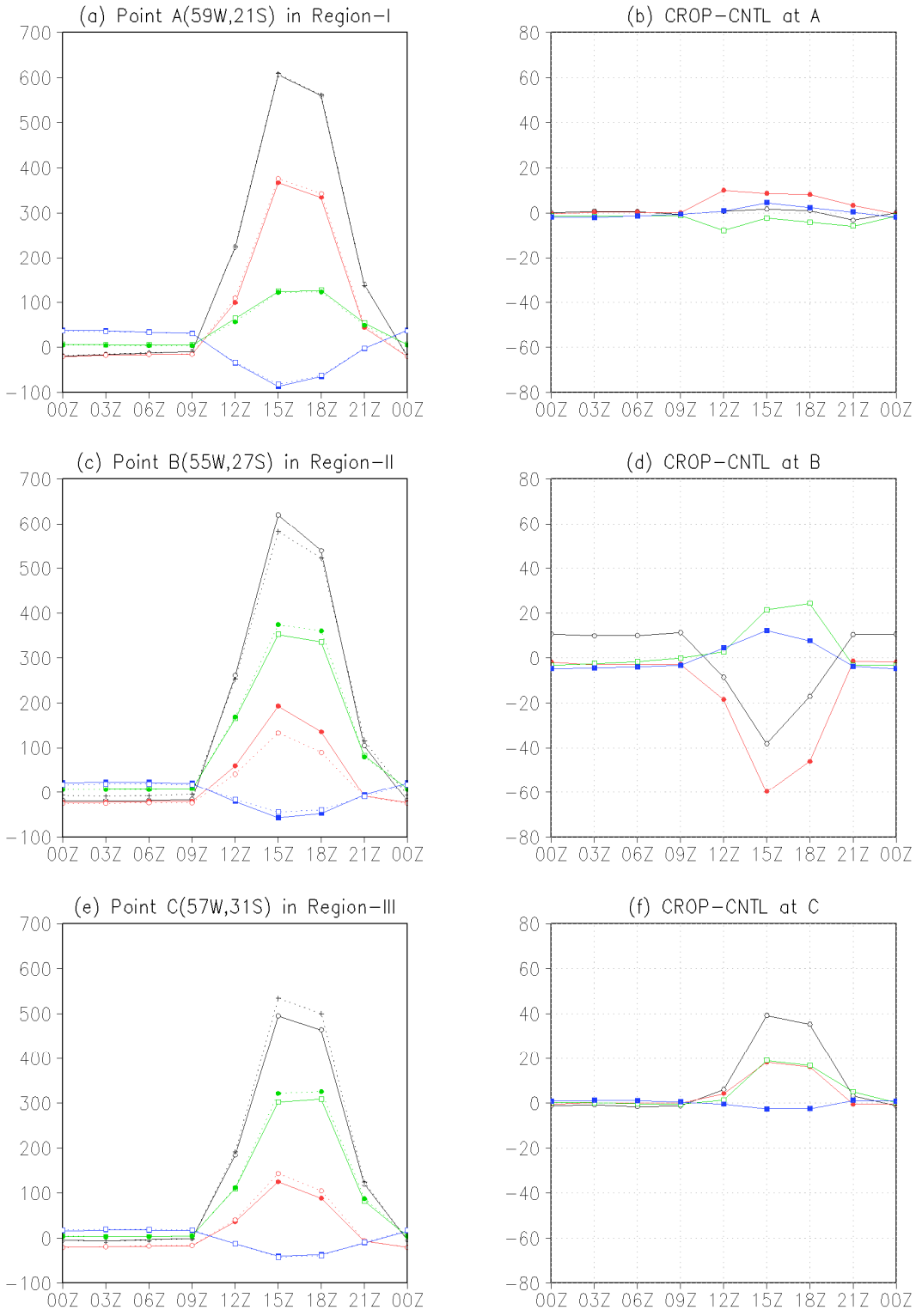

Figure 4.6: (a)-(c) Three-month (SON 2002) mean diurnal cycle of surface fluxes averaged at three selected places representing the 3 regions identified in Fig. 4.5. Solid and dotted lines denote CNTL and CROP, respectively. (d)-(f) show the differences CROP-CNTL for the same points. Black: Net radiation; Red: Turbulent sensible heat flux; Green: Turbulent latent heat flux; Blue: Conductive ground heat flux.

4.4.2 Surface heat fluxes and near-surface atmospheric variables

So far the local effects have been described, but the changes tend to be widespread, as presented in Fig. 4.7 that shows the three-month averaged field of sensible and latent heat fluxes for the control run, CNTL, and the difference CROP minus CNTL. To facilitate the analysis, two rectangle boxes are drawn in the panels. The upper box bounded by (66° W-46° W, 28° S-17° S) represents *"the northern LPB"* and the lower one bounded by (65° W-51° W, 37° S-28° S) represents *"the southern LPB"*. The latitude 28° S is appropriately located so that the northern LPB contains most of the changes from savanna and broadleaf forest to croplands (Regions I and II), while the southern LPB encompasses most of the changes from grasslands to croplands (Region III).

Figure 4.7 indicates that sensible heat flux is large in mountainous areas, whereas latent heat flux is large over the sea and the wetter low-altitude central part of LPB. It can also be seen that in general there is a reverse pattern between sensible and latent heat fluxes (when one is large, the other is small). The differences between the control and modified land cover simulations show a pattern where the sensible heat flux decreases (in general) over the northern LPB with largest changes in eastern Paraguay, and increases over the southern part of the basin (Fig. 4.7b). The latent heat flux (Fig. 4.7d), on the other hand, experiences the largest increase over eastern Paraguay and a slight decrease elsewhere on the northern LPB. The overall increase of latent heat fluxes could be a response to the decreased stomatal resistance (see Table 4.2) and the increased wind speed.

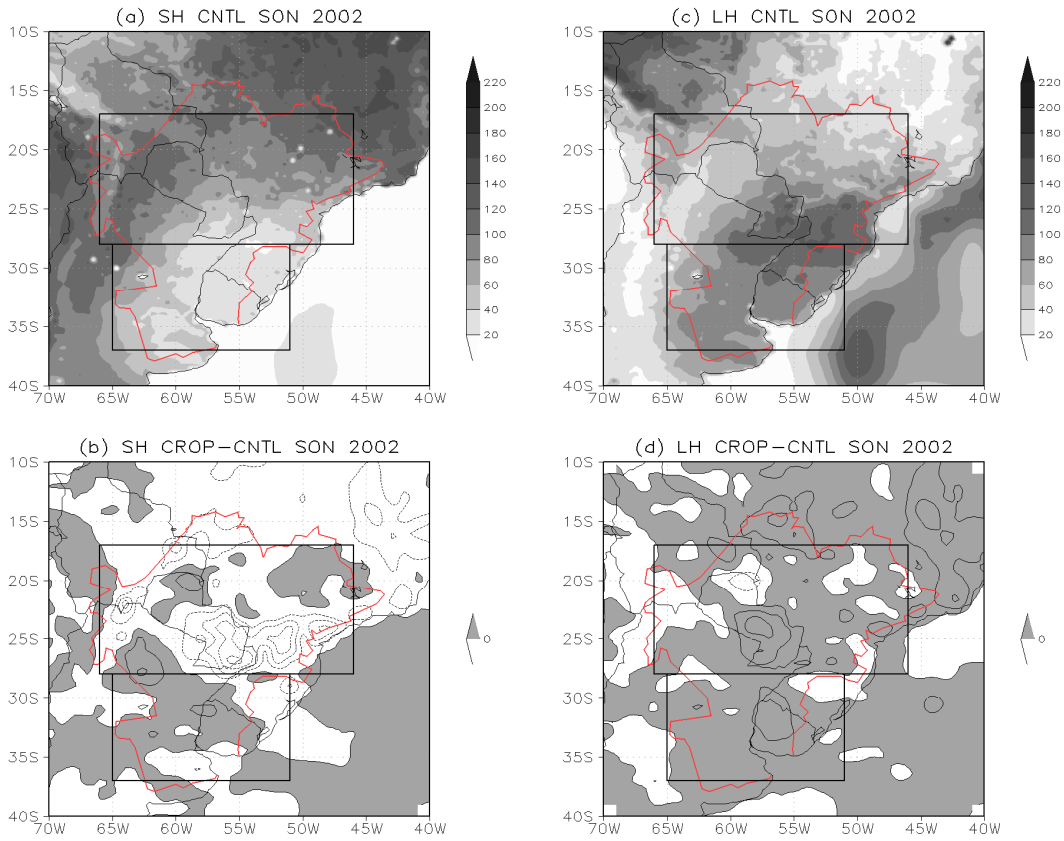

Figure 4.7: Three-month (SON 2002) averaged (a) sensible heat flux (W m^{-2}) and (c) latent heat flux (W m^{-2}) from the model simulations and their corresponding differences (b, d) when modifying the surface conditions (CROP-CNTL). The contour interval is 4 W m^{-2} and the zero contour is suppressed.

The horizontal distributions of sensible and latent heat fluxes in northern and southern LPB play a crucial role in determining near-surface temperature and humidity. Figure 4.8 shows that the decreased (increased) sensible heat fluxes in the northern (southern) LPB give rise to relatively strong cooling (weak warming) near the surface (Fig. 4.8b). The magnitude of the maximum cooling is about 1.1 °C in the northern basin, while the amount of the maximum warming is below 0.5 °C in the southern basin. These results are consistent with Beltrán-Przekurat et al. (2010) which showed that the conversion from wooded grassland or forest to agriculture produced warmer temperature, while afforestation and conversion of grass to agriculture led to a cooler

near-surface atmosphere. Fall et al. (2009) showed from their observation-minus-reanalysis (OMR) data that the shift to agriculture from four types of land covers (i.e., urban, barren lands, forests and glasslands/shrublands) gives rise to a cooling presumably because of irrigation and high evaporation. Figure 4.8 shows that Region II is in agreement with their findings, while Region III is not. The reasons for the latter can be due to the difference in agricultural systems between North America and South America. The current agricultural systems over LPB are dominated by dry croplands (Fig. 4.4b), not irrigated croplands. Accordingly, the extreme agricultural activity experiments assumed an expansion of dry croplands (Fig. 4.4d), not irrigated croplands. Region II (forest → dry cropland) experiences very large changes in surface parameters (e.g., large increase in albedo) and shows clear cooling signals in Fig. 4.7b. Region I (savanna → dry cropland) and III (grassland → dry cropland) do not show such a cooling signal. This seems to be related with the fact that dry croplands generally have smaller water (less evaporation) and smaller albedo (more insolation) than irrigated croplands, leading to slight warming in Region I and III (Fig. 4.7b). However, we should note that Fall et al. (2009) and the present study are different in the land cover classification. For example, Fall et al. (2009) grouped grasslands and shrublands, but the two are separated in this study.

Although the perturbation amplitudes of near-surface temperature have horizontally heterogeneous distributions, their spatially-averaged values are comparatively small over both the northern and southern parts of the basin (Fig. 4.8b). This is related with contrasting processes controlling ground temperature change, and is in agreement with analytical theories (e.g., Zeng and Neelin 1999) and GCM simulations (e.g., Hahmann and Dickinson 1997). In case of the northern part (Region II), for example, the ground temperature is cooled initially as incoming solar radiation decreases by an

increased surface albedo. However, negative feedbacks from reduced evaporation and increased incoming solar radiation due to reduced cloud cover tend to offset this cooling tendency, resulting in a small ground (and near-surface) temperature change (Zeng and Neelin 1999).

On the other hand, the increase in latent heat fluxes in both the northern and the southern LPB produces the increase in humidity (the 2-m water vapor mixing ratio) near the surface with a maximum again over eastern Paraguay as well as along the northern boundary of the LPB, and the magnitude of change is over 0.4 g kg^{-1} (Fig. 4.8d). The comparatively strong cooling in the northern LPB is a statistically significant signal at the 90% level of confidence. The relatively weak warming in southern LPB is partly statistically significant at the same level. The somewhat large changes water vapor mixing ratio along the northeastern boundary (parts of the Brazilian Highlands) of the basin are associated with local changes in latent heat fluxes (Fig. 4.7d), but cannot be fully explained. The latent heat fluxes and the near-surface humidity in LPB seem to be influenced by non-local effects such as large-scale moisture fluxes (shown later in Fig. 4.12d).

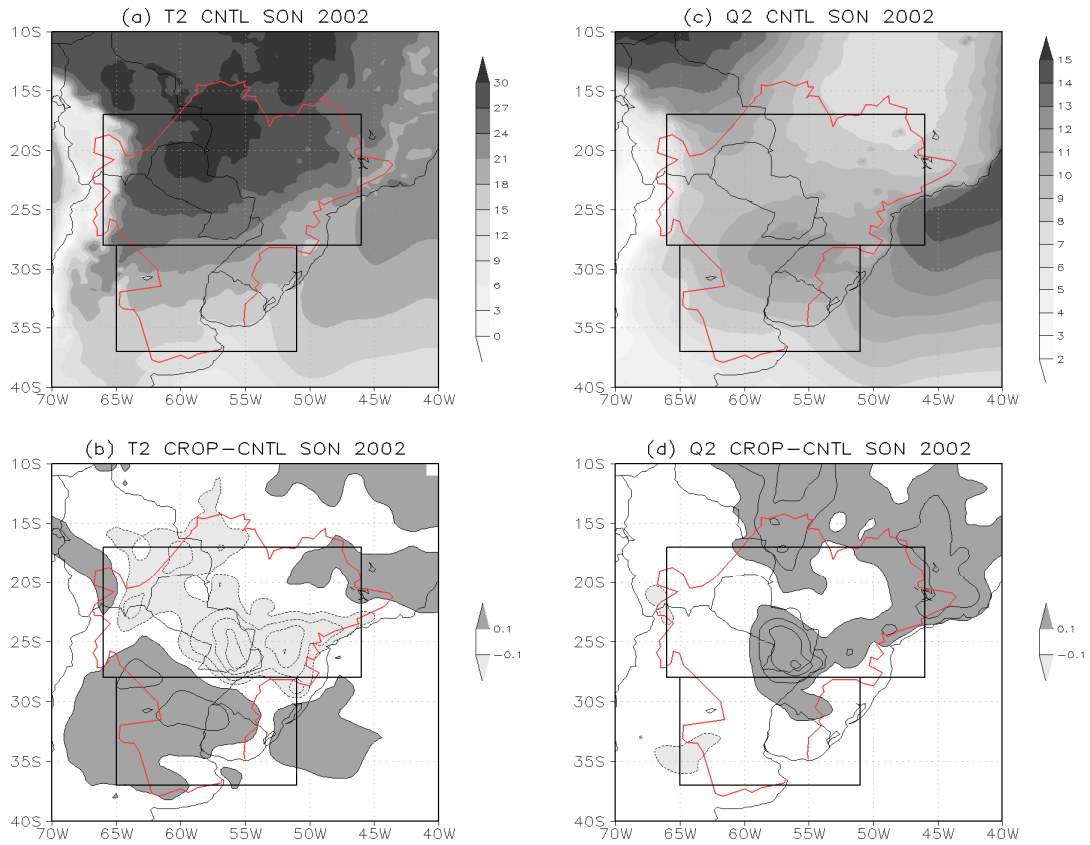

Figure 4.8: Same as Fig. 4.7 but for (a) 2-m temperature (°C) and (c) 2-m water vapor mixing ratio (g kg^{-1}) on the right panels. The plotted contours are [-1.2, -0.9, -0.6 -0.3, -0.1, 0.1, 0.3] in (b). The contour interval 0.1 g kg^{-1} and the zero contour is suppressed in (d).

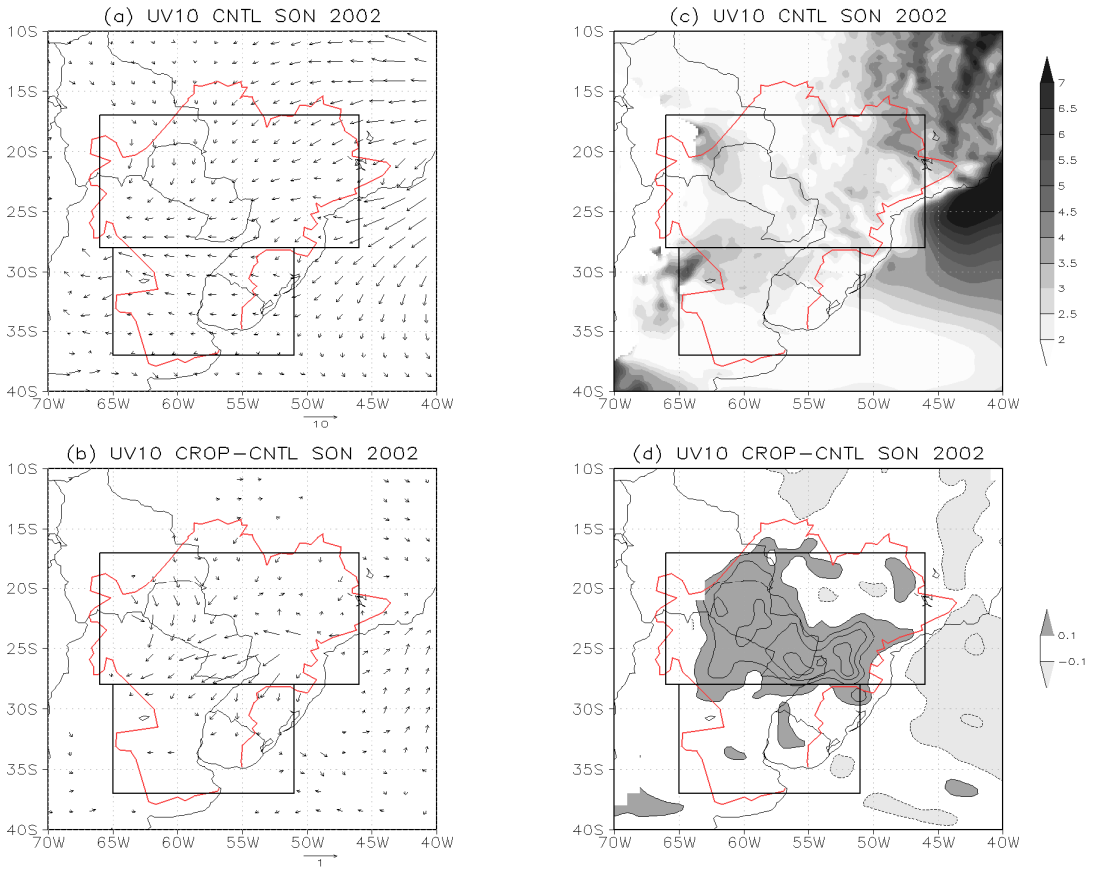

Figure 4.9: Same as Fig. 4.7 but for 10-m horizontal wind vectors (left panels) and their magnitude (right panels; shaded; m s^{-1}). Regions of high-altitude above 1250 m on all panels and regions of weak wind below 0.1 m s^{-1} on lower panels were masked out. The plotted contours are [-0.3, -0.1, 0.1, 0.3, 0.5, 0.7] in (d).

Changes in the surface properties, particularly the surface roughness, are expected to force changes in the low level winds, and this can be noticed in Figs. 4.9b,d. The difference CROP-CNTL wind field indicates that a strengthening of the northerly/northeasterly winds near the exit zone of the LLJ, and this particular effect will be discussed later. The magnitude of the wind speed change reaches up to 1.5 m s^{-1} in the east-central region of the LPB including the southern Paraguay (Fig. 4.9d). This strengthening of near-surface winds contributes to the increases in latent heat fluxes over the LPB in Fig. 4.6d because higher wind speeds and/or reduced temperature favor more evaporation (e.g., Chen and Dudhia 2001, Ek et al. 2003, Raymond 2004).

Wind field changes are also observed over the ocean east of the LPB, suggesting a role for advective processes in the analysis of land cover impacts. The role of advection will be discussed later. The 10-m wind increase over the three regions where land cover was modified is also statistically significant (the null hypothesis, that there is difference between CNTL and CROP, is rejected at the 10% level of significance).

4.4.3 Local thermodynamic forcing

The changes in the surface fluxes and surface energy balance are expected to influence the structure of the lower atmosphere through atmospheric turbulent eddies. Figure 4.10 shows the simulated 3-month average of the Planetary Boundary Layer (PBL) heights. The PBL in the CNTL simulations is deeper in the northern part of LPB and shallower towards the south (Fig. 4.10a). The CROP-CNTL difference field (Fig. 4.10b) suggests that the northern LPB would have a large decrease in the PBL height, while the southern LPB would experience a slightly increased PBL height. Such changes in boundary layer depth are closely related with changes in sensible heat fluxes. In Region II, the decrease of sensible heat fluxes from the ground to the atmosphere would produce less vertical mixing in the PBL. This would cause the potential temperature in the PBL to be less constant with height following a dry adiabatic lapse rate, and decrease the thickness of the PBL. Region III exhibits the reverse behavior. Stronger sensible heating in the southern LPB generates more intense turbulent eddies and produces a deeper boundary layer. The largest decrease in PBL depth in Region II is due to the fact that the magnitude of reduction in sensible heat fluxes in Region II is three times larger than that of increase of sensible heat fluxes in Region III.

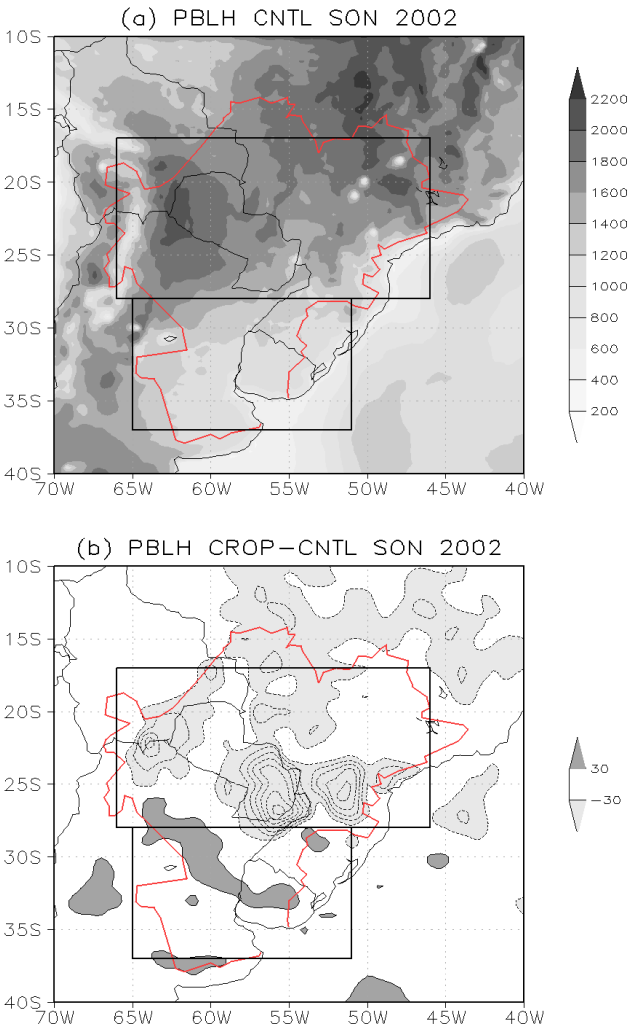

Figure 4.10: Same as Fig. 4.7 but for planetary boundary layer height (in m). The contour interval is 30 m and the zero contour is suppressed in (b).

The local processes that contribute to the development of precipitation can be analyzed using the convective available potential energy (CAPE) and convective inhibition (CIN). The CAPE (CIN) is the amount of positive (negative) buoyant energy in the vertical sounding of temperature, and by convention, both have positive signs in this chapter. The CAPE (CIN) can be regarded as the thermodynamic forcing facilitating (inhibiting) local convection and precipitation (Bluestein 1993, Barlow et al. 1998). CAPE and CIN can be computed by assuming that air parcels start ascending

from different levels. Here, we choose the level that produces the maximum values of CAPE and CIN at each horizontal point. Figures 4.11a,c show that in general there is relatively large CAPE and CIN in the southern and western parts of the LPB. This region is well known for the development of Mesoscale Convective Systems (MCSs) as discussed by Zipser et al. (2006). Also, Berbery and Collini (2000) discussed the role of MFC versus CAPE in the diurnal cycle of precipitation in the LPB, and found that thermodynamic processes are not the primary forcing for the regions' precipitation, as maxima are mostly due to large-scale dynamical processes.

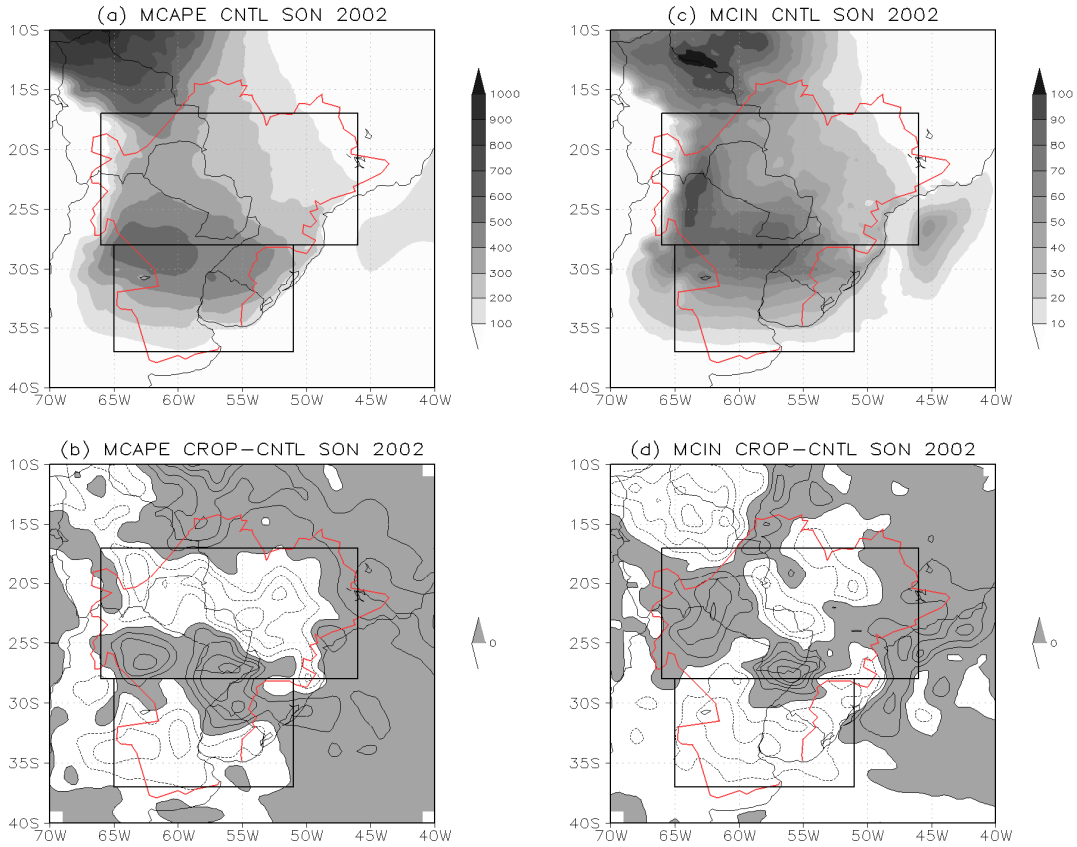

Figure 4.11: Same as Fig. 4.7 but for maximum CAPE (J kg^{-1}) and maximum CIN (J kg^{-1}). The contour intervals are (b) 10 J kg^{-1} and (d) 2 J kg^{-1} and zero contours are suppressed.

The CROP-CNTL differences suggest that the land cover change on the whole acts to decrease CAPE in the northern and the southern sectors of LPB, while it increases CAPE between 30° S and 24° S and above the northern boundary of LPB (Fig. 4.11b). Figure 4.11d indicates that the land cover change increases CIN in the central and the northwestern parts of LPB, and along the east coast, with decreases in the north-central and the southern parts of the LPB. From the difference between CAPE and CIN fields, we can determine local convection and precipitation. However, the CAPE and CIN fields in Fig. 4.11 still represent local changes in the atmospheric column, and do not fully account for the impacts of the land cover change. It will be shown next that the change in land cover can affect not only the local climate, but the larger scales climate.

4.4.4 Large-scale horizontal moisture flows

The changes in near-surface conditions, particularly the water vapor mixing ratio and the low-level winds, are expected to affect the moisture fluxes and their convergence. Figure 4.12a presents the prevailing features of the CNTL 3-month mean vertically integrated moisture flux, which is heavily influenced by the lower level layers. Large moisture fluxes associated with the trade winds can be noticed over the tropical Atlantic Ocean and into the Amazon basin. A region of large westward/southward moisture fluxes also exists on the southeastern coast of Brazil associated with the western boundary of the Atlantic anticyclone and the topography of southeastern Brazil, transporting water vapor along the coast and towards the South American Monsoon (Vera et al. 2006). However, the most relevant feature for our study is the southward moisture flux from the Amazon into the La Plata Basin noticed through the relatively low lands between the Andes Mountain ranges and the Brazilian Highlands. A closer look

at this region (Fig. 4.12c) reveals the horizontal structure of the Low-Level Jet (LLJ) east of the Andes, discussed a few times in the literature. It can also be noticed in Fig. 4.12c a region of moisture flux convergence at the exit region of the LLJ (western and southern parts of LPB). This region of convergence also prevails over the southern South Atlantic.

Figures 4.12b,d present the differences in moisture fluxes and their convergence resulting from the land cover modification from current vegetation to dry croplands (CROP – CNTL). Within the La Plata Basin, the reduction in surface roughness (Fig. 4.5c) favors stronger low-level winds and consequently stronger moisture fluxes (Fig. 4.12d), and an eastward anomaly develops. The acceleration of the moisture flux at the exit region of the LLJ produces increased divergence (or reduced convergence) of moisture fluxes particularly over the northern part of the basin. As the flow exits LPB, and into a region where the surface roughness kept the original values, there is an increased convergence of moisture flux most noticeable east of the basin. Likewise, southward anomaly winds produce increased convergence over the southern part of the basin.

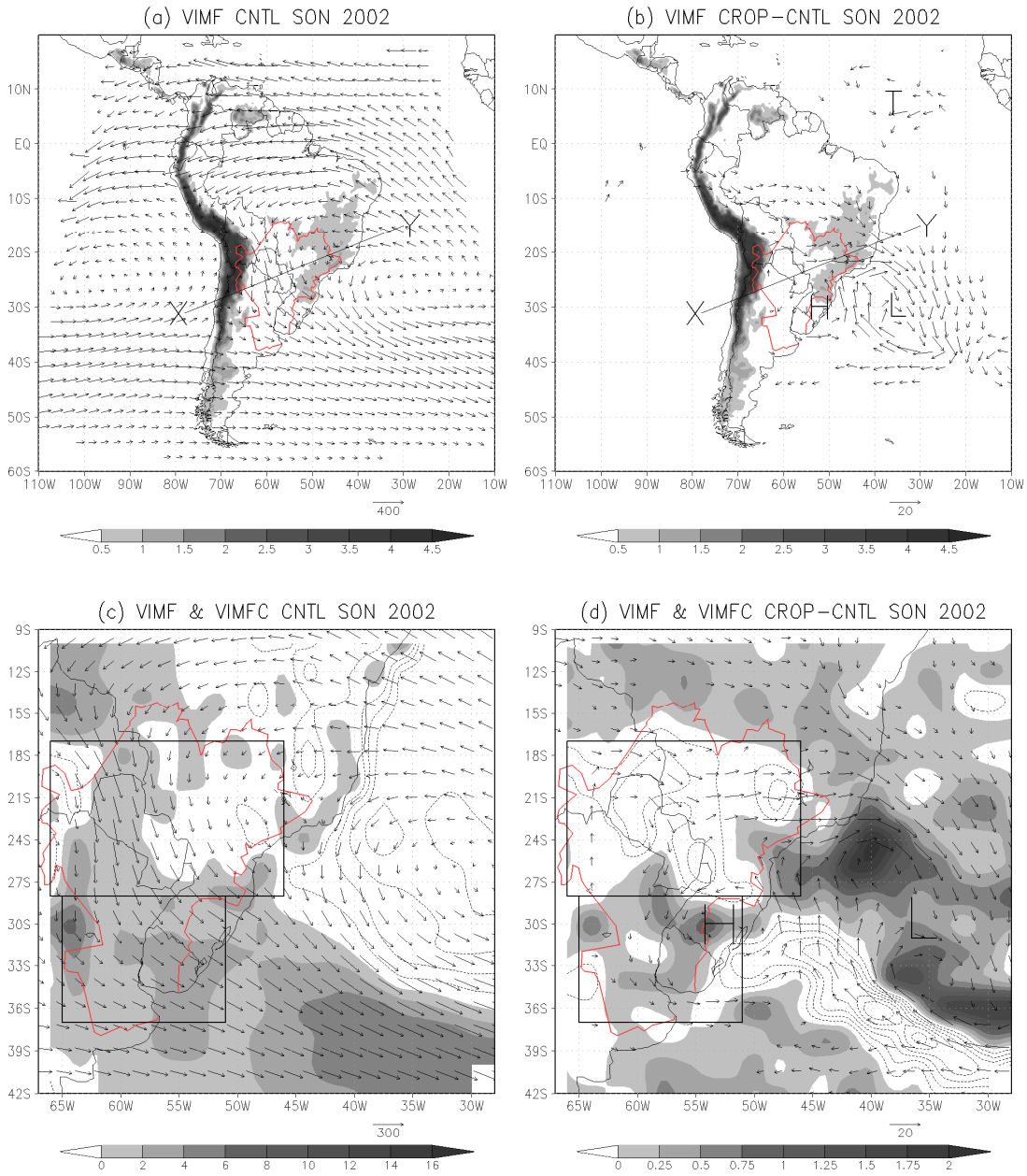

Figure 4.12: (a) Three-month (SON 2002) average of vertically integrated moisture flux in kg (m s)$^{-1}$ (shades represent the main features of the topography in km); (b) the CROP-CNTL moisture flux differences (Moisture fluxes weaker than 4 kg (m s)$^{-1}$ were masked out); (c) close-up over La Plata Basin of the vertically integrated moisture flux and its convergence (shades); and (d) as (c) but for the CROP-CNTL differences; values smaller than 3.5 kg (m s)$^{-1}$ were masked out. The magnitude of the vectors is presented at the lower right of each panel. In (b) and (d), 'H' and 'L' denote anticyclonic and cyclonic circulations of moisture flows respectively. In (b), 'T' denotes a response at a distant location.

Figure 4.13 shows the cross section, along the line X-Y in Fig. 4.12b, of the meridional moisture flux and its variation due to the land cover change. Berbery and Collini (2000) showed that the LLJ east of the Andes Mountains supplies moisture from the Tropics into the subtropics and even into the middle latitudes. Figure 4.13a shows that the southward moisture fluxes are concentrated in a narrow longitudinal band below 700 hPa. It also shows that the cross section of meridional moisture flux has a southward maximum of about 30-50 g kg^{-1} m s^{-1} through the 900-700-hPa layer on the eastern side of the Andes. Figure 4.13b shows that the extreme land-cover change would strengthen the northerly moisture flow between the central Andes Mountains and the Brazilian Highlands. This means that the land cover modification would increase the moisture injection to LPB from the north, the Amazon basin (but also increases the exit flow from the northern region). The maximum amount of the increase in the moisture flux exceeds 4 m s^{-1} g kg^{-1} in low levels (55° W - 60° W) and accordingly water vapor mixing ratio increases in the lower troposphere levels. Because a major reason for variability in precipitation over LPB is moisture transported from Amazon basin by LLJs, this result suggests that the drier (moister) springtime in the northern (southern) LPB would be induced by the assumed extreme land-cover change.

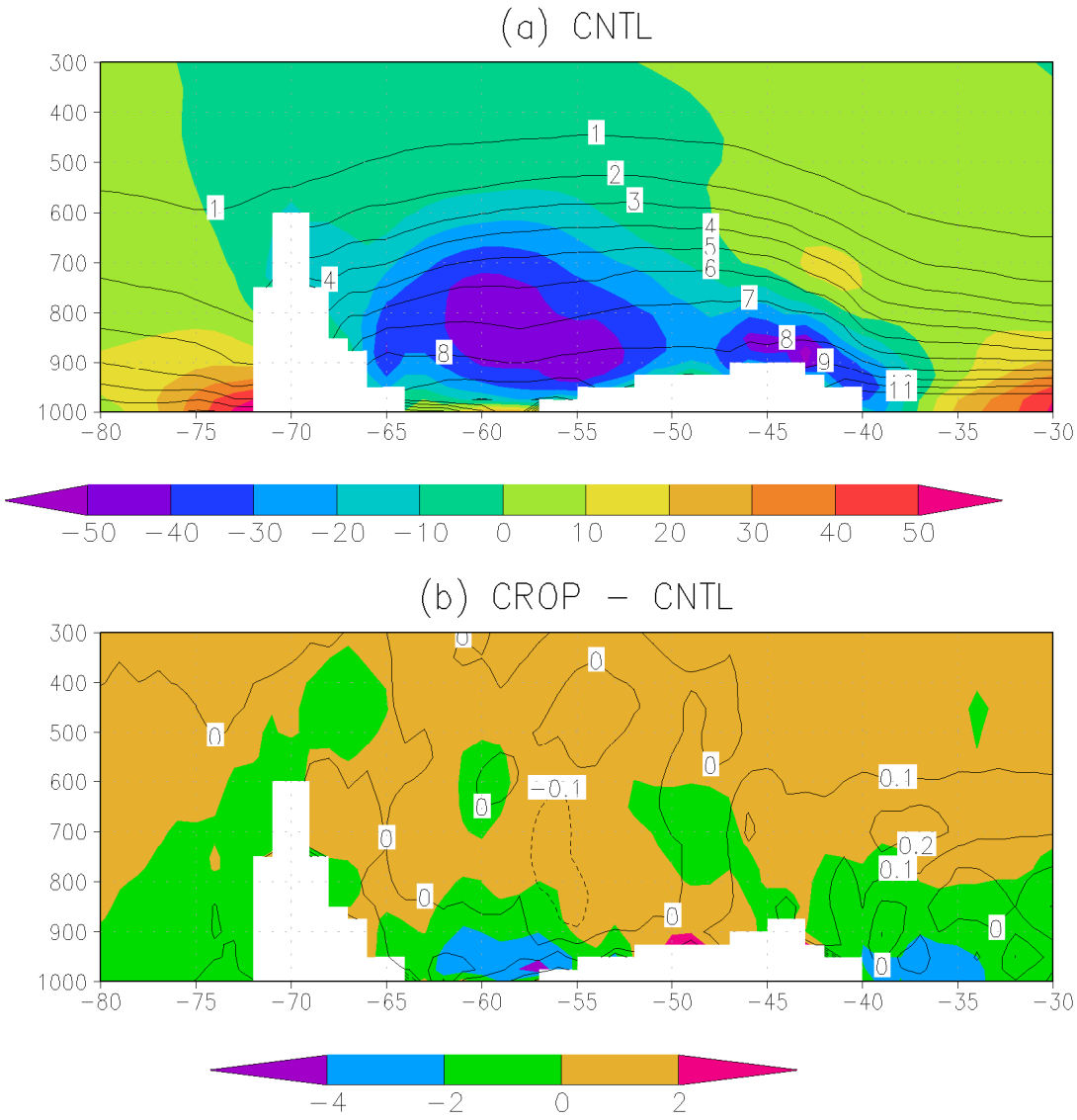

Figure 4.13: (a) Cross section of the meridional moisture flux (shaded; m s^{-1} g kg^{-1}) across the line marked X-Y in Fig. 4.12. The contours in denote water vapor mixing ratio (g kg^{-1}). The model topography is represented in white color. (b) CROP-CNTL difference in the meridional moisture flux. The solid (dotted) lines in (b) denote the positive (negative) difference with interval of 0.1 g kg^{-1}.

The spatial scale of the land cover change that must occur in order to give rise to a large-scale impact depends on where the land cover forcing occurs on the earth (Marland et al. 2003). There is no detailed study on the remote or teleconnection effect of land surface changes over the LPB. Figure 4.12 shows that the land cover change in LPB results not only in changes in the interior of the basin but also in changes in the

horizontal moisture flux patterns over the South Atlantic Ocean as well. This clearly indicates that the results of land cover change in the LPB are not strictly local, and advective processes modify the circulation and precipitation patterns downstream over the South Atlantic Ocean. The horizontal scale of the land surface change is approximately corresponding to 22° x 24°, i.e. the size of the basin. The extensive land cover changes produce anomalies of the mass/temperature fields (as shown in Fig. 4.8b), whose size is comparable to the Rossby radius of deformation (L_R). Under this circumstance, the anomaly information might be transferred to distant regions, for example, by Rossby wave propagations (personal communication, Laprise 2009) or by circulation connecting the Tropical Ocean and mid-latitude regions. This could be the case of the anomalous atmospheric circulations near 10° N ('T' in Fig. 4.12b), far beyond the LPB. Or, the remote response can be the anomaly flow fields which can be diagnosed by large-scale dynamics through moisture convergence (Zeng and Neelin 1999). It remains to be verified if the two features are dynamically related or are simply "noise" in the simulations. This subject will not be examined here

4.4.5 Surface precipitation

Figure 4.14 presents the precipitation fields averaged over 3 months (the precipitation in Fig. 4.14a is the same as in Fig. 4.2c). The control run shows that the precipitation fields exhibit larger precipitation over the southern LPB than over the northern LPB (Fig. 4.14a). Figure 4.14b presents the precipitation difference between the CNTL and CROP experiments. The changes in the precipitation field can be explained as the combined effects of both local (e.g., CAPE/CIN effects) and large-scale (moisture fluxes) forcings induced by the land cover change. There is an overall consistency between the precipitation field and vertically integrated moisture flux convergence.

On the whole, the regions of precipitation increase (decrease) are collocated with vertically integrated moisture flux convergence (divergence). Especially, precipitation change over the ocean is more related with large-scale moisture flux change, than to the local thermodynamic changes.

Figures 4.14b,d show that the northern LPB may experience drier climate with the reduced precipitation with the centers of the drying (about -0.6 mm day^{-1}) occurring in the Region I and II. This is consistent with the majority of numerical experiments that examine the effect of deforestation on climate by assuming conversion of forests into croplands with higher albedo and lower roughness length (e.g., Nobre et al. 1991, Hahmann and Dickinson 1997). In contrast, the precipitation is slightly increased in the southern LPB. Thus, the horizontal precipitation gradient between the northern and the southern basins would increase because of the land cover change. This result indicates that the increases in cropland extension would make the northern LPB be slightly drier, while the southern LPB would have more precipitation. It is important to recall that these are idealized simulations and the results need to be taken under these limitations. The conversion of evergreen broadleaf forest to dry cropland and pasture is a commonly assumed scenario in most of the deforestation experiments, which find that deforestation yields significant reduction in precipitation. Similar results were obtained also in this study.

The reduced (increased) precipitation in the northern (southern) LPB is statistically significant. However, the statistical significance of precipitation is somewhat lower than that of 2-m temperature and 10-m wind (see Appendix B). This can be attributed to the fact that, in general, precipitation does not necessarily follow Gaussian probability distributions. Nevertheless, statistical significance of the change in surface

precipitation due to land cover conversion is over 90%. While the effect of the LPB land cover change on the near-surface temperature is mainly limited to the basin, the effect on the precipitation is not restricted to the basin but also over large downstream areas.

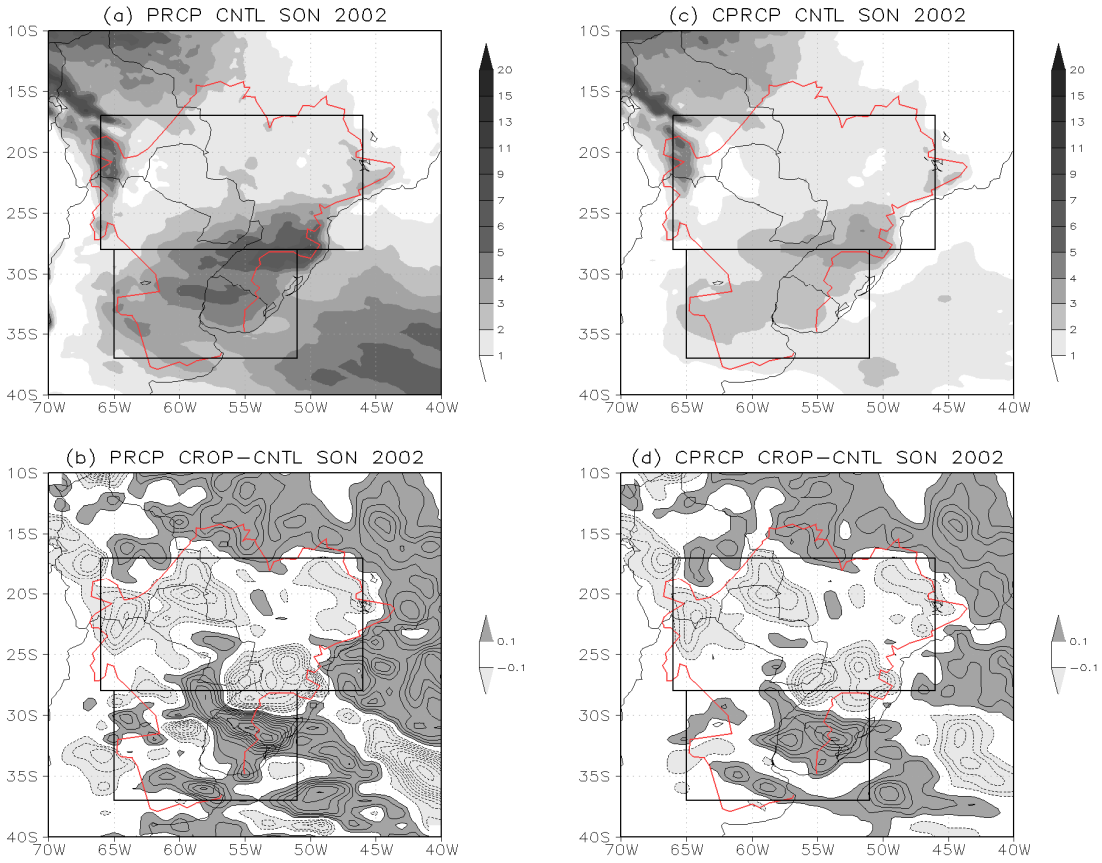

Figure 4.14: (a) Three-month (SON 2002) average of total precipitation in mm day^{-1}. (b) CROP-CNTL difference in total precipitation in mm day^{-1}. (c)-(d) as (a)-(b) but for the convective component of the total precipitation. The contour interval is 0.1 mm day^{-1} and the zero contours are suppressed.

Thus, the change in precipitation induced by the land cover modification and its physical mechanism over LPB can be summarized as follows. An extreme agricultural activity implies that the northern part of the basin changing from “forests and

savanna" to "croplands" would have an overall increase in albedo and reduced surface friction. These two changes lead to a reduction of sensible heat and surface temperature, and a somewhat higher evapotranspiration due to reduced stomatal resistance and enhanced 10-m winds. The effect on sensible heat seems to dominate and yield a reduction in convective instability. The stronger 10-m winds due to reduced friction also imply a larger amount of moisture advected out of the basin, and thus resulting in reduced MFC inside the basin. The combined effects of the two, increased stability and reduced MFC, give rise to a reduction of precipitation. On the other hand, the southern part of the basin exhibits the opposite behavior, as "croplands" would replace "grasslands", resulting in reduced albedo, a slight increase of surface temperature and increased precipitation. Turbulent latent heat flux is enhanced in both the northern and the southern LPB by reduced stomatal resistance and strengthened near-surface winds, but such an enhancement is smaller in magnitude than that of decrease or increase in turbulent sensible heat flux.

4.5 Discussion of the NATR experiment

The scenario NATR represents a natural land cover pattern (see Fig. 4.15) where current dry croplands and cropland/woodland mosaic areas were replaced by savanna (grassland) above (below) 25° S, only within the LPB (refer to Lapola et al. 2008). The scenario CROP had three regions with changes in surface properties, i.e. Region I, II and III in Fig. 4.5a. However, the scenario NATR accompanies four different regions: the first changing from dry croplands to savanna, the second from cropland/woodland mosaic to savanna, the third from cropland/woodland mosaic to grassland, and the fourth from dry croplands to grasslands.

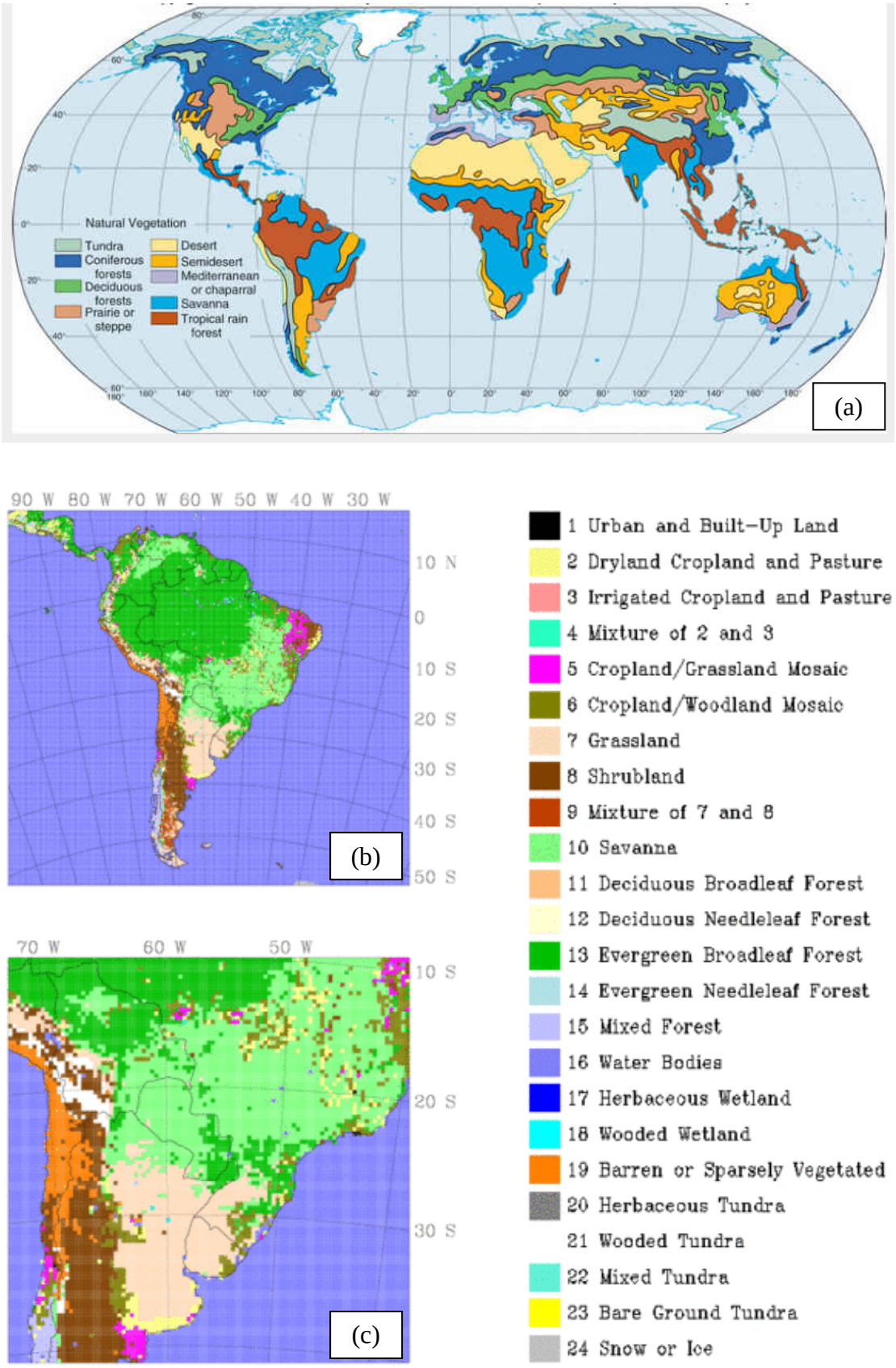

Figure 4.15: (a) A global natural vegetation map (source: http://www.geography.hunter.cuny.edu/~tbw/ncc/chap4.wc/vegetation/world.map.natural.vegetation.jpg). The natural land-use/ land cover map used for the NATR experiment on the (b) mother and (c) nested domains.

Figures 4.16a,b present the vertically integrated moisture flux and its horizontal convergence for NATR-CNTL, while Fig. 4.16c shows the total precipitation differences. An overall match between the precipitation fields and vertically integrated moisture flux convergence can be seen, as it was the case for the CROP experiment in Figs. 4.12d and 4.14b. Fig. 4.16c shows that in general the entire LPB would have a drier climate if there were no croplands. The major centers of reduced precipitation (below -0.8 mm day^{-1}) occur around Uruguay in the southern LPB. Increased precipitation also exists, for example, over Paraguay and northwest of Uruguay, but over smaller areas and with weaker intensities.

Nuñez et al. (2008)'s observational analysis suggests that the observed increase in precipitation in the northwestern Argentina is related not only with an increase in moisture transport from the Amazon but also an intensive cultivation of soy. Figure 4.16c reveals that the northern (southern) LPB would suffer from increase (reduction) in precipitation due to modern land cover effects. This implies that the increased precipitation in the Uruguay River is possible through the land cover change from the natural vegetation to the modern vegetation. In particular, this finding may have an important implication associated with the observational increase in precipitation in the Uruguay River (Saurral et al. 2008) and northwestern Argentina (Nuñez et al. 2008) during the second half of the past century. Because Saurral et al. (2008) did not allow land-atmosphere exchanges, our findings bring another view to their conclusion that the positive trend observed in the Uruguay River streamflow should be attributed to increase precipitation, rather than to land cover change.

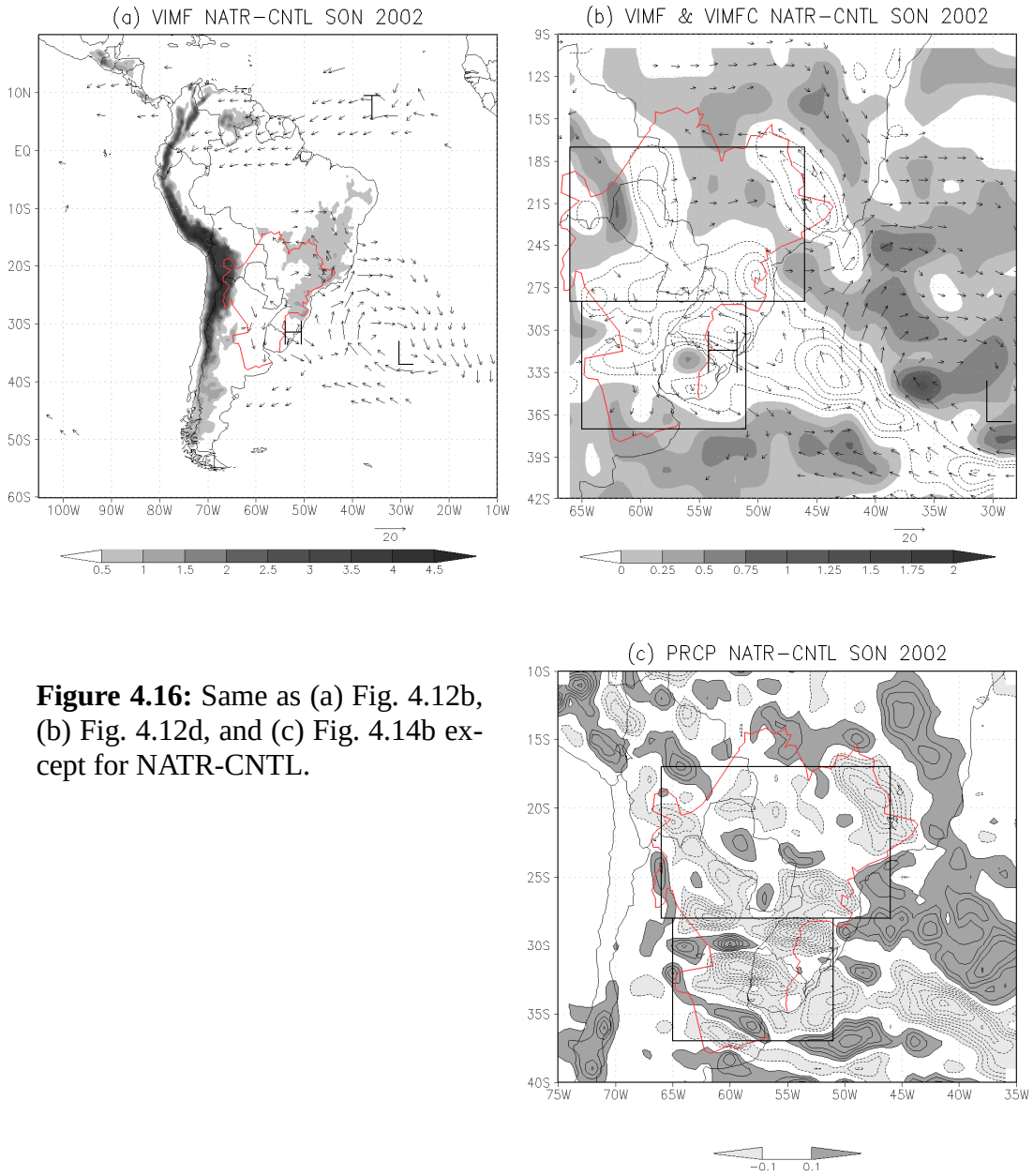

Figure 4.16: Same as (a) Fig. 4.12b, (b) Fig. 4.12d, and (c) Fig. 4.14b except for NATR-CNTL.

On the other hand, the results of Figs. 4.14b and 4.16c indicate that continued land cover changes, from natural vegetation state to current as well as from current to future, would have impacts on increasing precipitation by a maximum of about +1 mm day^{-1} in the southern LPB, especially near Uruguay. In the northern LPB, however, the impact of anthropogenic land cover changes tend to be cancelled off as time goes by from past to future through present. Namely, land cover changes from past to present would have effects on increasing precipitation, but vegetation changes from present to future would have the opposite effects in the northern LPB. By comparing the two regions, the southern LPB appears to be more vulnerable to land-cover and land-use changes, and would experience relatively bigger regional climate changes.

According to Fig. 4.16a, NATR-CNTL shows weaker impact of LULCC than CROP-CNTL inside the LPB and over the Atlantic Ocean west of the LPB, but exhibits bigger remote impacts than CROP-CNTL with the teleconnection more noticeable near equator (the region 'T'). Beltrán-Przekurat et al. (2010) mentioned that in their results the LULCC impacts were mostly limited to the areas of the land-cover changes, and assumed that remote changes would also appear in locations far from where the LULCC occurred. One of the major reasons for that may be the fact that the spatial scale of the LULCC in Beltrán-Przekurat et al. (2010) is small compared to our present study, which deals with the horizontal scale of the LULCC comparable to Rossby radius of deformation. The present study suggests that such remote responses might be possible in case of highly strong land-use and land-cover practices over LPB.

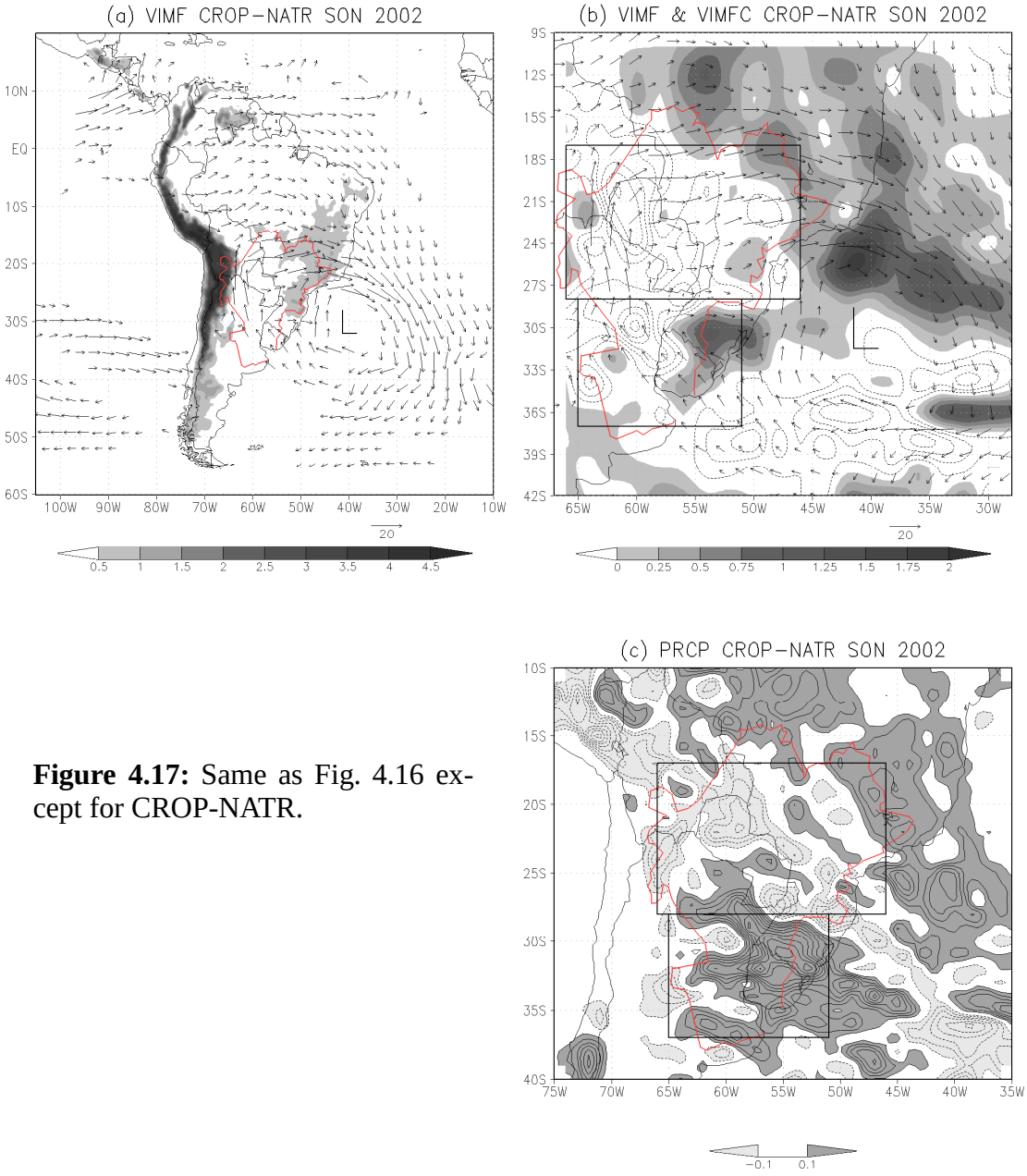

Figure 4.17: Same as Fig. 4.16 except for CROP-NATR.

Figure 4.17 is the same as Fig. 4.16 but for (CROP – NATR). Compared with CROP – CNTL, we can see more clear signals for general contribution of anthropogenic landscape changes over La Plata Basin to regional MFC and precipitation trends. Figure 4.17a shows that southerly and westerly moisture flows accelerate over the LPB due to decreases in roughness length (Table 4.2), while the moisture flows out of the basin decelerate due to increased roughness length. As a result, MFC are reduced

within the basin but are reinforced along the northeastern boundary of the basin (Fig. 4.17b). These processes produce a distinct cyclonic circulation downstream ('L' in Figs. 4.17a,b) in contrast with the two-cell structure in Fig. 16a. The southerly and westerly moisture fluxes within the basin seem to prevent the LLJ blowing from the Amazon Basin. As a result, Fig. 4.17c shows that the expansion of human-induced dry croplands would lead to an overall reduction in precipitation over the northern basin, while would result in an enhancement in precipitation over the southern basin. The latter feature is consistent with the increasing trend in observed precipitation (Fig. 1.4) and shows that observed precipitation change is partly associated with land surface changes. However, the magnitude of the observed changes is much larger than those obtained here, and the pattern is also not identical. This is partly because we ignored land cover changes outside the basin, but more basically because the observed changes seem associated to changes in large-scale forcings (e.g., Haylock et al. 2006).

4.6 Summary and conclusions

The land cover of the La Plata Basin has been subject to important changes due to agricultural practices with unknown effects to the environment. Extensive farming activities have potential impacts in the surface physical properties that may affect the basin's climate. To better understand the mechanisms by which the land surface-atmosphere feedbacks may be affected, the WRF modeling system was used to simulate idealized cases of vegetation distributions. Two idealized scenarios were considered. The first one is an intensification of the agricultural activities (replacement of natural vegetation by croplands within LPB) while the other one reflects the assumption that there were no human influences in the land cover of LPB (no croplands).

This research discusses the land-atmosphere interactions, their role in modifying the boundary layer, the effect on the convective instability and low level moisture fluxes, and ultimately, the resulting changes in precipitation. A statistical significance at the 90% level was considered for the results.

Evaluation of the model performance for the 2002 austral spring season in South America was performed against raingauge and satellite estimates of precipitation. Although not perfect, the simulations were able to reproduce all the main observed centers of precipitation. The evaluation of the 2-m temperature was also qualitatively successful in magnitude and spatial gradient within the La Plata Basin. The comparison becomes unreliable in other regions due to the lack of a proper observational network (e.g., in the Amazon basin).

The first set of experiments was prepared by assuming an increase of agricultural practices within the La Plata Basin by replacing natural vegetation (savanna, grasslands and evergreen broadleaf forest) by dry cropland. The replaced vegetation over the northern part of the basin was mostly savanna and forests, while in the southern part of the basin it was savanna and grasslands. The northern part of the basin experiences an overall increase in albedo and reduced surface friction. The changes in physical properties lead to a reduction of sensible heat and near-surface temperature, a reduction in CAPE, and MFC, resulting in a reduction of precipitation. The southern part of the basin, on the other hand, exhibits the opposite behavior, resulting in slight increase of surface temperature and increased precipitation. The reduction of 2-m temperature over the northern LPB and the enhancement of 10-m winds over the entire LPB were strong signals and statistically significant even at the 99% level of sig-

nificance. The land cover change effect on precipitation was less statistically significant compared with the near-surface temperature and winds, but it was still statistically significant at the level of 90%. Among the three replaced vegetation types, the largest change in surface climatic variables occurs in regions with changes from evergreen broadleaf forest to dry cropland. This suggests that over those regions potential future agricultural practices may have a larger impact on the local surface energy balance and the entire LPB climate.

The second set of experiments replacing croplands by natural vegetation showed that the LPB would have a drier climate if there were no human landscape practices. Combined results of the two scenarios show that land cover changes from past to present would increase precipitation, but vegetation changes from present to future would have the opposite effects in the northern LPB. All these things may imply that the southern LPB would be more sensitive to land-cover and land-use changes, and would experience relatively bigger regional climate changes.

It is shown that the land cover change in the LPB may affect remote places as well as downstream, indicating that extensive land-cover changes with a spatial scale similar to that of the Rossby radius of deformation in mid-latitudes during austral spring season can teleconnect to other regions.

Chapter 5: Incorporation of Ecosystem Functional Types in the WRF Model

5.1 Motivation

In exchanges of heat, moisture and momentum between land and atmosphere, vegetation information is important in establishing the partitioning of surface sensible and latent heat flux, and affects the near-surface mass and wind variables. Values of 2-m temperature, 2-m specific humidity and 10-m wind are associated with the vegetation characteristics like albedo, roughness length, leaf area index, vegetation fraction etc. Moreover, the influences of vegetation in the near-surface are transferred to the planetary boundary layer (PBL) and even to higher levels in the free atmosphere by turbulence processes and meso-/large-scale atmospheric circulations.

For observational and modeling studies on the land surface changes, satellite-derived information has been playing a crucial role in upgrading the quality of land surface data (e.g., Anderson et al. 1976). In order to replace the existing ground-based land cover data by remotely sensed data, many efforts have focused upon using satellite-based land cover data in the numerical models. For instance, Oleson et al. (1997) carried out stand-alone model runs using two satellite-derived maps and a global land-cover dataset commonly used in GCMs, and showed that the partitioning of net radiation into sensible and latent heat fluxes was different for the two satellite-derived datasets. Kurkowski et al. (2003) implemented satellite-derived land cover data in the Eta Model (Black 1994) and showed that use of the near-real-time vegetation fraction

data from the National Oceanic and Atmospheric Administration's Advanced Very High Resolution Radiomenter (AVHRR) data improves the forecasts of both the 2-m temperature and dew point temperature for much of the growing season. Yucel (2006) implemented the Moderate Resolution Imaging Spectroradiometer (MODIS) land cover and albedo in the fifth-generation Pennsylvania State University–National Center for Atmospheric Research Mesoscale Model (MM5) (Grell et al. 1994) at two contrasting U.S. regions and showed remarkable improvements in near-surface temperature and humidity at both study areas. Ge et al. (2008) also incorporated the MODIS data of leaf area index and vegetation fractional cover in the Regional Atmospheric Modeling System (RAMS) (Pielke et al. 1992) and showed that the spatial, seasonal, and diurnal characteristics of the model land surface temperature were improved because of MODIS data.

However, AVHRR (USGS) land-cover dataset, a default dataset traditionally used in most meteorological modeling systems including the WRF model, is based on a land-cover classification dictated by "structural" attributes of vegetation, and therefore have a high inertia to rapid environmental changes (Alcaraz-Segura et al. 2009). The number of land-cover/land-use types is also rather small: for example, 15 types in ECOCLIMAP (Champeaux et al. 2005), 17 IGBP types (Belward et al. 1999; Scepan 1999), and 24 USGS types (Loveland and Belward 1997). The number of land-cover/land-use types is related with spatial heterogeneity in ecosystem functioning, and we would lose heterogeneity information with smaller number of types. According to Pielke (2001), the shape of the surface heterogeneity strongly affects the ability of mesoscale atmospheric flows to accumulate CAPE within local regions so as to permit a greater likelihood of stronger thunderstorms. To overcome these drawbacks,

some ecologists (e.g., Paruelo et al. 2001, Alcaraz-Segura et al. 2006, 2009) proposed a new land-cover classification called *Ecosystem Functional Types (EFTs)*, where the land-cover classification is dictated by "functional" attributes of vegetation and has a sensitivity to rapid environmental changes. The idea is representing the earth's land surface in terms of ecosystem functional types rather than the current fixed structural types. For example, the behavior of rice fields and wetlands is similar, but are classified as different types in the traditional land-cover classification.

Because the EFT dataset has not been incorporated in any numerical weather or climate models, the first objective of this study is to implement it in the WRF Model as a new terrestrial boundary condition, and to estimate its impact on the climate and hydrology of the region. With this objective, numerical simulations of the WRF Model, using both USGS and EFT data, are carried out for the austral spring 1998 and are compared with observations. The present study focuses on a regional area, southern South America which has experienced significant land cover changes since the European settlement. It is also our objective to understand the physical mechanisms by which regional EFT changes give rise to changes in regional precipitation.

5.2 Methodology and data

5.2.1 The WRF model configuration

The model configuration has several differences from the previous chapter. Taking advantage of a new release, the Advanced Research WRF version 3.1.1 was used in this chapter for the numerical simulations rather than version 2.2.1. All of the simulations were performed on a two-way nested grid configuration with an outer grid of

625 x 377 points at a 30-km interval, covering the southern South America including the LPB. An inner grid with 768 x 552 points at a 10-km interval was nested to cover most of the LPB and the northern and central parts of Argentina (see Fig. 5.1). Both grids have 27 vertical levels and their thickness is geometrically increased with height**.** A 180-s time step is used on the coarse-grid domain and a smaller time interval on the inner grid. Each grid used the same vertical coordinate (27 levels). The LAI, as well as the other surface parameters, is dependent on the type of land-cover/land-use and has seasonal variations, allowing more dynamic vegetation behavior. Model physics are the same as in Chapter 4, except that the radiation scheme was replaced by a new one in WRF version 3.

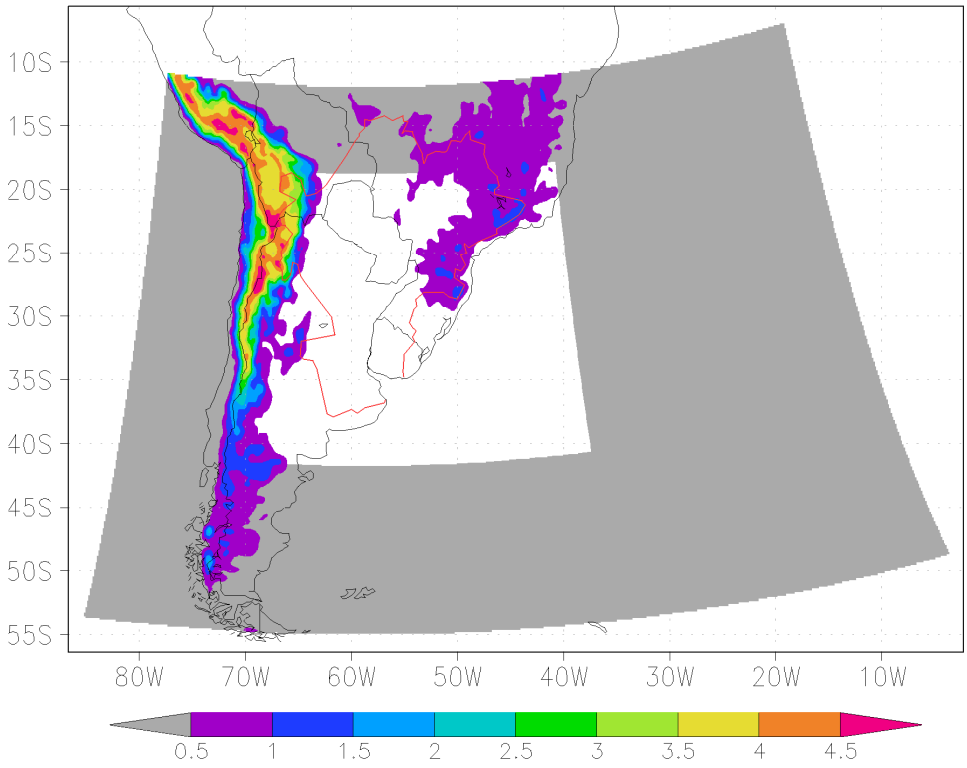

Figure 5.1: The WRF model domain configuration used in this chapter. Mother and nested domains have horizontal resolutions of 30 km and 10 km, respectively. Contour intervals for topography are indicated at the bottom in km.

Initial atmospheric fields and atmospheric lateral boundary conditions were provided by the NCEP/NCAR reanalysis (Kalnay et al. 1996). The lateral boundary update interval is 6 hour and five grid points were used for the lateral boundary nudging. Upper-air spectral nudging techniques (Davis et al. 1976, Vukicevic and Errico 1990, Waldron et al. 1996, von Storch et al. 2000) are adopted and the nudging is done at every model time step only on the coarse grid. Cut-off wave numbers used for spectral nudging are 6 and 5 in x and y directions of the domain, respectively. It is known that precipitation location biases and monsoon circulations are improved by implementing spectral nudging of the large-scale dynamics (e.g., Miguez-Macho et al. 2005, Cha et al. 2006). All these are summarized in Table 5.1.

Table 5.1: The specification of the WRF modeling system used in Chapter 5.

Grids	Double nested domain (30 km for 625x377 and 10 km for 768x552 grid points)
Numerics	Primitive equations based on the non-hydrostatic frame
Vertical resolution	27 vertical levels with model top of 10 hPa
Later boundary condition	Time and inflow/outflow dependent relaxation
Lateral boundary update	30 km : 6-hour interval by NNRPs 10 km : 6-hour interval by 30 km forecasts
Spectral nudging	30 km : cut-off wave number is 6 (5) in the x (y) direction 10 km : none
Time integration	3 months for both 30 km and 10 km meshes (180s intervals in the coarse grid)
Horizontal diffusion	Fourth order diffusion
Precipitation physics	WSM6 microphysics (Hong and Lim 2006)
Deep convection	BMJ cumulus scheme (Janjic 1994, 2000)
PBL and surface layer	MYJ PBL scheme (Janjic 1990, 1996, 2002) and MOJ surface layer scheme (Janjic 1996, 2002)
Land surface physics	NOAH LSM (Chen and Dudhia 2001)
Short wave radiation	Dudhia shortwave scheme (Dudhia 1989)
Long wave radiation	New RRTM (Mlawer et al. 1997)

5.2.2 Land cover data

The WRF model, which was adopted in this study, allows the use of 17-category MODIS land cover data in replacement of the traditional 24-category USGS land cover data. The default land-cover dataset in the WRF Model is based on the USGS global 1-km land-cover map (Anderson et al. 1976) produced from the National Oceanic and Atmospheric Administration (NOAA)'s Advanced Very High Resolution Radiometer (AVHRR) measurement (Loveland and Belward 1997) from 1992 – 1993 data. Surface properties such as vegetation and soil moisture data are prescribed following 24 unique USGS land-use categories with different surface albedo, moisture availability, emissivity and roughness values assigned to each category. The other land-cover dataset in the WRF model is based on data from the National Aeronautics and Space Administration (NASA)'s Moderate Resolution Imaging Spectroradiometer (MODIS) measurement, and was implemented by Yucel (2006). The MODIS land cover dataset has 17 USGS land-cover types which were translated from the International Geosphere-Biosphere Program (IGBP) classes.

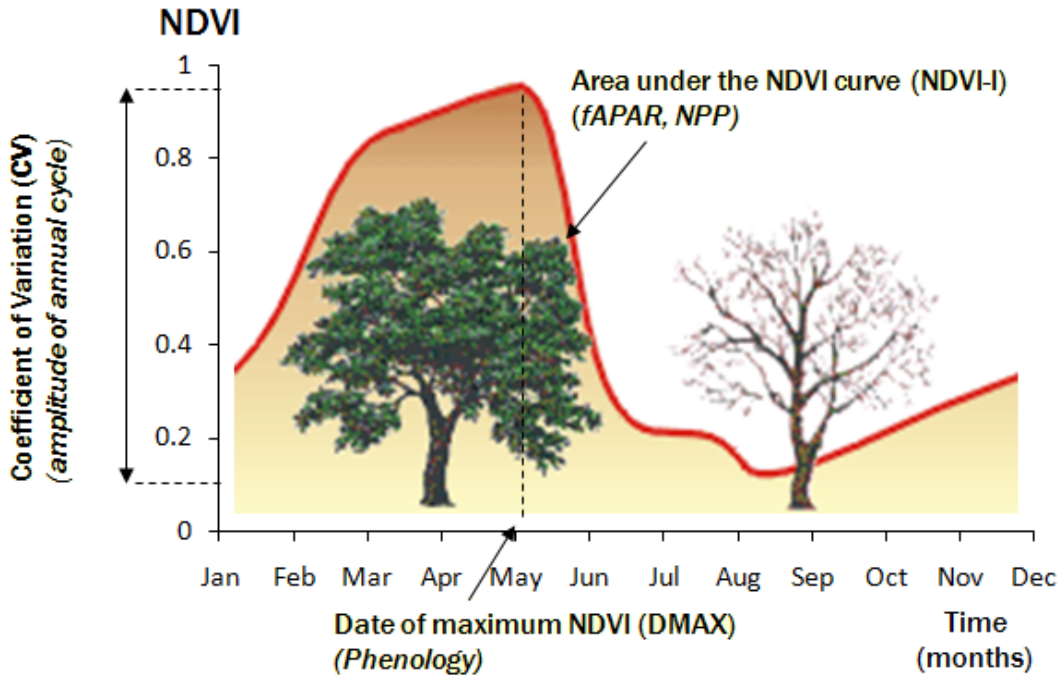

Figure 5.2: A schematic diagram illustrating the seasonal curve of Normalized Difference Vegetation Index (NDVI) and the three components which are used to define Ecosystem Functional Types (EFTs) (Paruelo et al. 2001, Alcaraz-Segura 2006).

EFTs are different from Plant Functional Types (PFTs) which are groups of plants that have similar functioning (N fixation, photosynthetic pathways, etc.). EFTs are groups of ecosystems that share functional characteristics in relation to the *amount* and *timing* of the exchanges of matter and energy between the biota and the physical environment, showing a coordinated and specific response to environmental factors. PFTs identify the functioning of a plant and assign those attributes to a region with those plants (e.g. tree → forest), thus the bottom-up denomination. EFTs are computed from satellite information (NDVI), so they do not identify the functions of a given plant, but instead identify an ecosystem that has homogeneous properties in terms of exchanges of energy and mass over a given region (top-down approach) (Alcaraz-Segura et al. 2010, manuscript in preparation). In the EFT system, 64 EFTs are identified using "three descriptors" of carbon gain dynamics derived from *seasonal curves* of Normalized Difference Vegetation Index (NDVI). The three descriptors are (1) *annual mean*

(**NDVI-I**, surrogate of primary production), (2) *amplitude of annual cycle* or *coefficient of variation* (**CV**, indicator of seasonality), and (3) *date of maximum NDVI* (**DMAX**, descriptor of phenology) (Paruelo et al. 2001, Alcaraz-Segura et al. 2006). Figure 5.2 shows a simplified example for the seasonal curve of NDVI and the corresponding three descriptors. NDVI-I, CV, and DMAX capture 95% of the variance in a Principal Component Analysis of NDVI (Alcaraz-Segura et al. 2006, 2009). For details, refer to Soriano and Paruelo (1992), Paruelo et al. (2001), and Alcaraz-Segura et al. (2006).

In order to assign land-surface physical parameters to each EFT, 1-km horizontal resolution dataset of the 1992 USGS global land-cover map was used. From the *1-km global land-cover map*, the corresponding *15 land-surface parameter maps* based on the Noah land-surface model parameterization for the 1992 USGS land-cover classes were obtained. Then, the 15 parameter maps are spatially superimposed to *the EFTs classification* for the year 1992 to spatially extract the mean land-surface parameter values of each EFT. To show the spatial effect between the two approaches, the *relative difference* between the mean EFT- and USGS-derived parameters was estimated using a formula (USGS-EFT) / USGS * 100. Characterization of the *inter-annual variability* of the land surface properties is based on the year-to-year changes in the EFT distribution from 1982 to 1999 and the former land-surface parameterization of each EFT. Both the coefficient of variation (standard deviation divided by mean) and the inter-quartile range divided by median were computed for each land-surface parameter as relative descriptors of the inter-annual differences. The *cumulative inter-annual variability* was also evaluated across all parameters (Alcaraz-Segura et al. 2010, manuscript in preparation).

Figure 5.3 displays the USGS land-cover map, derived from the AVHRR data, through the 30- and 10-km model domains. The USGS terrestrial datasets of 10' and 5' resolutions were used for the coarse and fine domains, respectively. In the figure, about 10 types among 24 types are seen in both domains, and somewhat detailed land-cover distribution is seen at the finer resolution. With USGS, we have a tile with a combination of LULC types for each grid box. With EFTs, we pick only one EFT for each grid box.

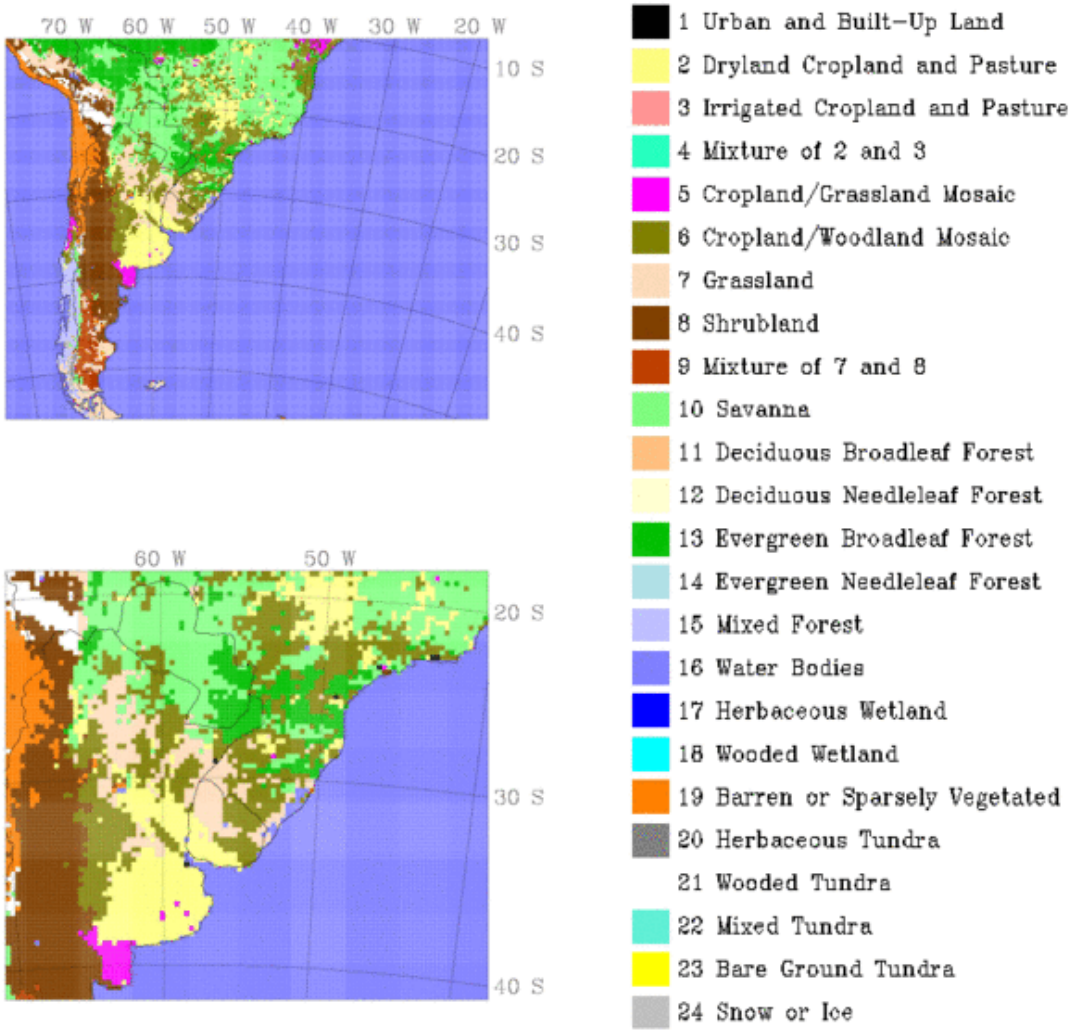

Figure 5.3: Land use/land cover maps used for CNTL. Left panels show the mother and nested domains.

Figure 5.4 displays the EFT map, derived from the NDVI data, in the model domains. Unlike Fig. 5.3, all 64 EFT categories are seen in both domains with larger (smaller) values indicating higher (lower) productivity of the surface vegetation. In Fig. 5.4, orange (brown) colored regions means high (low) net primary productivity. In contrast with the Andes Mountain ranges and Patagonia, vigorous vegetation activities can be seen over the LPB, especially, the central and southern Paraguay.

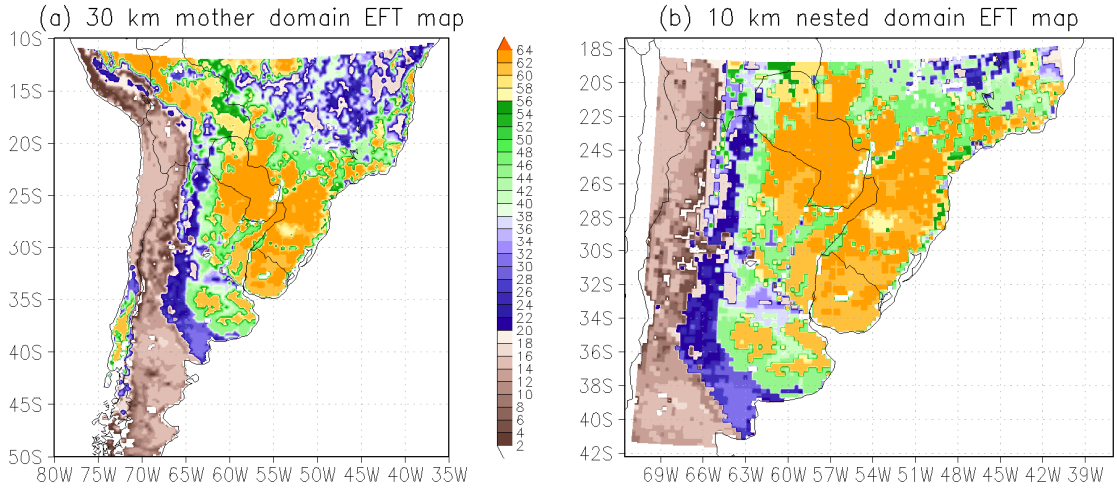

Figure 5.4: Same as Fig. 5.3 but the ecosystem functional type map.

5.2.3 Design of experiments for EFT impact

WRF simulations consisted of two kinds of land cover datasets covering the period from September to November 1998. The control run (CNTL) represented a model simulation with the default USGS land cover map (Fig. 5.3) in which there are various kinds of human-induced vegetations (dry cropland, irrigated cropland, and their mixture) as well as natural vegetations (Savanna, evergreen broadleaf forest and grasslands in the northern, central, and southern parts of LPB, respectively).

In the experimental run (called EFT), we use the EFT map (Fig. 5.4) replacing the existing 24 USGS land-cover types by 64 EFTs. In order to scrutinize the changes to the mechanisms that induce precipitation, we examine the surface fluxes, near-surface temperature and winds, the convective instability, and the moisture advection into the region. All simulations are conducted from 0000 UTC 1 September 1998 to 0000 UTC 1 December 1998, with NCEP/NCAR reanalysis data providing initial and 6-hourly boundary conditions. Experiment results for precipitation and 2-m air temperature are compared with observations.

Figure 5.5 displays the surface albedo and roughness length fields in CNTL and the difference EFT minus CNTL. Surface albedo is low over evergreen broadleaf forest regions in the central LPB and the Amazonia (Fig. 5.5a). The Andes mountain ranges have albedo higher than 25% with the maximum at higher latitudes south of 45° S. It can be seen over the LPB that the maximum decrease (increase) in surface albedo occurred in the southern (northern) LPB (Fig. 5.5b). On the other hand, surface roughness length shows the largest values over the evergreen broadleaf forest regions (Fig. 5.5c). It can be seen within the LPB that the maximum increase (decrease) in surface roughness length albedo took place in the southern (northern) LPB (Fig. 5.5d).

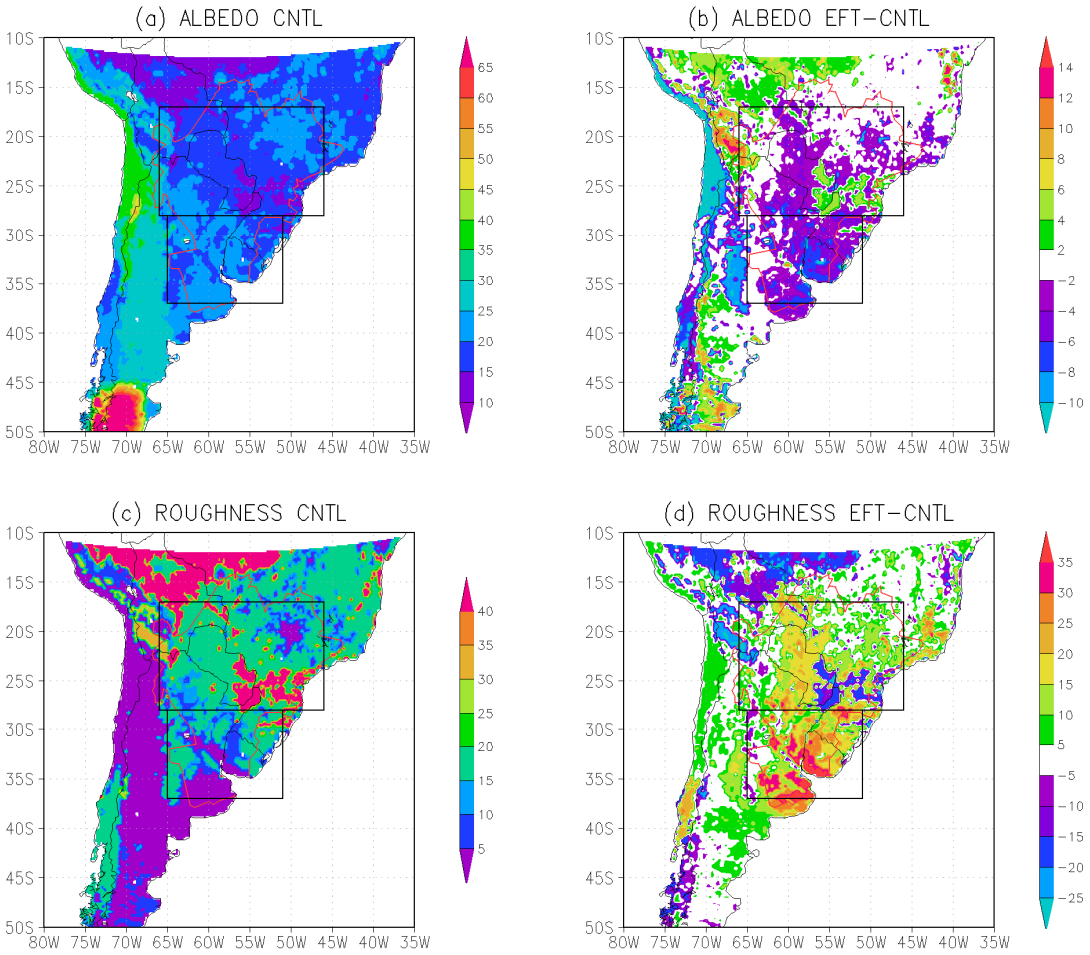

Figure 5.5: Three-month (SON 1998) averaged (a) CNTL and (b) EFT minus CNTL fields for surface albedo (%). (c) and (d) are for surface roughness length (cm).

Hereafter, the analysis focuses on the interior of the La Plata Basin which is the study interest area. To make the analysis simple, two rectangle boxes are drawn in the panels as in subsection 4.4.2. The upper box bounded by (66°W-46°W, 28°S-17°S) represents *"the northern LPB"* and the lower one bounded by (65°W-51°W, 37°S-28°S) represents *"the southern LPB"*. The latitude 28°S is properly located so that the northern LPB contains mixed albedo and the central eastern LPB has decreased roughness-length areas, while the southern LPB encompasses decreased albedo and increased roughness-length areas.

5.3 Effects of the new land-cover dataset on the numerical model simulation

5.3.1 Surface precipitation and 2-m temperature

In this subsection, model simulated precipitation and near-surface temperature results were verified against observation through frequently used two methods (bias and root-mean-square-error). Figure 5.6 shows spatial biases and root-mean-square errors (RMSEs) between simulated and observed precipitation for the whole three months (SON 1998). The figure shows that the control run has overall negative biases except in the northwestern part of the basin. In general, Fig. 5.6 indicates that model's systematic biases are improved by the new land-cover dataset with the RMSE remained practically almost unchanged. The new approach reduces model biases (i.e., systematic errors) especially in the southern LPB (Figs. 5.6a,b). On the other hand, the RMSE (i.e., total error) for precipitation differences shows mixed effects, increasing in some regions and decreasing in others. For example, the southern LPB shows reduced RMSEs, but over Paraguay the RMSE were increased (Figs. 5.6c,d). The increases in RMSE may indicate that the EFT experiment was less capable of simulating the day-to-day precipitation variability present in the observed, but may be partly related with the non-Gaussian nature of precipitation distribution. This could be clarified with other statistical measures for longer-term simulations.

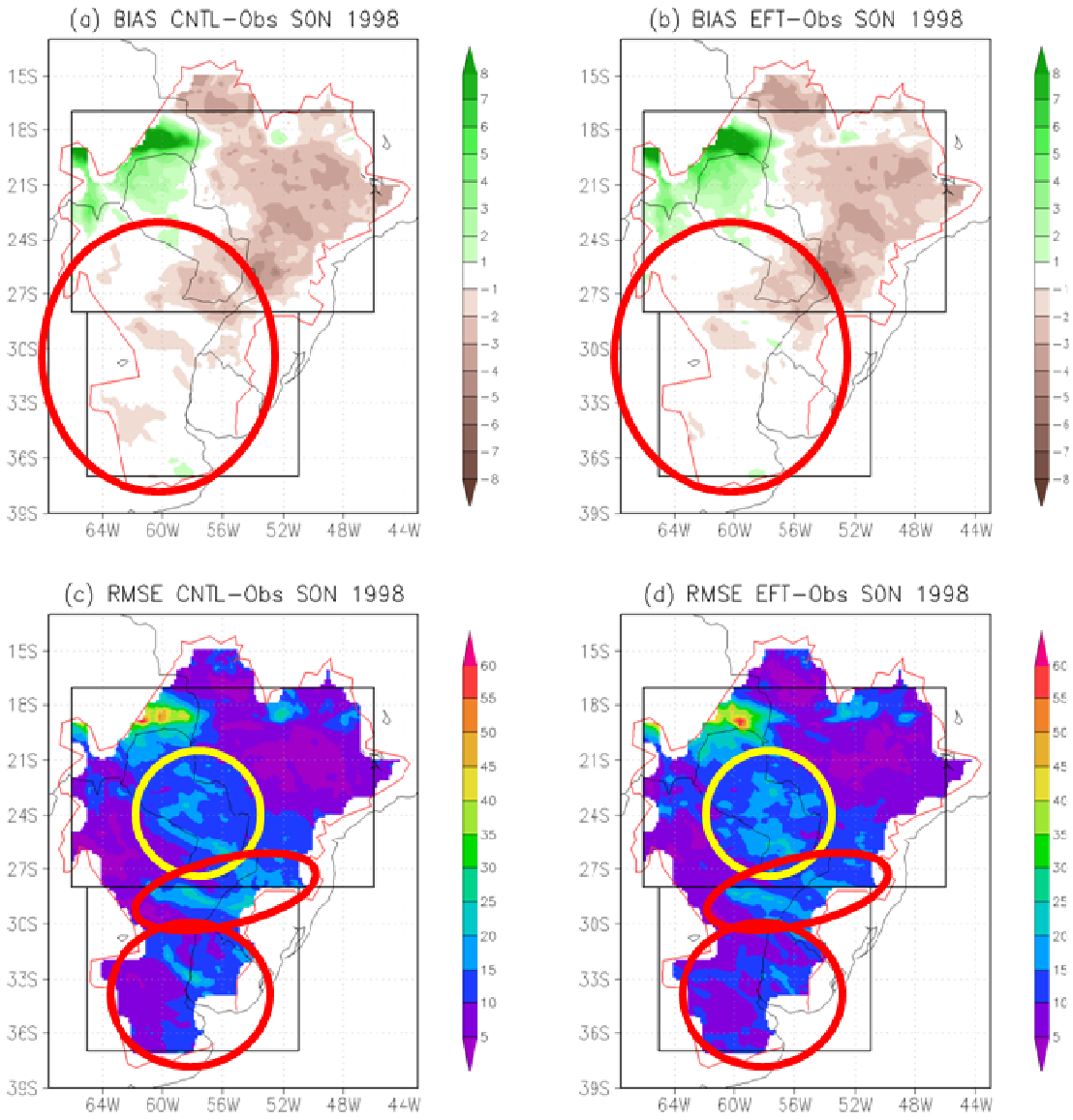

Figure 5.6: Biases in precipitation (mm day^{-1}) for (a) CNTL – TRMM and (b) EFT – TRMM. (c) and (d) are the same as (a) and (b), respectively, except for root-mean-square-error (mm day^{-1}).

Figure 5.7 shows time series of simulated and observed total accumulated precipitation over the LPB during austral spring 1998. Overall, the control run has smaller precipitation than observed except at the beginning of the simulation in early September. Such underestimation becomes clearer with time, and the difference from observed precipitation reaches about 20-30 mm at the end of November 1998. Use of EFT data in the WRF model tends to increase accumulated precipitation, and the gap between EFT and CNTL increases with time. This shows the positive benefits of using the new land-cover map to reduce the model bias, and suggests that if the simulations were extended into summer, there would be a potential improvement in summer season precipitation.

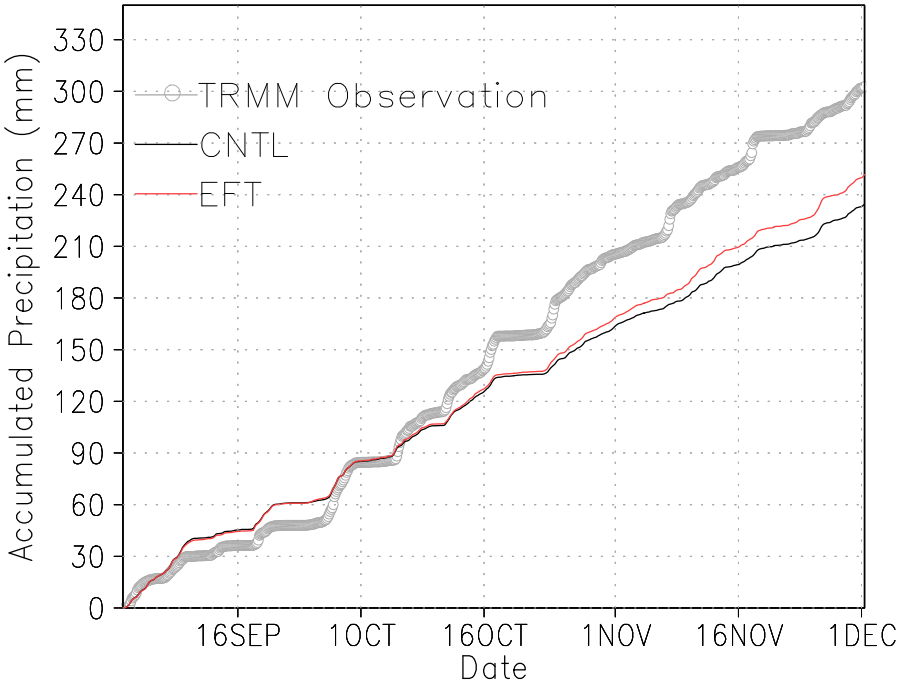

Figure 5.7: Time series of observed, CNTL and EFT accumulated precipitation (mm).

Figure 5.8 displays one-month averaged precipitation for November 1998. First, with the introduction of the new land-cover data, the areas of total precipitation over 1 mm increase in the LPB. Also, the horizontal precipitation distribution is substantially improved and the magnitude of precipitation is closer to the TRMM observation.

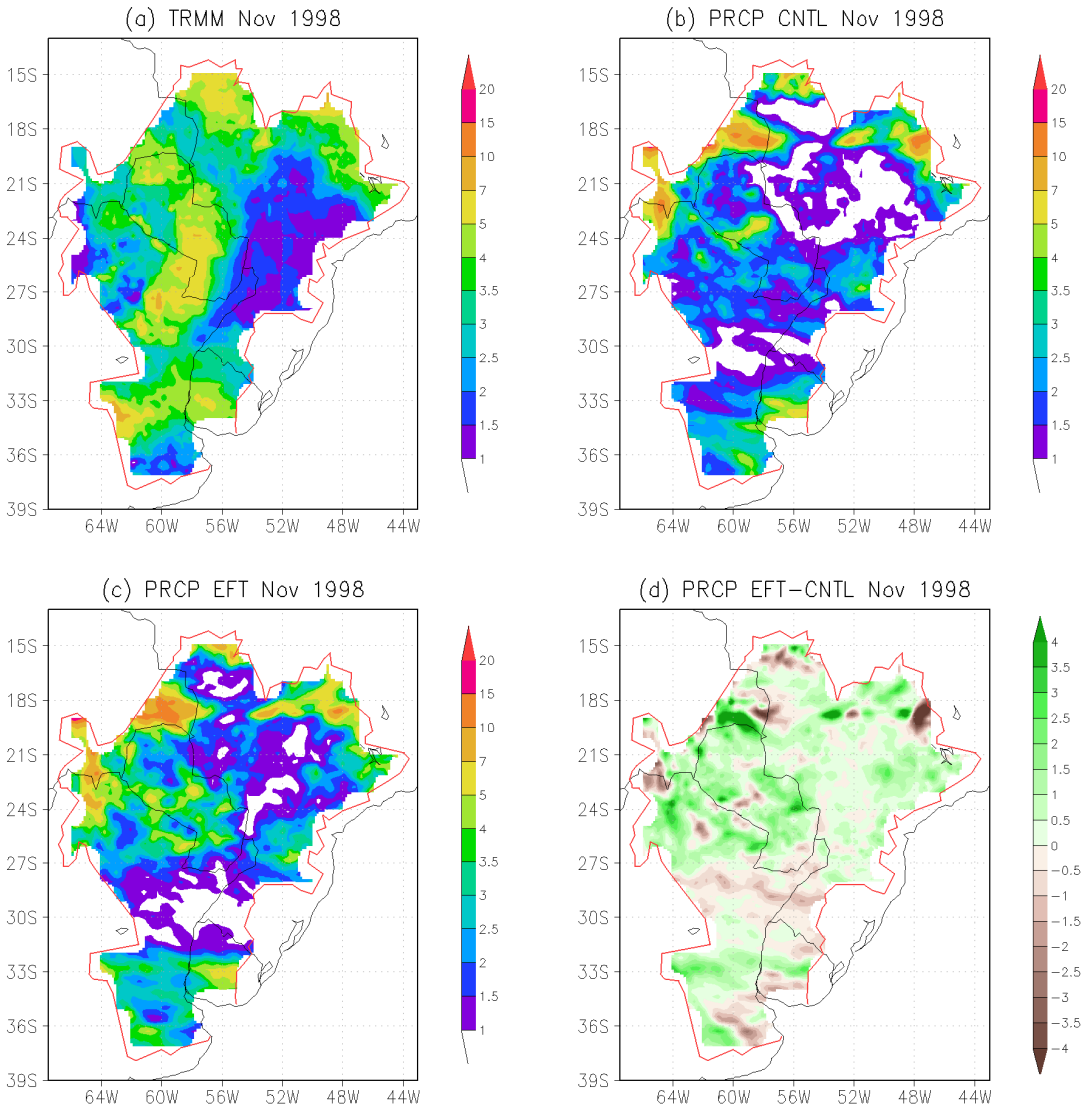

Figure 5.8: November-1998 averaged precipitation (mm day^{-1}) for (a) observation, (b) CNTL, (c) EFT and (d) EFT – CNTL.

Figures 5.9a,b display the three-month averaged field of observed and simulated 2-m temperature, respectively. Observed temperatures have maximum values around latitude 18°S and gradients of northwest-southeast directions (Fig. 5.9a). CNTL reproduces well such patterns and show reasonable consistency with the spatial distribution of observed temperature. Figures 5.9c,d display the difference of CNTL from observations. CNTL tends to have cold biases along the boundary of the LPB, while have warm biases in the southern Paraguay and north of Paraguay (Fig. 5.9c). Figure 5.9d indicates that the warm bias over the southern Paraguay and the cold bias over the Uruguay are reduced with the use of the new land-cover dataset.

Stations measuring temperature are even sparser than those measuring precipitation, and this dataset may have unreliable values over large ungauged regions, thus, the evaluation should not be more than qualitative. In order to see how the monthly mean 2-m temperature errors evolve with time, biases in 2-m temperature were calculated in the rectangle box (see location in Figs. 5.9c,d), which denotes low-altitude regions within the LPB and is thought to have better quality observation compared with mountainous regions within the basin. Figure 5.10a presents the simulated minus observed mean 2-m temperatures for each month in austral spring 1998. All the three months have biases ranging from about -0.7 to 0.4 °C, and October has the largest magnitude among them. The CNTL run has negative residuals in the first two months and then positive residuals. The EFT run has the same phase but has smaller amplitudes than CNTL in all the three months. Consequently, use of EFT data instead of USGS land cover types in the model reduced biases in monthly mean 2-m temperature over the LPB by on average 54% (89%, 14% and 60% for each month) in spring

1998. There was also general improvement in the root-mean-square-error (RMSE), and the correction was largest during November (Fig. 5.10b).

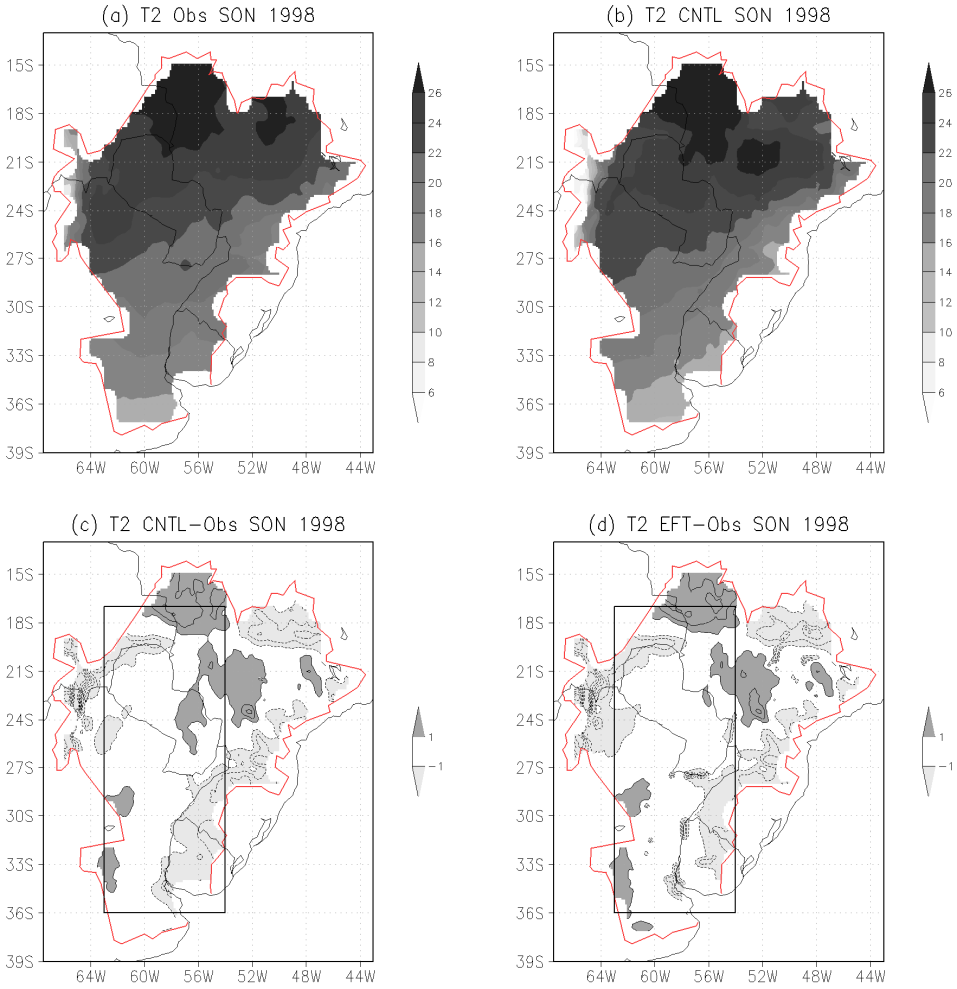

Figure 5.9: Same as Fig. 5.8 but for 2-m air temperature (°C).

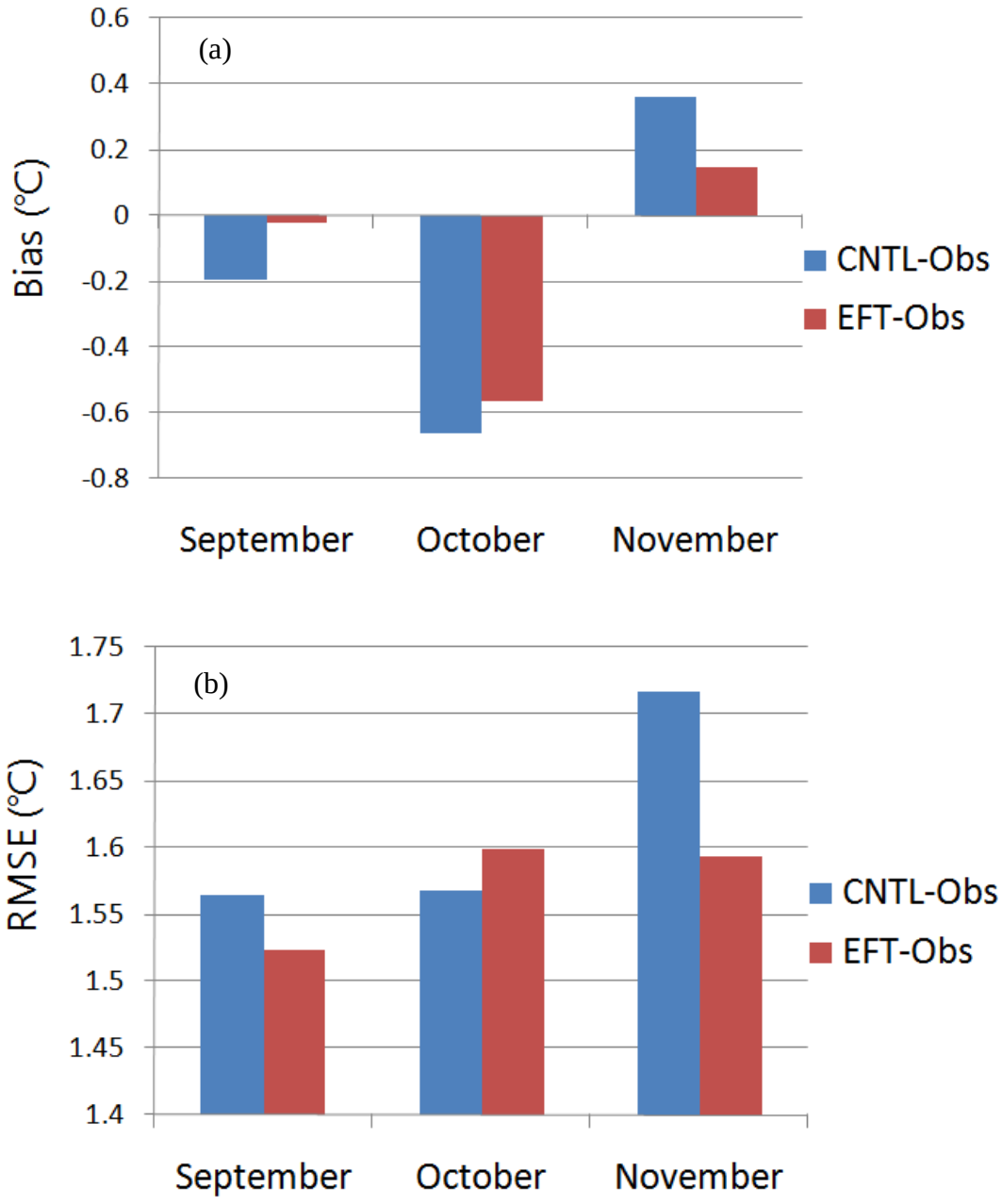

Figure 5.10: (a) 2-m temperature biases (°C) and (b) root-mean-square-error (°C) over the box area in Fig. 5.9c,d for each month during SON 1998.

In the following sections, the effect of EFTs on other variables will be discussed to understand the mechanisms involved in the reduction of the biases and RMSEs.

5.3.2 Surface heat fluxes and near-surface atmospheric variables

Figures 5.11a,b present time series of the difference (EFT minus CNTL) of the area-averaged surface heat fluxes over the two regions. In the northern LPB, the replacement of the USGS land-cover map by the EFTs produces a decrease in sensible heat fluxes due to the increased surface albedo, and an increase in latent heat fluxes. The southern LPB exhibits the opposite behavior in the sensible and latent heat fluxes time series, and the signal is relatively weak compared with the northern LPB.

The changes in the surface heat fluxes are expected to alter the near-surface atmospheric variables. This can be seen in Figs. 5.11c,d where the two area-averaged time series of the difference (EFT minus CNTL) in 2-m temperature and 2-m specific humidity. The decreased (increased) sensible heat fluxes in the northern (southern) LPB give rise to a cooling (warming) near the surface (Fig. 5.11c). The magnitude of the cooling is up to 0.5 °C, while the amount of the warming is below 0.8 °C. On the other hand, the increase in latent heat fluxes in the northern produces the increase in specific humidity near the surface (Fig. 5.11d). In the southern LPB, the latent heat fluxes are reduced but the corresponding 2-m specific humidity shows almost neutral changes. This is explained by the fact that 2-m specific humidity is dependent on near-surface temperature and winds as well as latent heat fluxes.

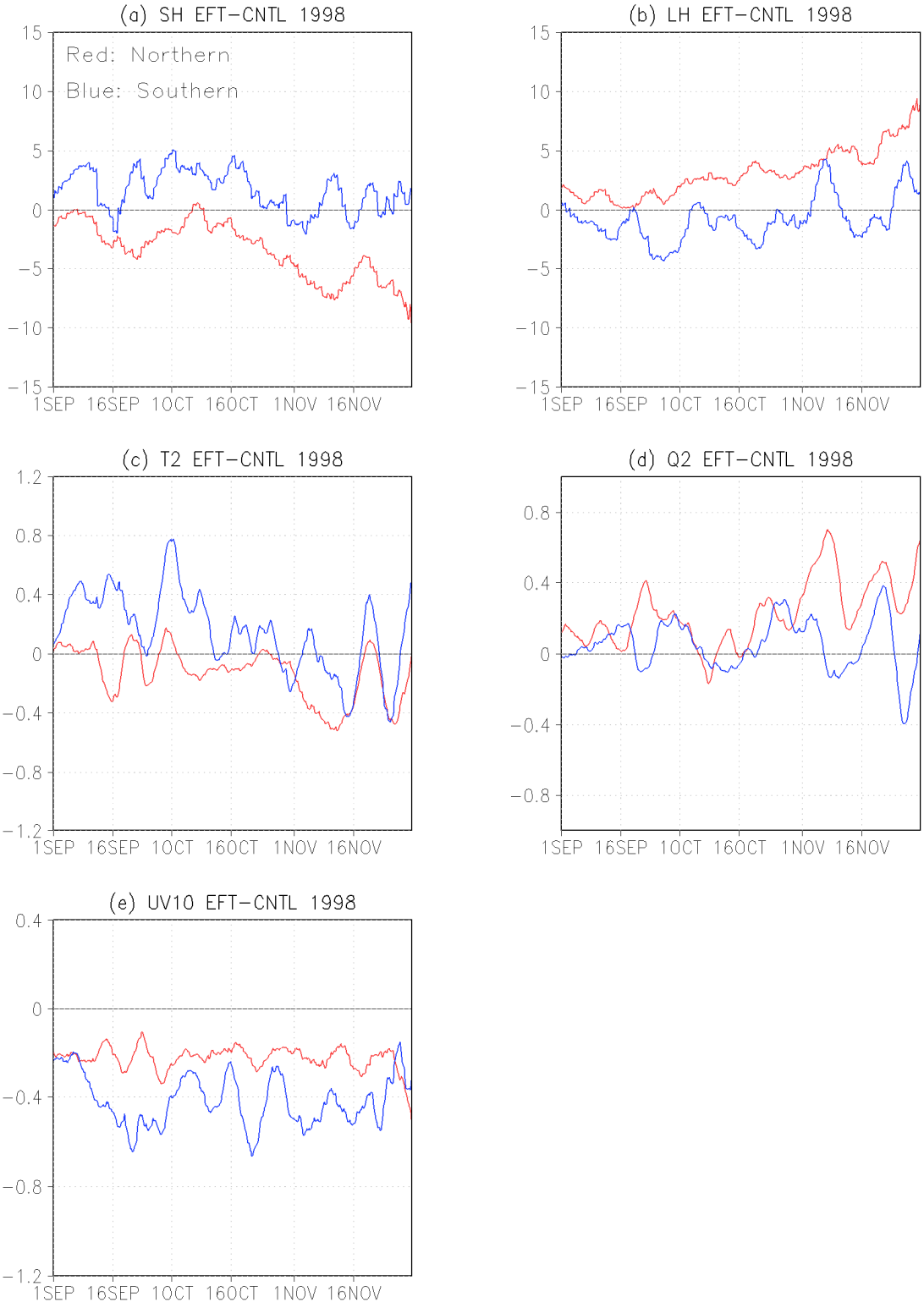

Figure 5.11: Time series of (a) sensible heat fluxes (W m^{-2}), (b) latent heat fluxes (W m^{-2}), (c) 2-m temperature (°C), (d) 2-m water vapor mixing ratio (g kg^{-1}), and (e) 10-m wind speed (m s^{-1}). All are 5-day running averaged.

Roughness lengths play a crucial role in determining near-surface wind direction and speed. The increase of the roughness length forces a reduction of 10-m wind speed in both northern and southern LPB regions (Fig. 5.11e). The southern LPB exhibits a larger decrease in near-surface winds since the maximum increase in surface roughness occurs there. It is noted that the magnitude of the difference in wind speed does not exceed 1 m s^{-1} in the original time series without 5-day moving average (not shown), but the effect is very systematic and lasts during much of the model integration period.

Figure 5.12 shows the 3-month average of the 10-m wind fields over the LPB. Figure 5.12a shows that winds have a strong easterly component under the USGS land cover condition. However, the easterly wind decreases (westerly anomalies) with the use of EFTs especially in the southern LPB (Fig. 5.12b). Although the alteration of near-surface winds is shown at 10-m height, the changes in lower-level winds are expected to modify higher-level wind flows and distributions.

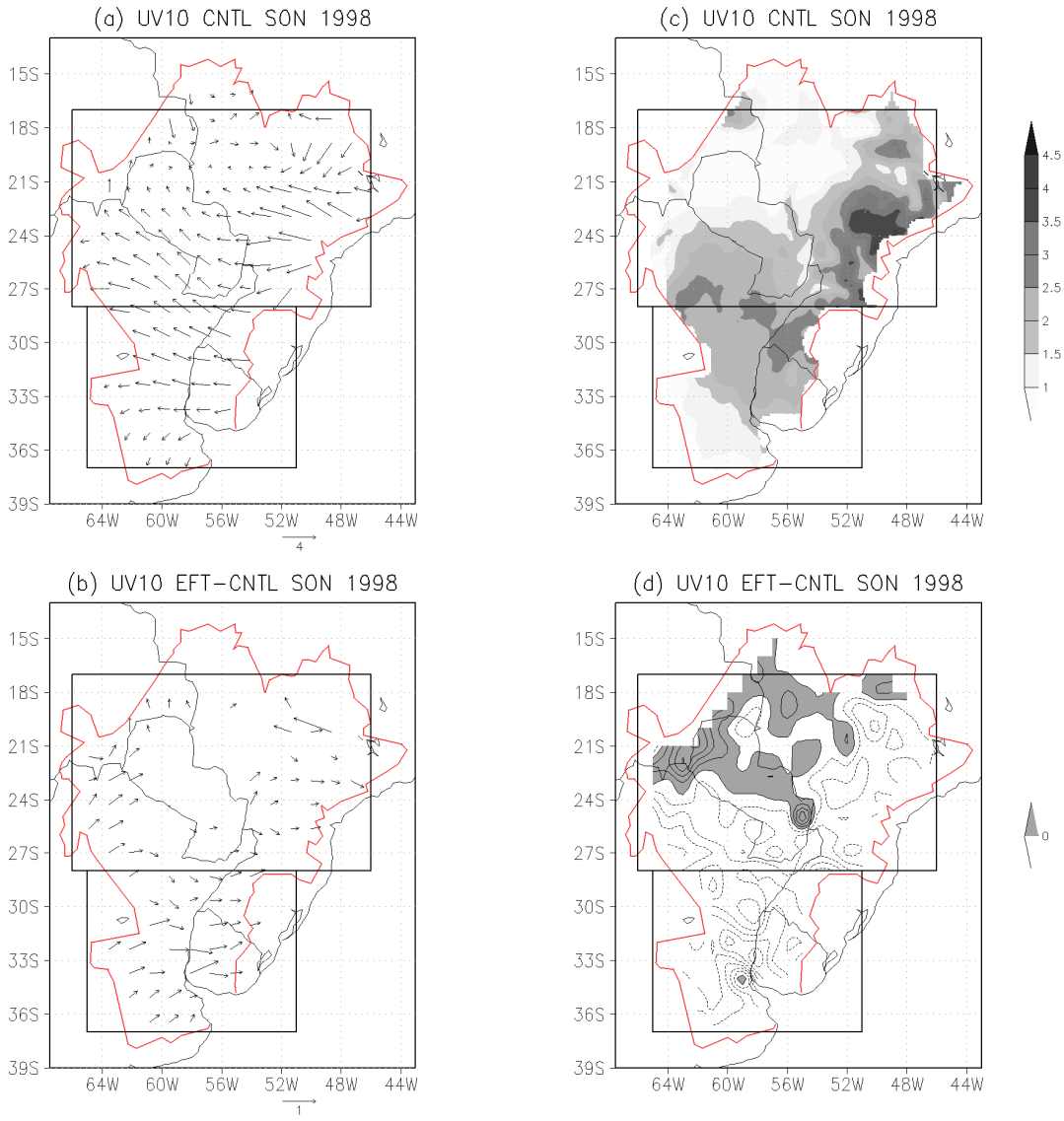

Figure 5.12: Three-month (SON 1998) averaged (a) CNTL and (b) EFT minus CNTL for 10-m wind vector fields (m s^{-1}). (c) and (d) are for 10-m wind speed, and contour intervals in (d) are 0.1 m s^{-1}.

5.3.3 Local thermodynamic forcing

The changes in the low level atmospheric conditions (e.g., 2-m T and 2-m Q) are expected to induce changes in atmospheric instability. Figure 5.13 displays the simulated 3-month average of the MCAPE and MCIN fields. In general there is relatively large MCAPE and MCIN over Paraguay in the control run (Figs. 5.13a,b).

The difference field (EFT-CNTL) shows that use of the new land-cover map would increase MCAPE in the northern LPB including Paraguay, while it would slightly decrease MCAPE in the southern LPB (Fig. 5.13c). The increase in MCAPE in the northern LPB (Fig 5.13c) is associated with the increase in the latent heat flux (Fig. 5.11b). Figure 5.13d shows that use of the new landscape data decreases MCIN in the southern LPB, but has neutral impact in the northern LPB. Because large values of CAPE and small values of CIN are favorable conditions for local convection and precipitation, the increased CAPE over the northern LPB implies a higher possibility of the development of Mesoscale Convective Systems in the region, especially around Paraguay.

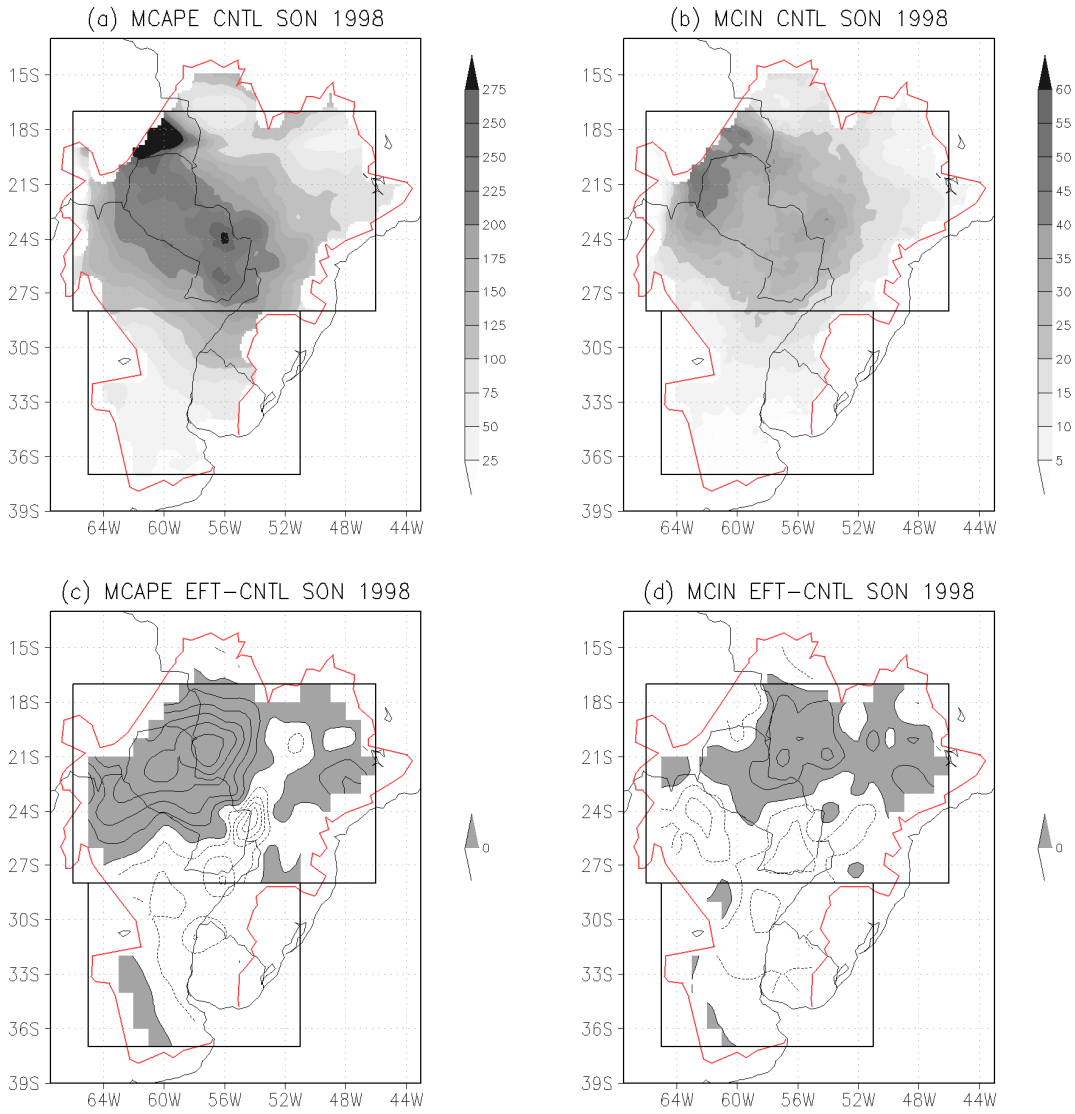

Figure 5.13: Three-month (SON 1998) averaged CNTL for (a) maximum CAPE (MCAPE) and (b) maximum CIN (MCIN) (Units: J kg^{-1}). (c) and (d) are for EFT minus CNTL, and contour intervals are 10 J kg^{-1} and 2 J kg^{-1}, respectively.

5.3.4 Large-scale horizontal moisture flows

The local thermodynamic instability alone cannot fully explain the changes in precipitation in the LPB. The change in surface precipitation is also the consequence of the alteration in moisture transport into the LPB. Such an alteration can be inferred from the previous section (Fig. 5.12), where the reduction of near-surface winds is expected to influence higher-level moisture flows and distributions.

Figure 5.14 displays the 3-month averaged moisture flux, vertically integrated from 1000 hPa to 300 hPa, and the corresponding convergence and divergence fields. The control run (Fig. 5.14a) shows consistent features with previous climatologies derived from global reanalyses (Labraga et al. 2000; Berbery and Barros 2002; Doyle and Barros 2002; Marengo et al. 2004), short-term regional forecasts (Silva and Berbery 2006), and month- or season-long simulations (Collini et al. 2008; Chapter 4). The largest southeastward moisture transport exists over the northwestern LPB including Bolivia and Paraguay (Fig. 5.14b). It supplies moisture into the LPB from the Amazon basin, whose moisture is provided from the tropical Atlantic Ocean by the trade winds.

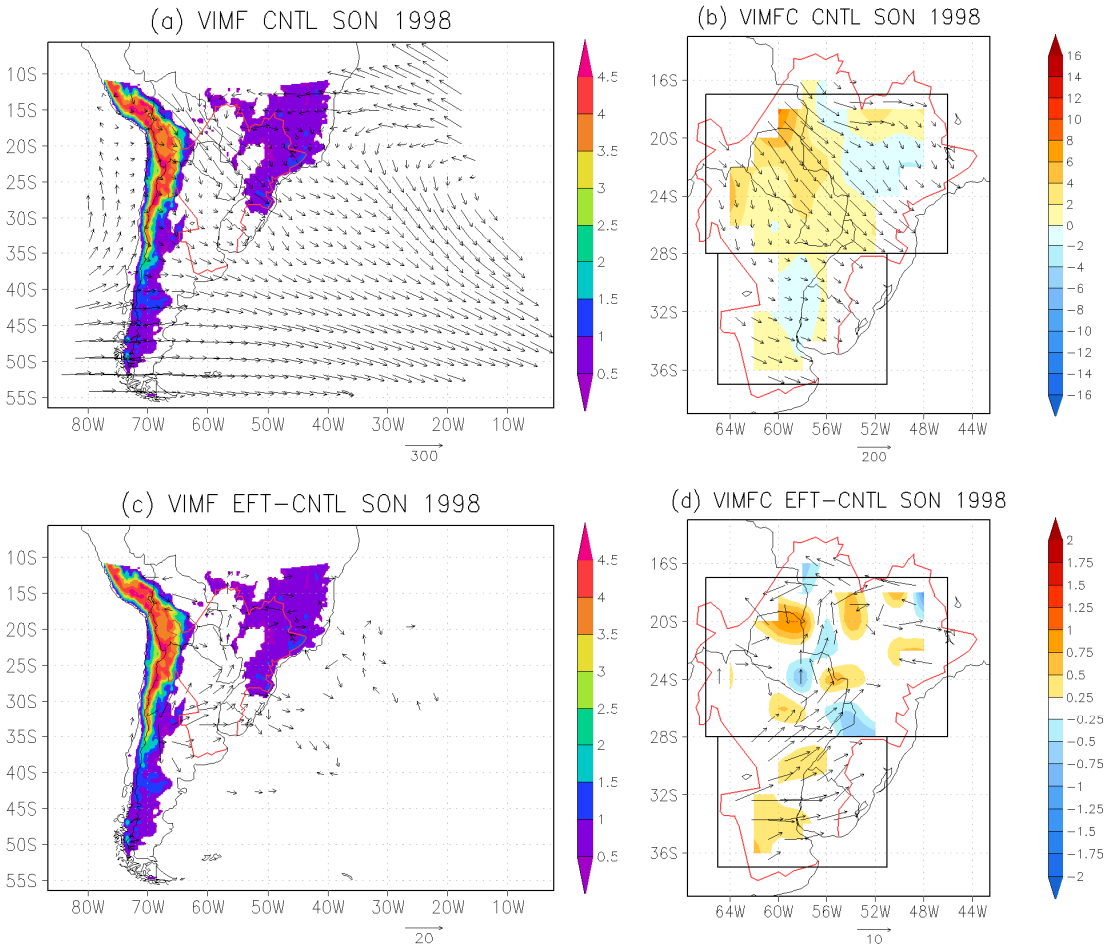

Figure 5.14: Three-month (SON 1998) averaged CNTL for (a) vertically integrated moisture fluxes in kg (m s)$^{-1}$ and (b) their convergence in mm day^{-1}. (c) and (d) are for EFT minus CNTL. Shaded areas in (a) and (c) are model terrain height (km), and the moisture flux convergence (divergence) is positive (negative) in (b) and (d).

Figures 5.14c,d show that use of the new land-cover map modifies regional moisture transports. Figure 5.14c indicates that westerly moisture flows are produced in the southern LPB and most of them turn their direction toward the north in the northern LPB. Some of the westerly moisture flows keep going eastward and create relatively small perturbations in moisture fluxes over the South Atlantic Ocean. The Brazilian Highlands seem to play an important role in the splitting of the westerly moisture flow. And then, the westerly (southerly) moisture fluxes in the southern (northern) LPB produces moisture flux convergence in the southern LPB (Fig. 5.14d). In the northern

LPB, both moisture flux convergence and divergence are produced, and on average moisture flux convergence is somewhat larger with its maximum in the northern Paraguay. All these features suggest that precipitation in the southern LPB would be supported mainly by the large-scale moisture flux convergence rather than local thermodynamic forcing because changes of MCAPE are small in the southern LPB (Fig. 5.15c).

5.3.5 Precipitation

Figures 5.15a,b display the 3-month averaged total precipitation in CNTL and the difference (EFT minus CNTL). The control precipitation field shows overall consistency with the vertically-integrated moisture flux convergence and divergence fields in Fig. 5.14b in both the northern LPB and the southern LPB. The regions of precipitation increase (decrease) are collocated with vertically integrated moisture flux convergence (divergence). The difference field (Fig. 5.15b) also corresponds well with the moisture flux convergence field in Fig. 5.14d. On the other hand, compared with the MCAPE difference field (Fig. 5.13c), the northern LPB precipitation difference corresponds well with it, but the southern LPB does not.

The total precipitation difference (Fig. 5.15b) between CNTL and EFT can be understood as the combined effects of both local (subsection 5.3.3) and large-scale (subsection 5.3.4) forcings induced by use of the new land-cover map. Figures 5.15c,d display area-averaged time series of the difference (EFT minus CNTL) in convective and non-convective precipitation over the northern LPB and the southern LPB. They reveal that the northern LPB and the southern LPB have clear differences in the precipitation type. The northern LPB exhibits increases in both convective and non-

convective precipitation with time. The southern LPB shows a similar increase as the northern LPB in non-convective precipitation but has almost no change in convective precipitation. This means that in the northern LPB both local thermodynamic and large-scale dynamic forcings are increased, while in the southern LPB only a large-scale dynamic forcing increased with the use of new land-cover map.

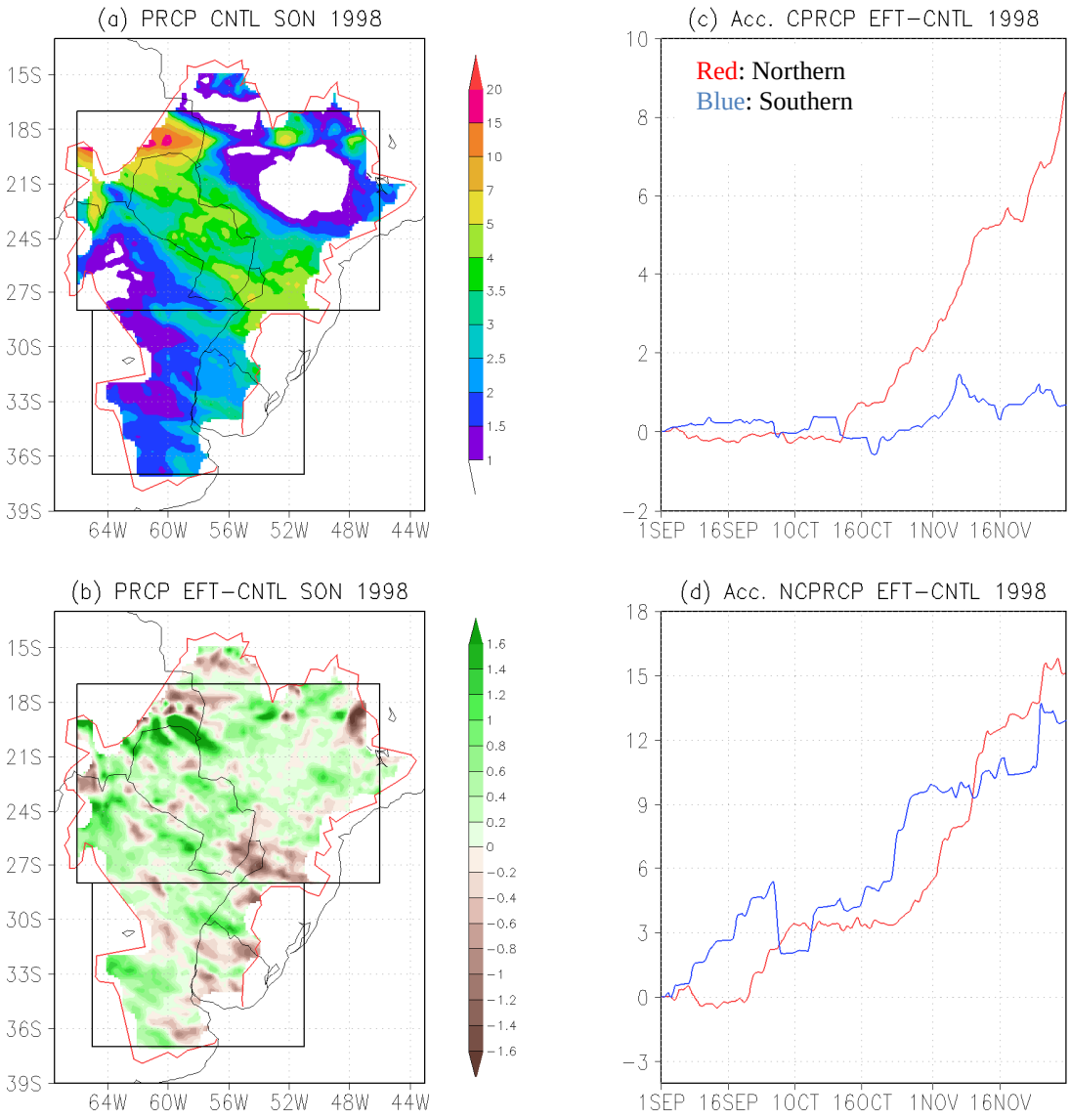

Figure 5.15: Three-month (SON 1998) averaged (a) CNTL and (b) EFT minus CNTL for surface precipitation (mm day^{-1}). Time series of three-month averaged fields of the difference (EFT minus CNTL) in (c) convective precipitation and (d) non-convective precipitation (Units: mm day^{-1}). In (c) and (d), the time series is 5-day running averaged and red (blue) color in (c) and (d) denotes the northern (southern) LPB.

5.4 Summary and conclusions

In the recent past, the accuracy of numerical weather and climate predictions and simulations has been improved with the help of the satellite-derived surface information. In this chapter, *a new concept* of a land-cover classification, called Ecosystem Functional Types (EFTs), was introduced in a numerical mesoscale model. EFTs are patches of the land-surface with similar carbon gain dynamics and consist of 64 functional categories of ecosystems. In a first approximation, the physical properties of each EFT were obtained by overlapping the land cover types and EFTs, and then assigning the properties of the given land cover type to the corresponding EFT. The effect of this incorporation on model simulations was investigated in the La Plata Basin in South America for spring 1998.

Compared with the existing USGS land-cover dataset, the use of the new data set shows substantial changes in surface albedo and roughness length fields. Such changes produce alterations in surface fluxes and near-surface atmospheric variables resulting in changes in local thermodynamic forcing and large-scale moisture flow patterns.

Through qualitative and quantitative comparisons with observations, it is found that in general the new approach improves model performance for precipitation and 2-m temperature simulations both in magnitude and spatial distribution. These encouraging results indicate the value of the EFT information and the need for weather/climate models to incorporate it to increase the accuracy of forecasts and simulations.

Chapter 6: Impact of Ecosystem Functional Type Changes on the Climate of the La Plata Basin

6.1 Background

In Chapter 4, we performed ensemble simulations for an extreme land-cover change scenario using the WRF system based on a two-way interactive nested grid. However, the scenario was based on the conventional land-cover and land-use types and assumed hypothetically idealized changes of them. In order to understand the impact of historically occurred land-cover changes on the climate of the LPB, model simulations based on actually occurred land-surface changes are required. In that sense, the EFT data, introduced in the previous chapter, can be utilized to represent more realistically the land-surface changes. The EFT data are composed of 64 types and available at 1 year interval, having the advantage of better representing diverse surface ecosystem functions and allowing a shorter and more detailed response to surface changes. Thus, applications of EFT data to diverse regional climate investigations are encouraged due to the promising results discussed in Chapter 5**.**

In Chapter 5, the EFT dataset was implemented in the WRF model system and showed that its incorporation, in replacement of the traditional USGS land cover dataset in a regional climate model, improved the accuracy in climate simulations of 2-m air temperature and surface precipitation over the LPB. This chapter, following the results in Chapter 5, aims at exploring the impact of the interannual variability of land-use and land-cover changes (using EFTs) on the climate of the LPB. For this

purpose, two numerical simulations consisting of September to November of 1988 and 1998 were performed using the EFTs corresponding to each year. Then, two other simulations for the same periods were performed but interchanging the surface conditions, i.e., the EFTs. In other words, the spring of 1988 was simulated with the EFTs corresponding to 1988 first, and then with the EFTs corresponding to 1998. The same was done for 1998. The idea was to understand how the surface conditions affected the interannual variability when the large scale forcing (through the lateral boundary conditions) remains unchanged. In order to understand the feedbacks between surface conditions and the hydrologic cycle over the LPB, the impact of the EFT changes between 1988 and 1998 on the surface heat fluxes, near-surface atmospheric variables, local thermodynamic instabilities, large-scale moisture flux convergence, and lastly surface precipitation is examined. The WRF model and its configuration are the same as in Chapter 5 (see Table 5.1).

6.2 Methodology

Currently, EFT maps are available at 1 year interval for the southern South America from 1982 to 1999, except for the year 1994 due to satellite failures. The 1988 and 1998 spring season periods were chosen for the simulation because they correspond, respectively, to low and high “net primary productivity” (low and high values of EFTs) over the LPB. Figure 6.1 shows three-month mean precipitation fields from raingauge data during September to November 1988 and 1998. General patterns in precipitation distribution are similar to each other with the largest precipitation located in the southeastern part of the LPB. Compared with year 1988, year 1998 had an overall increase in precipitation and the maximum precipitation region was some-

what shifted toward the northeast. The shift leads to a reduction in precipitation over the southern LPB and enhances precipitation in the northern LPB.

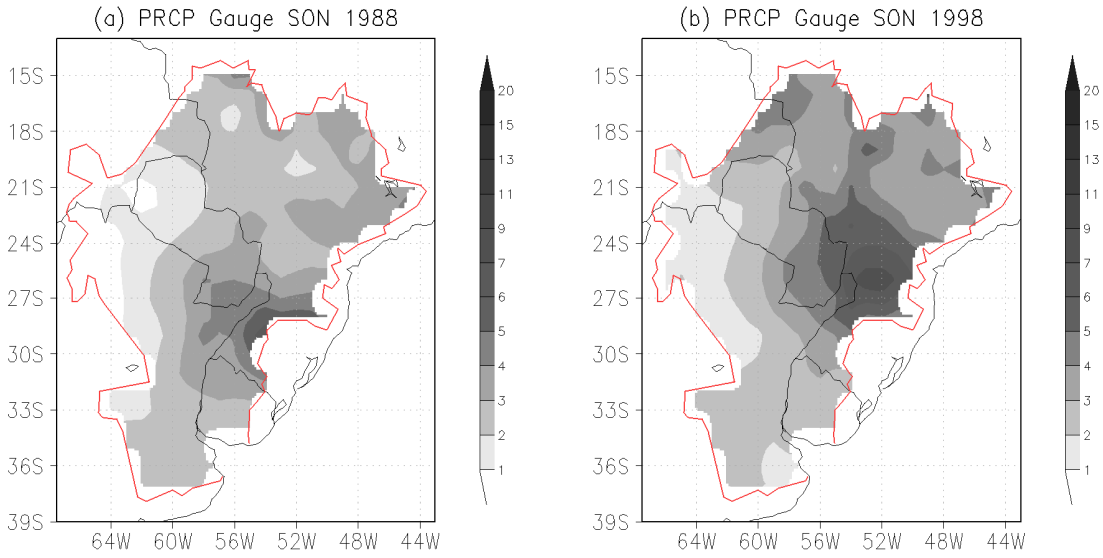

Figure 6.1: Three-month average observed precipitation for spring (SON) (a) 1988 and (b) 1998 (Unit: mm day^{-1}).

The two periods also showed very different characteristics in spatial distribution and the magnitude of EFT productivities. Figure 6.2 shows the EFT maps for the two years over coarse and fine model grids. Orange colored regions mean higher carbon productivity by vegetation, while dark brown colored regions mean lower carbon productivity. The Andes Mountain ranges exhibit very little changes in EFTs, while the LPB presents dramatic changes in the EFTs. The year 1998 had an overall higher productivity than the year 1988, and this implies that more vigorous exchanges of mass and energy existed in 1998. Hereafter, the EFT conditions in 1988 and 1998 are called “LowEFT” and “HighEFT”, respectively.

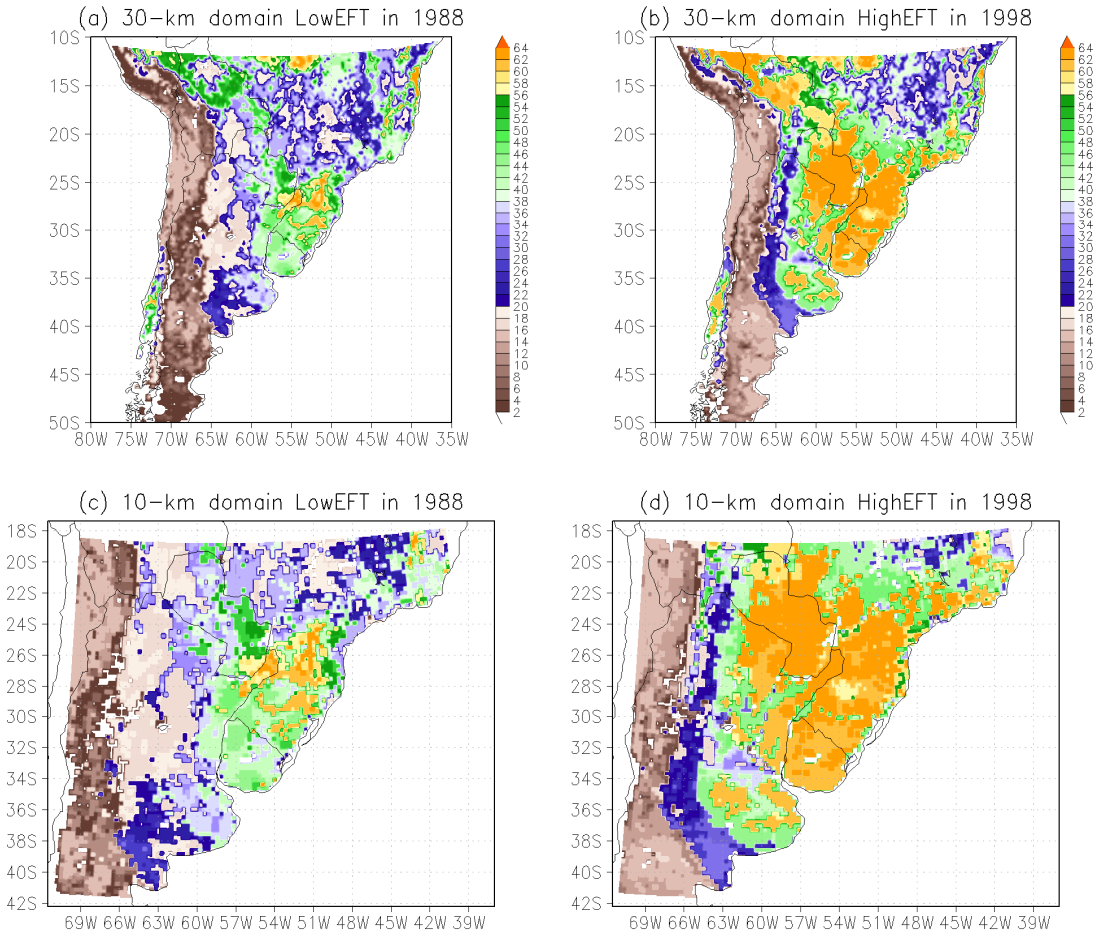

Figure 6.2: Ecosystem functional type data used for the coarse (upper) and the fine (bottom) model grids. Left (right) panels are for year 1988 EFT (1998 EFT). Orange (dark brown) colored regions denote higher (lower) carbon productivity of vegetation.

Based on Figs. 6.1 and 6.2, pairs of simulations were carried out for September-November 1988 (a dry year) and 1998 (a wet year). Within a given pair, one member employed LowEFT as the surface boundary condition, while the other used HighEFT. This experimental design permits us to examine the general impact of EFT changes on the climate of the LPB, that is, how simulation results using identical lateral boundary conditions (large scale forcing) for each year would be affected by using different land surface forcings.

6.3 Results

6.3.1 Changes in surface physical properties and surface energy balance

Figure 6.3 shows the surface albedo and roughness length fields for LowEFT and the difference (HighEFT minus LowEFT) over the LPB. Figures 6.3a,b show that in case of LowEFT, the central eastern LPB has relatively small surface albedo (< 15%) and large roughness length (> 35 cm). Compared with LowEFT, the HighEFT field generally has smaller surface albedo (Fig. 6.3c) and larger surface roughness length (Fig. 6.3d) over the LPB. In particular, the southern LPB below 27˚ S (Uruguay and its neighbor regions) has the largest decrease in albedo and the largest increase in roughness length (Figs. 6.3c,d).

Figure 6.4 illustrates the model-simulated 3-month averaged diurnal cycle of the surface energy balance over the LPB for 1988 and 1998. The simulated surface energy budget over the LPB in spring 1988 and 1998 shows that the sensible heat flux is an important energy component, and the latent and the ground heat fluxes are approximately two times smaller than the sensible heat flux (Figs. 6.4a,b). Figure 6.4b shows that the latent (sensible) heat flux is larger (smaller) in 1998, and this is because the year 1998 was a wetter year.

Figures 6.4c,d show that the EFT changes on average increase sensible heat, latent heat, ground heat and net radiation fluxes over the LPB for both dry and wet years. This is consistent with Beltrán-Przekurat et al. (2010) which showed that for land-use and land-cover change scenarios, the surface energy fluxes and temperature changes remained in general the same in two contrasting ENSO years. The increase in sensi-

ble heat fluxes due to the EFT changes is mainly associated with the decreased surface albedo as shown in Fig. 6.3c.

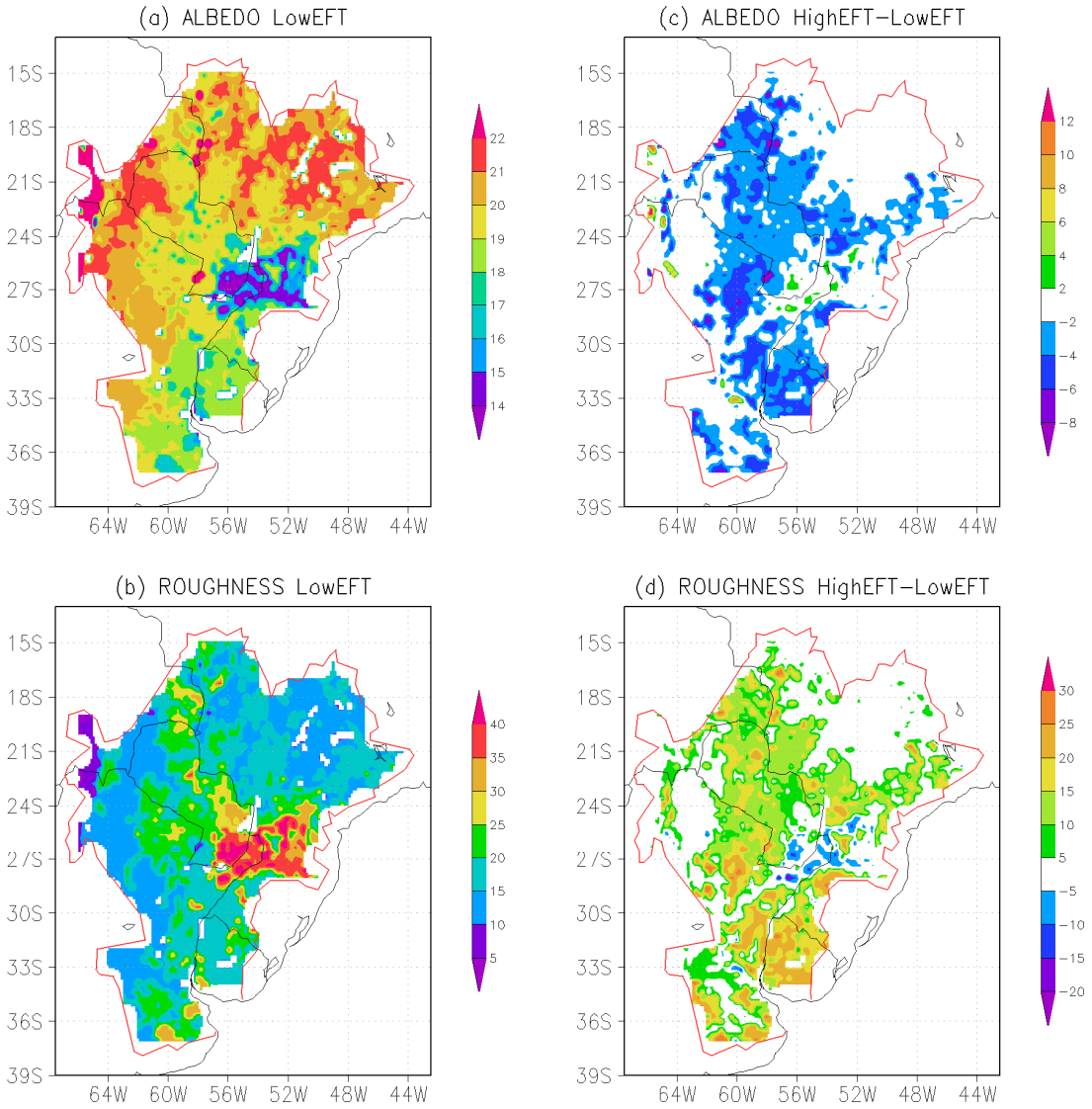

Figure 6.3: (a) Albedo (%) and (b) roughness length (cm) fields corresponding to year 1988 EFT condition (LowEFT), and their differences from year 1998 EFT (HighEFT) for (c) albedo and (d) roughness length.

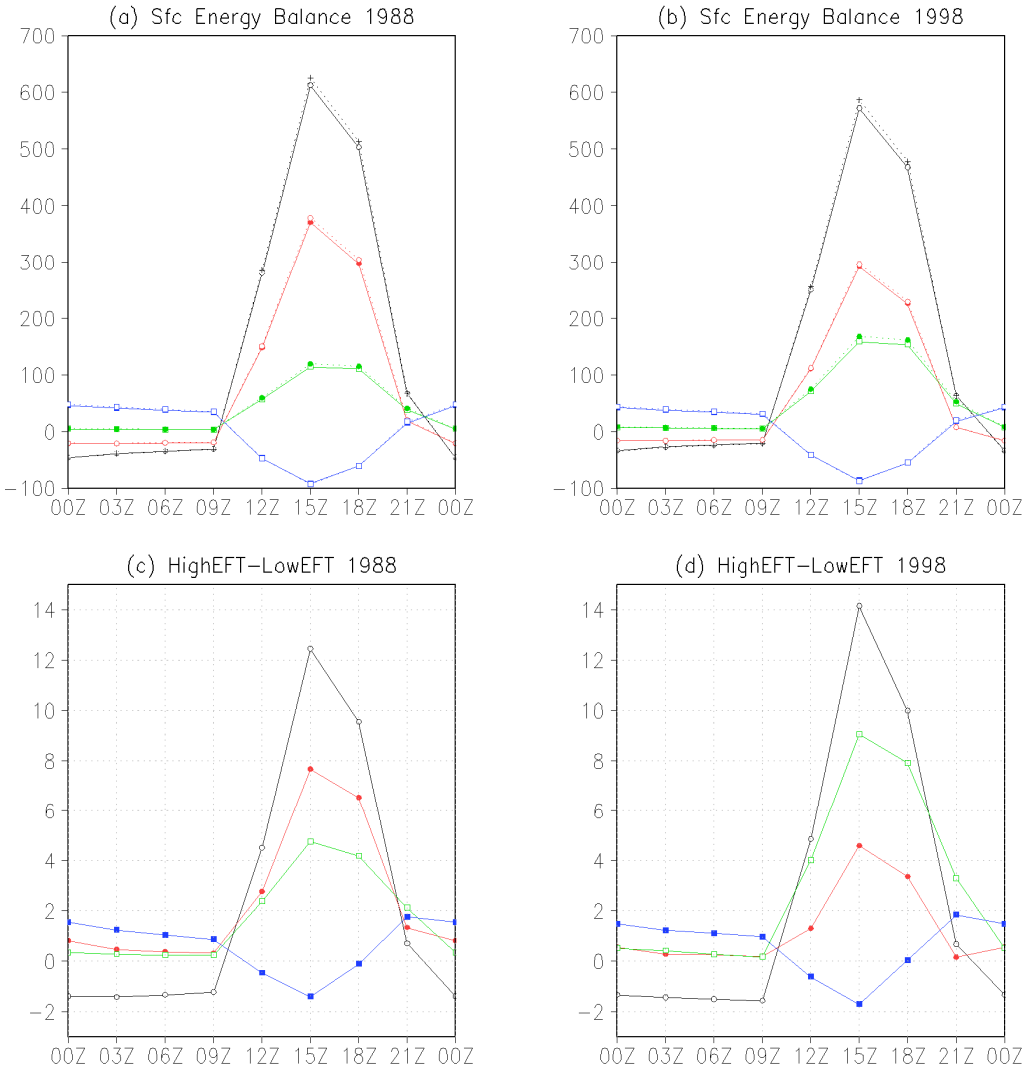

Figure 6.4: Three-month (SON 1988 and 1998) mean diurnal cycle of surface fluxes (W m^{-2}) averaged over La Plata Basin. Solid and dotted lines denote LowEFT and HighEFT, respectively, for (a) year 1988 and (b) year 1998. (c) and (d) show the differences HighEFT – LowEFT. Black: Net radiation; Red: Turbulent sensible heat flux; Green: Turbulent latent heat flux; Blue: Conductive ground heat flux.

However, Figs. 6.4c,d also illustrate that the EFT changes have different effects on partitioning of net radiation into sensible and latent heat fluxes. For 1988, the major impact of using higher EFT is to increase sensible heat fluxes, but for 1998 the main effect of using higher EFT is to increase latent heat fluxes. This indicates that the impact of EFT increase over the LPB is working toward increasing sensible heat fluxes in a dry year, and latent heat fluxes in a wet year.

6.3.2 Changes in near-surface variables

The horizontal distributions of sensible and latent heat fluxes in the LPB play important roles in determining near-surface temperature and humidity. Figure 6.5 shows the three-month averaged 2-m temperature (°C) fields for 1988 and 1998 using LowEFT, and their differences from using HighEFT. The spatial gradient of near-surface temperature is similar between the two years and the main difference occurs over the northern LPB, where year 1998 shows colder spring temperature than 1988 (Figs. 6.5a,b). Figures 6.5c,d show that in general EFT changes over the LPB increase near-surface temperature for both 1988 and 1998. This is directly related with the increased sensible heat fluxes by the reduced surface albedo as shown in Figs. 6.4c,d. The largest temperature increase is mainly located around Paraguay and Uruguay reaching +0.6 to +0.8°C. There are weak cooling regions near the northwestern boundary of the LPB and west of Uruguay. The two numbers in the bottom panels denote mean and standard deviation of corresponding fields. The statistics indicate that the net impact of EFT changes on the near-surface temperature over the LPB is positive and the corresponding variability is somewhat larger in a dry year.

Figure 6.6 presents the three-month averaged 2-m water vapor mixing ratio fields (g kg^{-1}) for 1988 and 1998 using LowEFT, and their differences from using HighEFT. It can be seen that year 1998 has larger 2-m humidity over Paraguay (Figs. 6.6a,b). The maximum increase region lies in the western LPB for both 1988 and 1998. The maximum decrease region is in the northeastern LPB for 1988, but is in the southeastern LPB for 1998 (Figs. 6.6c,d). In general, the net impact of EFT changes on the near-surface humidity is positive and the corresponding variability is bigger in a wet year.

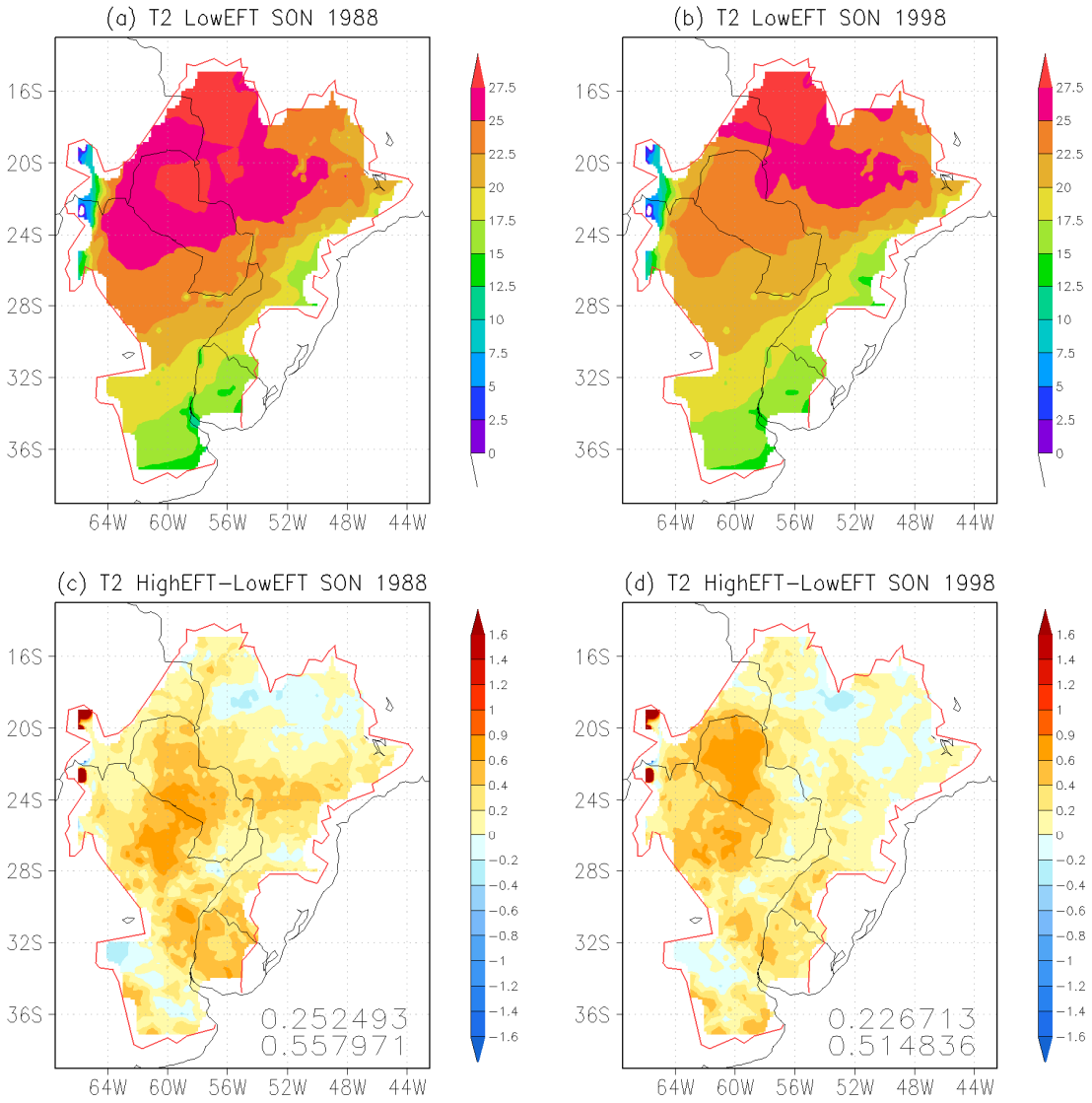

Figure 6.5: Three-month averaged 2-m temperature (°C) fields for (a) 1988 and (b) 1998 using LowEFT, and their differences from using HighEFT for (c) 1988 and (d) 1998. The two numbers in the bottom panels are bias (upper) and standard deviation (lower).

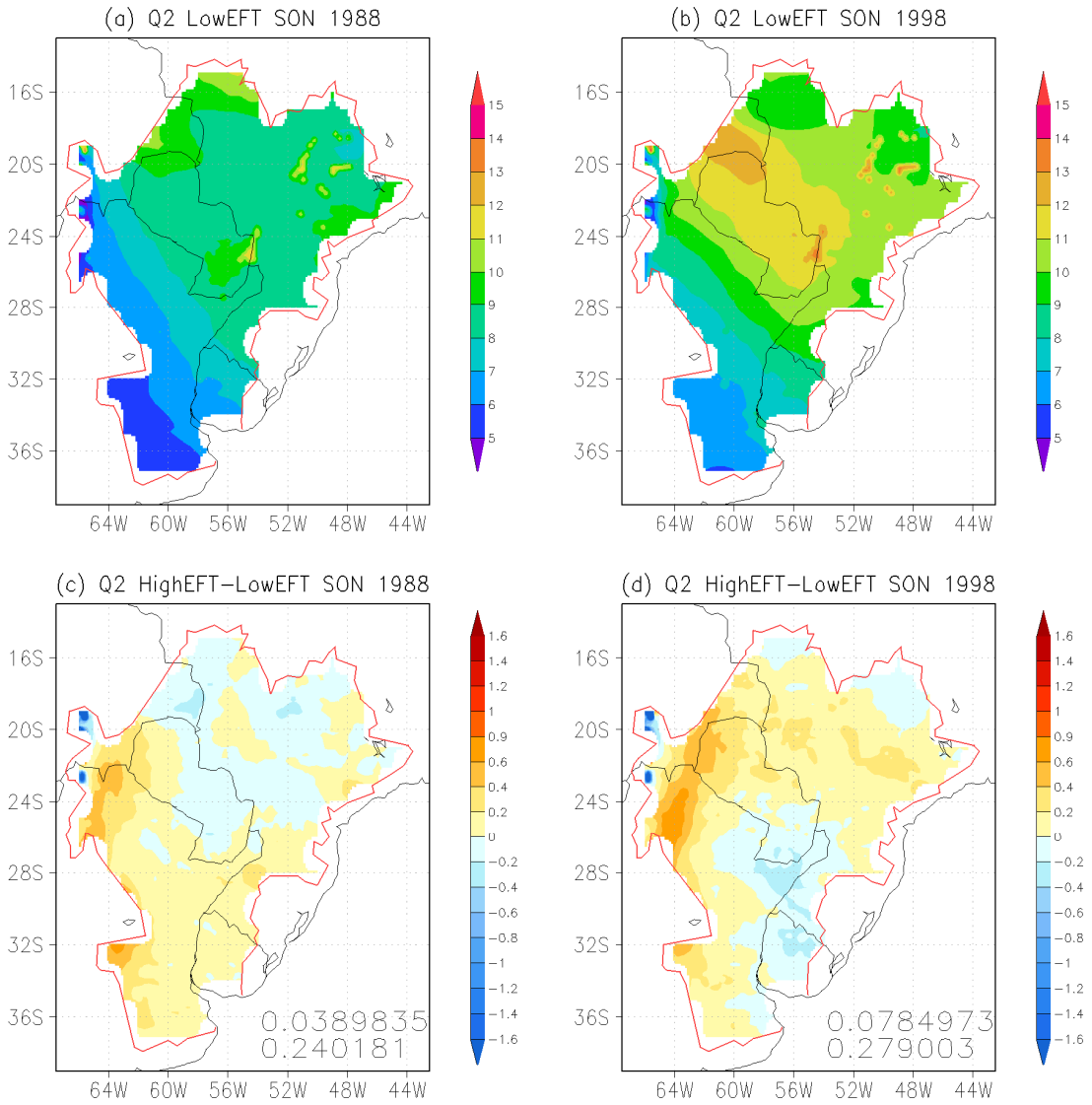

Figure 6.6: Same as Fig. 6.5 but for 2-m water vapor mixing ratio (g kg^{-1}).

Figure 6.7 shows the three-month averaged 10-m wind fields for 1988 and 1998 using LowEFT and, their differences from using HighEFT. Both years of 1988 and 1998 have larger wind speed in the eastern LPB and easterly component winds are dominant (Figs. 6.7a,b). For the year 1988, EFT changes produce overall decreases in the 10-m wind speed (Fig. 6.7c). Such decreases are also seen for the year 1998, but the maximum values appear at different locations (Figs. 6.7c,d). In response to the EFT

changes, northwesterly wind anomalies over Paraguay and westerly wind anomalies over the southern Brazil are produced for the dry year (Fig. 6.7c), but northerly wind anomalies over Paraguay are formed for the wet year (Fig. 6.7d). The net impact of EFT changes on the near-surface wind is negative and the corresponding variability is bigger in a dry year.

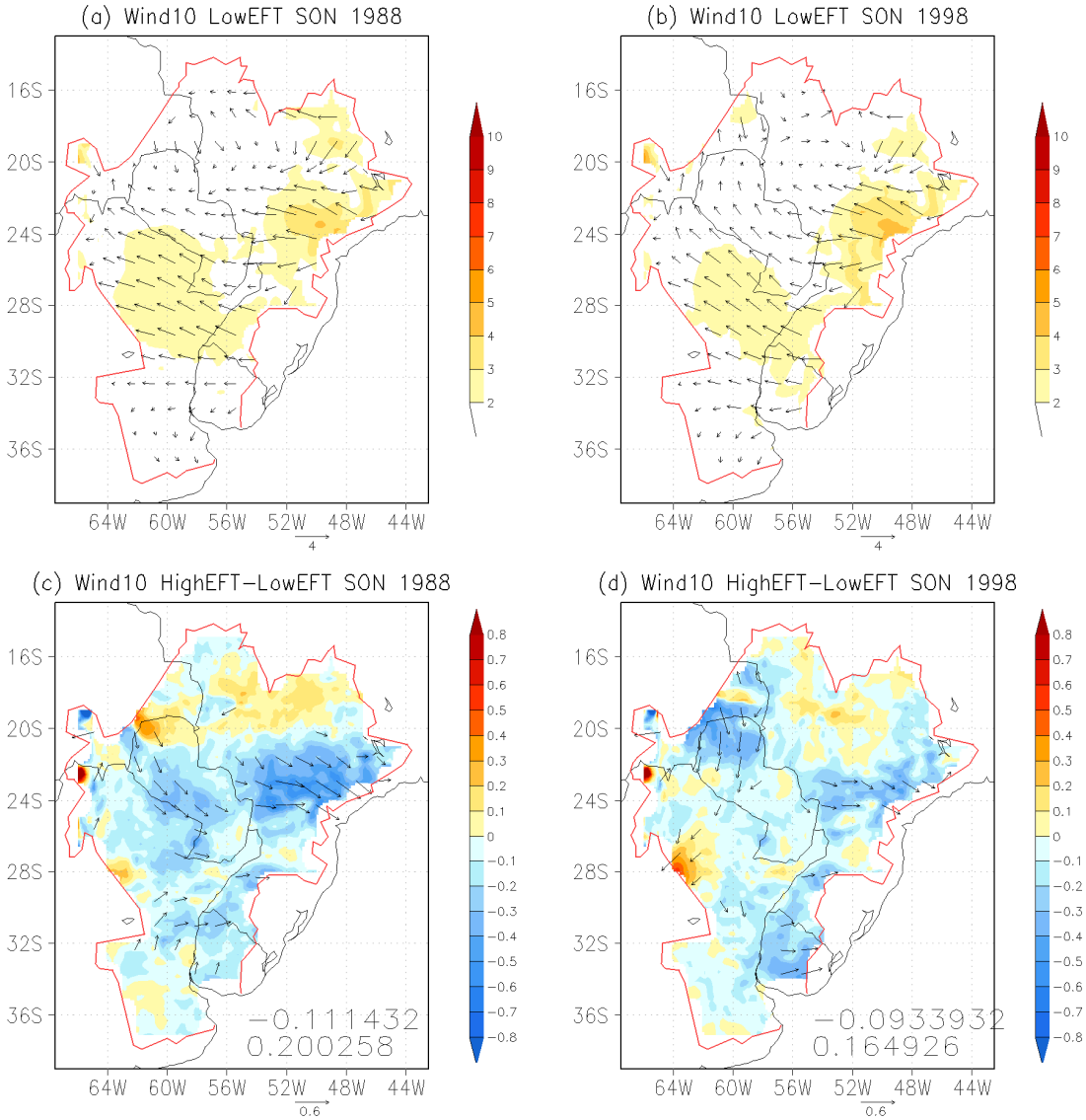

Figure 6.7: Same as Fig. 6.5 but for 10-m wind vector and wind speed (m s^{-1}).

6.3.3 Changes in local thermodynamic forcing

The changes in the surface fluxes and surface energy balance are expected to influence atmospheric instabilities in the vertical. The convective available potential energy (CAPE) and convective inhibition (CIN) are useful tools for analyzing local thermodynamic processes that contribute to the development of precipitation. The CAPE (CIN) is the amount of positively (negatively) buoyant energy in the vertical sounding of temperature, and both are defined as positive signs in this chapter. The CAPE (CIN) can be understood as a thermodynamic forcing facilitating (inhibiting) local convection and precipitation (Bluestein 1993; Barlow et al. 1998). To simplify the analysis, the maximum values from the vertical profiles of CAPE and CIN at horizontal grid points were used and named as MCAPE and MCIN, respectively.

Figure 6.8 shows the three-month averaged MCAPE over the LPB for 1988 and 1998 using LowEFT, and their differences from using HighEFT. The two years 1988 and 1998 have comparatively large MCAPE over Paraguay for the given same LowEFT condition (Figs. 6.8a,b). Given the EFT changes, year 1988 shows small magnitude of MCAPE changes and the signal is weak (Fig. 6.8c). Compared with year 1988, EFT changes in the LPB give rise to more striking modifications in MCAPE field for year 1998 (Fig. 6.8d). For year 1998, the largest increase in MCAPE occurs over the northern Paraguay, and the biggest decrease in the southern LPB, especially between Paraguay and Uruguay (Fig. 6.8d). The MCAPE difference fields (Figs. 6.8c,d) due to EFT changes are associated with the 2-m water vapor mixing ratio fields in Fig. 6.6. Regions of the maximum increase (decrease) in MCAPE tend to correspond to regions of the maximum increase (decrease) in 2-m water vapor mixing ratio especially for 1998. All these indicate that the net impact of EFT increase on atmospheric insta-

bilities is positive and the corresponding variability is much larger in a wet year.

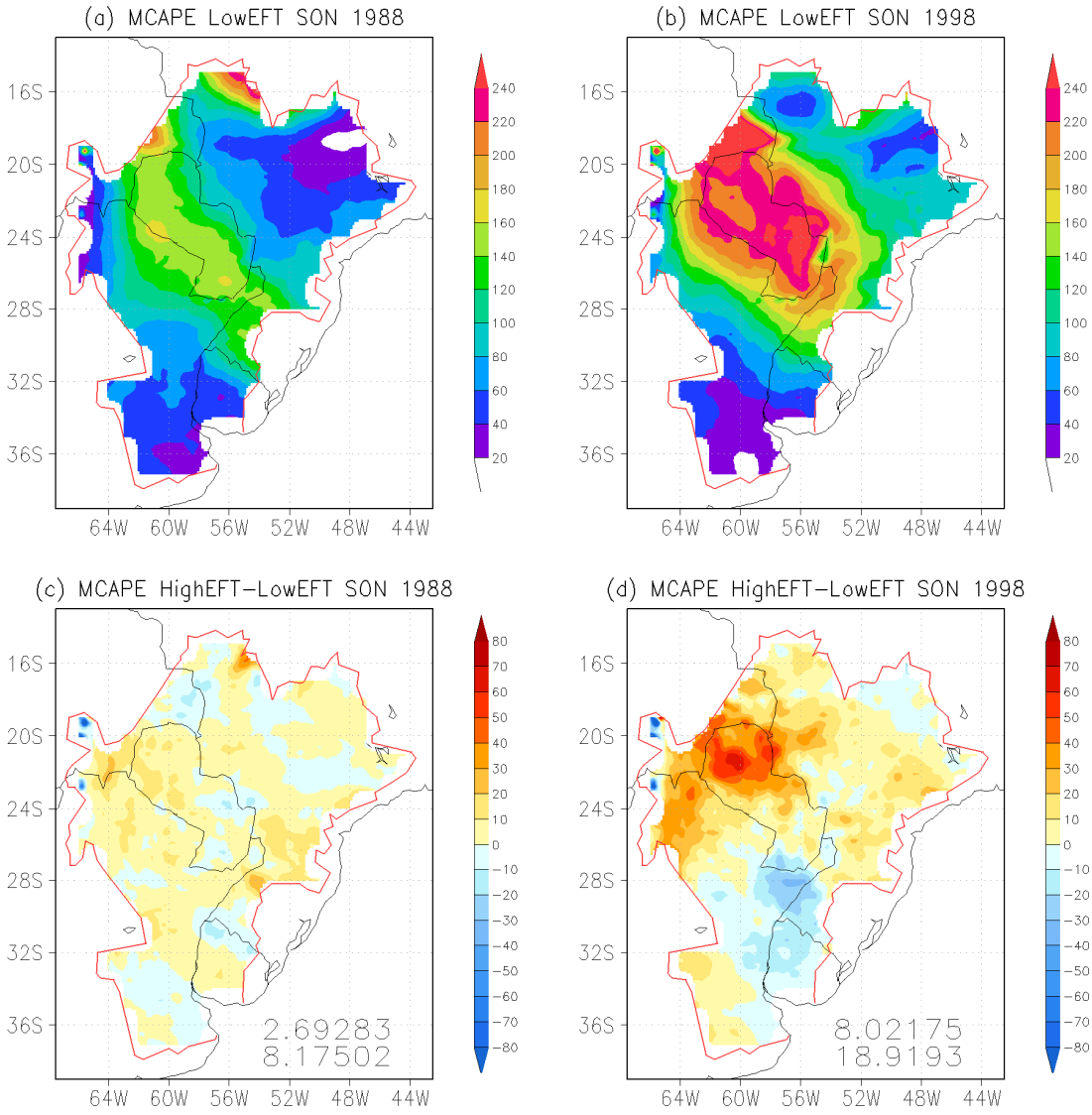

Figure 6.8: Same as Fig. 6.5 but for maximum CAPE (J kg^{-1}).

Figure 6.9 shows the three-month averaged MCIN over the LPB for 1988 and 1998 using LowEFT, and their differences from using HighEFT. The two years 1988 and 1998 have comparatively large MCIN around Paraguay for the given same LowEFT condition, but year 1998 has larger values of MCIN around the northern Paraguay (Figs. 6.9a,b). Compared with MCAPE (Figs. 6.8c,d), the difference field (Figs. 6.9c,d) of MCIN has less organized structure, and shows some reverse patterns for the two years, for example, over the northwestern and the southeastern parts of the basin. It should be noted from Figs. 6.8c,d and 6.9c,d that the northwestern LPB has a favorable condition for local convective precipitation due to the increased MCAPE and the decreased MCIN. The net impact of higher EFTs on the MCIN is positive for both a dry year and a wet year, and the variability of MCIN corresponding to the EFT change is almost the same between a dry year and a wet year (Figs. 6.9c,d). The effect of EFT changes on the MCIN field does not show much dependency on the two contrasting years (Figs. 6.9c,d), and this is contrasted with MCAPE (Figs. 6.8c,d) which shows highly different features between a dry year and a wet year. Therefore, it is expected that the MCAPE field would play a practical role in determining the local convective precipitation.

6.3.4 Changes in large-scale horizontal moisture flows

We cannot say that the change in precipitation over the LPB is the only consequence of changes in the MCAPE and MCIN fields. The change in the surface fluxes and near-surface atmospheric variables can affect not only local instabilities, but also regional moisture flows by modifying surrounding atmospheric circulations.

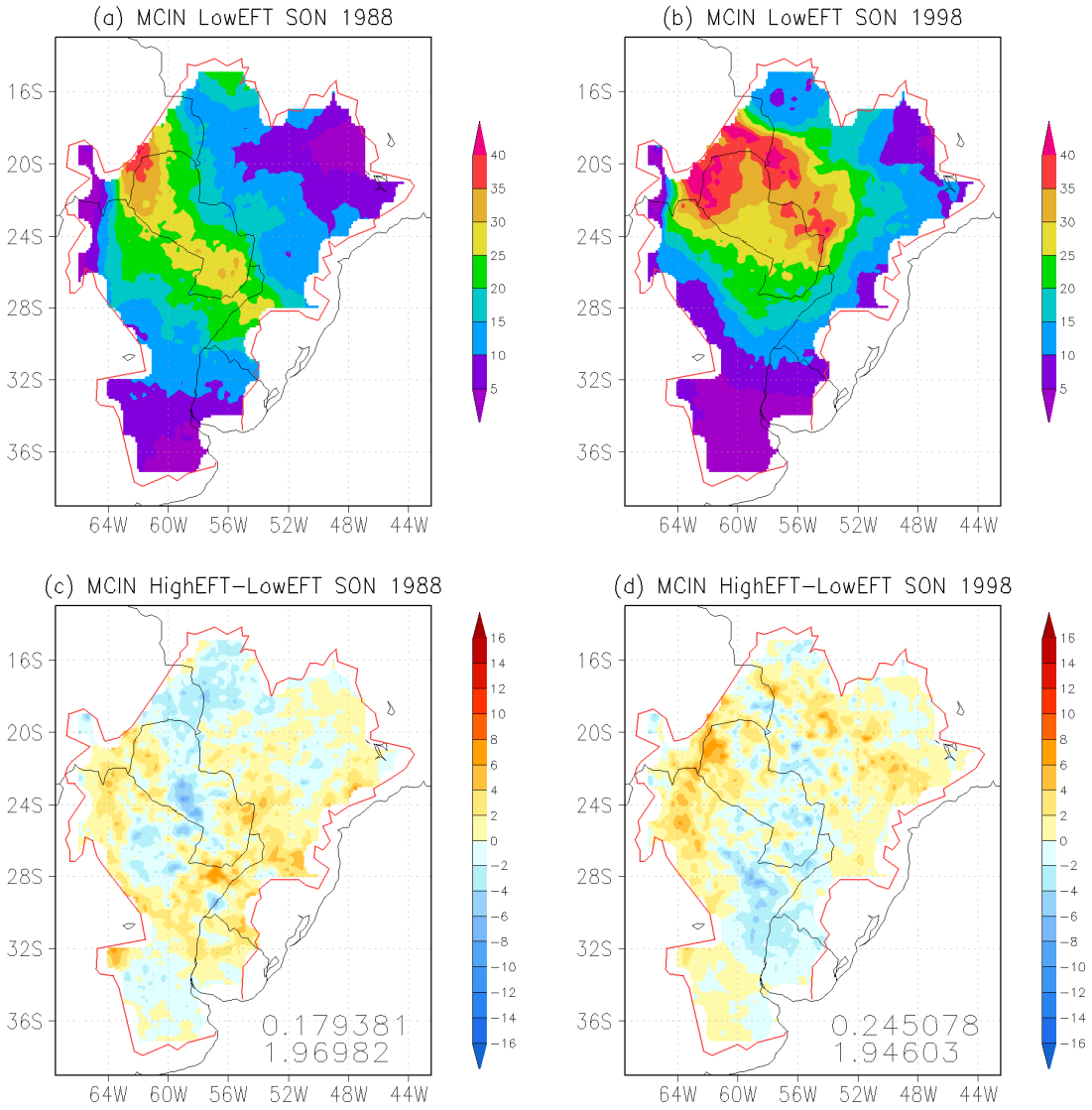

Figure 6.9: Same as Fig. 6.5 but for maximum CIN (J kg^{-1}).

In fact, a major reason for variability in precipitation over LPB is moisture transported from Amazon basin by Low-Level Jets (LLJs). Figure 6.10 presents the horizontal moisture flux, vertically integrated from 1000 hPa to 300 hPa, for 1988 and 1998 using LowEFT, and their differences from using HighEFT. The convergence/divergence of the moisture fluxes is shaded using the color scale at the right of the figure. The changes in moisture flux and its convergence/divergence over LPB are related with the increased near-surface wind due to the reduction in roughness

length, as shown in Figs. 6.3d and 6.7c,d. Figures 6.10a,b illustrate the well-known moisture supply to the LPB by the northerly LLJ during the warm season. A region of southward low-level moisture flux into the LPB occurs through the relatively low-altitude lands formed between the Andes Mountain ranges and the Brazilian Highlands. The wet year 1998 has larger moisture transport from the north and the region of largest moisture flux convergence is seen around Paraguay (Fig. 6.10b).

Using higher EFTs over the LPB produces changes in moisture flows and the associated convergence/divergence fields. For year 1998, the impact of EFT changes on moisture flows are more organized and produce an anticyclonic anomaly near central Paraguay (Fig. 6.10d). The net impact of EFT changes on the large-scale moisture transport is almost neutral and the corresponding variability is slightly larger in a wet year. On the other hand, Figs. 6.10e,f show moisture fluxes and their convergence vertically integrated from 1000 hPa to 850 hPa. Although the net impact of EFT changes on the moisture flux convergence and the corresponding variability is similar to the one vertically integrated from 1000 hPa to 300 hPa, the intensity of moisture flux convergence is strong since atmospheric humidity is concentrated at lower altitudes. Figures 6.10e,f show that overall effects of EFT changes on the lower tropospheric moisture convergence are increases (decreases) of precipitation in the northwestern (southern) LPB.

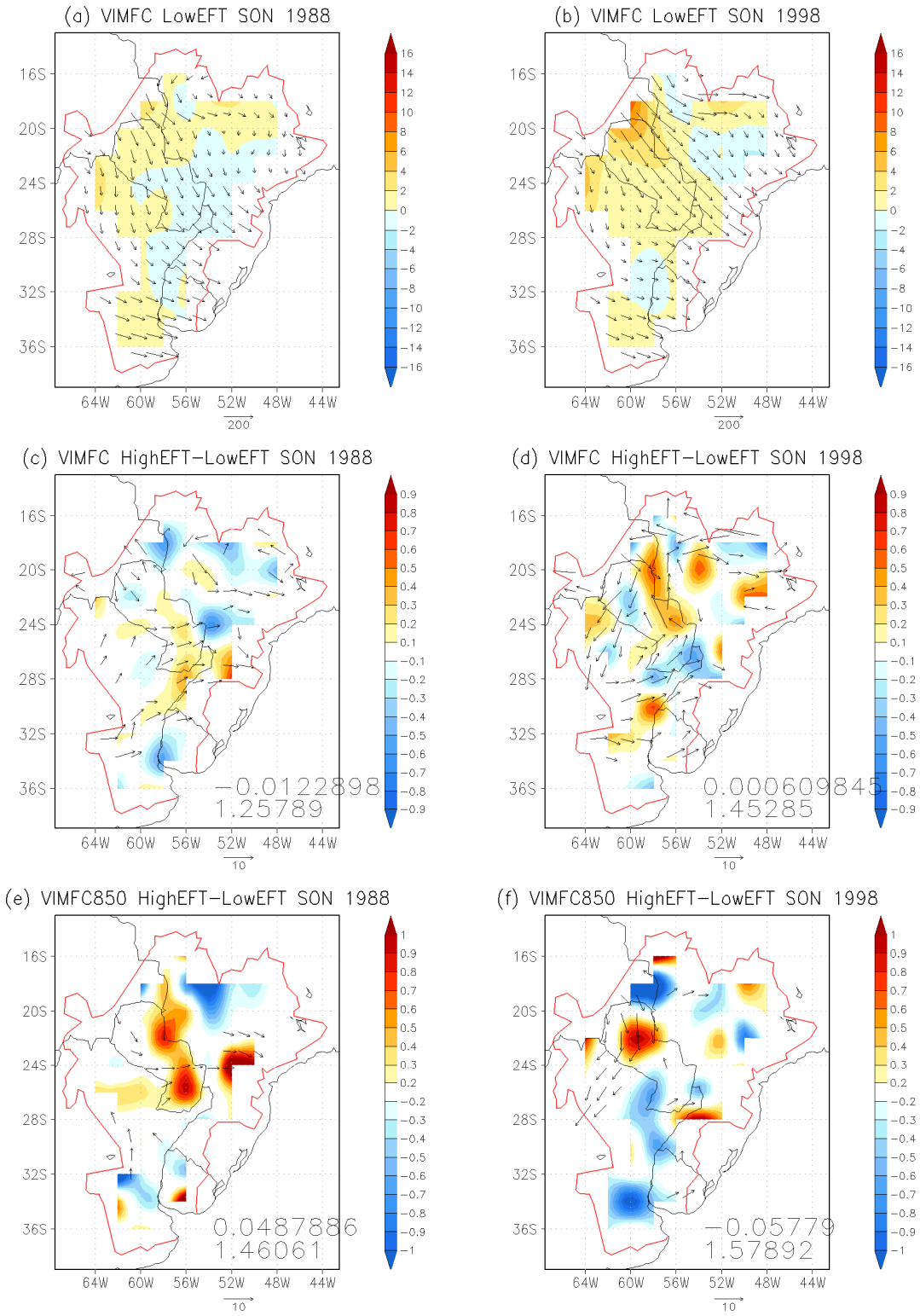

Figure 6.10: (a)-(d) Same as Fig. 6.5 but for vertically integrated moisture fluxes (kg (m s)$^{-1}$) and their convergence (mm day^{-1}). (e)-(f) Same as (c)-(d) but for moisture fluxes integrated for lower troposphere from 1000 hPa to 850 hPa.

6.3.5 Changes in precipitation

As a reasonable approximation, precipitation over the LPB can be understood as a combined product of local thermodynamic effects and larger-scale dynamical effects discussed in section 6.3.3 and 6.3.4, respectively. Figure 6.11 presents the three-month average precipitation field for 1988 and 1998 using LowEFT, and their differences from using HighEFT. Precipitation difference between the two years under the LowEFT condition is striking, and precipitation increases greatly over Paraguay in the wet year (Figs. 6.11a,b). Such an increase of precipitation over Paraguay is consistent with the large MCAPE (Fig. 6.8b) and the large moisture flux convergence (Fig. 6.10b) over Paraguay in the wet year.

Figures 6.11c,d indicate that the net impact of high EFTs on the total precipitation is positive for both years, and the corresponding variability is larger in a wet year. For a dry (wet) year, the net increase in precipitation is weak (strong). Figure 6.11d shows that due to the high EFTs, precipitation is in general increased over northern LPB above latitude 26˚ S, but is decreased in southern Paraguay. Figures 6.10c,d and 6.11c,d show an overall agreement between total precipitation and vertically integrated moisture flux convergence. The regions of precipitation increase (decrease) are collocated with vertically integrated moisture flux convergence (divergence) for both dry and wet years.

Figures 6.11e,f are same as Figs. 6.11c,d but for the convective component of total precipitation. It can be seen that the net effect of EFT changes on the convective precipitation is positive for both dry and wet years, and the corresponding variability is larger in a wet year. The horizontal distribution of the convective and total precipitation looks somewhat similar to each other except for the magnitude. It needs to be

noted that the northern LPB has dominant increases in the convective precipitation for the wet year (Fig. 6.11f), and this seems to be related with the MCAPE field in Fig. 6.8d.

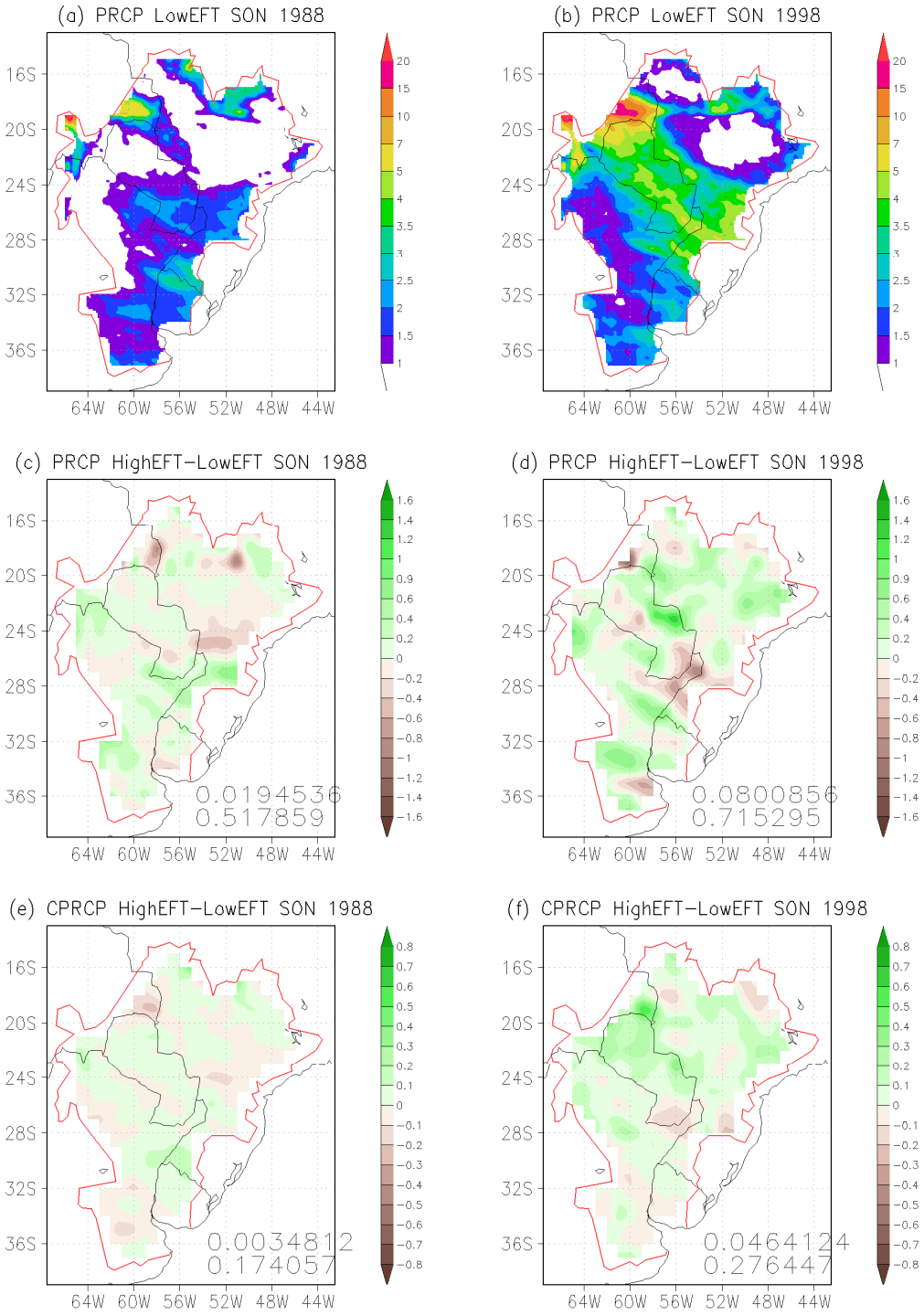

Figure 6.11: (a)-(d) Same as Fig. 6.5 but for total precipitation (mm day^{-1}). (e)-(f) Same as (c)-(d) but for convective component of total precipitation.

6.3.6 Comparison with observed changes in precipitation and 2-m temperature

Figure 6.12 shows the observed changes in precipitation and 2-m temperature from 1988 to 1998. Figure 6.12a shows that precipitation increased over the northern LPB, while precipitation was reduced in the southern LPB. The region of the maximum increase (decrease) in precipitation is located east of the southern Paraguay (around Uruguay). Figure 6.12b presents that year 1998 had colder near-surface temperature over the northern LPB, while it had slightly warmer near-surface temperature over the northeastern and southwestern LPB. All these changes between 1988 and 1998 should be attributed not only to land surface changes but also to diverse forcings driven by atmosphere, ocean, aerosol, and teleconnection etc. Nevertheless, it is clear that the observed changes in precipitation from 1988 to 1998 are similar to the simulated changes. For example, the signals of observed changes in precipitation (Fig. 6.12a) are found in the simulated MCAPE (Fig. 6.8d), vertically integrated moisture flux convergence (Figs. 6.10e,f) and convective precipitation fields (Fig. 6.11f). This indicates that the effect of EFT changes contributed to the observed precipitation fields. EFT changes in a wet year may induce a large increase of CAPE especially in the northern LPB, and facilitate the development of Mesoscale Convective Systems that are responsible for much of the region's precipitation.

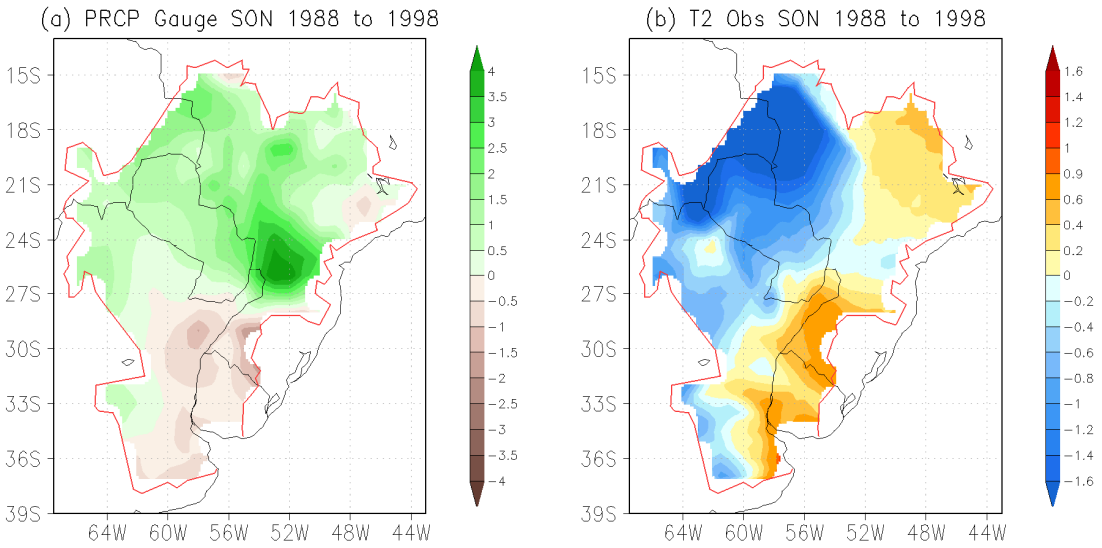

Figure 6.12: Observed changes in (a) precipitation (mm day^{-1}) and (b) 2-m air temperature (°C) from 1988 and 1998.

The observed changes in 2-m temperature (Fig. 6.12b) from 1988 to 1998 are similar to the simulated fields (Figs. 6.5c,d) over the southern LPB, especially around Uruguay. This is explained by the fact that the largest changes in the surface albedo and roughness length occurred mainly in the southern LPB especially around Uruguay (see Figs. 6.3c,d), and thus the effect of EFT changes are concentrated in those regions. However, the other regions show the opposite features between the simulated and observed 2-m temperature. This implies that those regions are strongly affected by other factors than land cover changes.

6.4 Summary and concluding remarks

The climate of the La Plata Basin in South America is subject to land-cover and land-use changes with important consequences for the environment. Two contrasting years (a dry year and a wet year) are chosen to investigate the interannual variability of land-atmosphere interactions and their effect on regional climate. According to EFT maps and their properties over the LPB, the surface albedo was lower for 1998 than for 1988. The surface roughness length was higher in 1998 than in 1988. In this chapter, the Weather Research and Forecast (WRF) modeling system and Ecosystem Functional Type data were used to explore the role of varying land cover conditions from 1988 to 1998 in the regional climate over the LPB. The EFT changes between 1988 and 1998 are applied to a dry year (1988) and a wet year (1998), respectively, to examine the dependence of the same land surface forcing on the two different years.

When the 1988 EFT data were replaced with the 1998 EFT data (higher net primary productivity), the simulated spatial patterns of the surface heat fluxes, near-surface atmospheric variables, and local thermodynamic and larger-scale dynamic forcings, and surface precipitaiton were altered. Table 6.1 summarizes the impact of EFT changes on all those prognostic variables. It is found that the range of surface and atmospheric responses to the given EFT changes is bigger in a dry year for 2-m temperature and 10-m wind, while is bigger in a wet year for 2-m water mixing ratio, convective available potential energy, vertically-integrated moisture fluxes and precipitation. This indicates that the impact of land-cover land-use changes on the climate of the LPB is dependent not only on the wetness of the year, but also on meteorological or climate variables.

Table 6.1: The impact of EFT changes (HighEFT – LowEFT) on the following variables. The mean values are shown in the table with standard deviation denoted by ( ).

(Basin Averaged)	Dry year (IC and LBC of 1988)	Wet year (IC and LBC of 1998)
2-m Temperature (℃)	0.25 (0.56)	0.23 (0.51)
2-m water vapor mixing ratio (g kg^{-1})	0.04 (0.24)	0.08 (0.28)
10-m wind speed (m s^{-1})	-0.11 (0.20)	-0.09 (0.16)
Max. CAPE (J kg^{-1})	2.69 (8.18)	8.02 (18.92)
Max. CIN (J kg^{-1})	0.18 (1.97)	0.25 (1.95)
1000-300hPa vertically integrated MFC (mm day^{-1})	-0.012 (1.26)	0.001 (1.45)
1000-850 vertically integrated MFC	0.05 (1.46)	-0.06 (1.58)
Precipitation (mm day^{-1})	0.02 (0.52)	0.08 (0.72)
Convective precipitation (mm day^{-1})	0.003 (0.174)	0.046 (0.276)

According to comparisons with observations, the simulated precipitation difference resulting from EFT changes holds the overall pattern of observed changes. The simulated 2-m temperature difference due to EFT changes also reflects observed changes over the southern LPB. In particular, over Uruguay in the southern LPB where the most significant EFT change occurred, higher EFTs led to an increase in the 2-m temperature especially for a dry year (Fig. 6.5c) and an overall decrease in the spring total precipitation especially for a wet year (Figs. 6.11d,f). This is in agreement with previous modeling studies (e.g., Narisma and Pitman 2003, Marshall et al. 2004, Pongratz et al. 2006, McAlpine et al. 2007) that indicate decreasing regional precipitation and increasing temperature due to historical land cover changes.

Therefore, ecosystem functional type changes can provide important lower boundary information for model simulations of regional climate, particularly over the LPB, and it is highly desirable that they are monitored on a regular basis. The relations between EFTs and climate deserve further exploration both for climate and ecology studies,

and the results could be used for a guided land-use planning and more efficient land-surface management policy.

Chapter 7: Summary

7.1 Regional climate response to land-cover/land-use change over the La Plata Basin

During the last few decades, deforestation and replacement of natural pastures by agriculture have become a common practice in the La Plata Basin in South America. The changes in vegetation may produce changes in physical properties like the surface albedo, the surface roughness length, evapotranspiration, infiltration, and water storage eventually affecting the development of precipitation and ultimately the hydroclimate of the basin.

To study the role of changing land cover conditions in the La Plata Basin, the Weather Research and Forecast (WRF) modeling system was employed. Ensembles of seasonal simulations were prepared for a control case and two extreme land cover scenarios: the first one assumes an expansion of the agricultural activities and the second one assumes a "natural" vegetation cover where no croplands are present. These highly idealized scenarios have the purpose of helping understand the potential changes to physical mechanisms before attempting simulations with more realistic conditions. In order to examine the changes to the mechanisms that induce precipitation, the land-atmosphere interactions were examined, as well as their role in modifying the boundary layer, the convective instability, the low level moisture fluxes, and lastly, precipitation.

An extreme anthropogenic land-cover change -simulating an extensive agricultural

practice- implies that the northern part of the basin, where croplands replace forests and savanna, would experience an overall increase in albedo and reduced surface friction. The two changes lead to a reduction of sensible heat flux and surface temperature, and a somewhat higher evapotranspiration due to decreased stomatal resistance and stronger near-surface winds. The effect on sensible heat flux seems to dominate and leads to a reduction in convective instability. The stronger low level winds due to reduced friction also imply a larger amount of moisture advected out of the basin, and thus resulting in reduced moisture flux convergence (MFC) within the basin. The two effects, increased stability and reduced MFC, result in a reduction of precipitation. On the other hand, the southern part of the basin exhibits the opposite behavior, as crops would replace grasslands, resulting in reduced albedo, a slight increase of surface temperature and increased precipitation. Notably, the results are not strictly local, as advective processes tend to modify the circulation and precipitation patterns downstream over the South Atlantic Ocean, and even a potential linkage between the basin and the tropical regions is implied.

7.2 Usefulness of newly developed Ecosystem Functional Types (EFTs) in a mesoscale regional climate model

Accurate specification of the land surface state is important in numerical weather and climate prediction and simulation studies. For that purpose, recent efforts have focused upon using satellite-based land cover data in the numerical models to substitute for the existing ground-based land cover data which are estimated by a multi-year climatology. Those efforts were realized in state-of-the-art numerical models like the fifth-generation Pennsylvania State University-National Center for Atmospheric Re-

search (PSU-NCAR) Mesoscale Model (MM5) and the Weather and Research Forecasting (WRF) model.

However, both ground-based and satellite-derived datasets are using a land-cover classification dictated by “structural” attributes of vegetation, and are insensitive to rapid and complex environmental changes. In this study, a new concept of land-surface state representation which is based on “functional” attributes of ecosystems, was introduced and the new land cover classification (Ecosystem Functional Type) dataset was successfully incorporated in the WRF Model.

In order to explore the usefulness of the EFT data in simulations of surface and atmospheric variables, numerical simulations of the WRF Model, using both the U.S. Geological Survey (USGS) and the EFT data, are conducted for the austral spring of 1998 and are compared with observations. Results show that use of the EFT data improves the climate simulation of 2-m temperature and precipitation, implying the need for this type of information to be included in numerical climate models. In particular, with the use of EFT data in replacement of USGS data, the southern LPB had an increase in large-scale MFC, while the northern LPB had increases in both CAPE and large-scale MFC. These two effects produced overall enhancement of precipitation over the LPB and led to a substantial reduction in precipitation bias, i.e., partially corrected the lack of model precipitation.

7.3 Impact of variable EFTs on the climate of the La Plata Basin

The Ecosystem Functional Types (EFTs) is a newly devised land-cover classification

to characterize the spatial and inter-annual variability of surface vegetation dynamics. It is composed of 64 functional attributes of vegetation describing its energy and gas exchange with the atmosphere, and provides more detailed information in space and time compared with the existing satellite-derived land-cover classification.

During the last few decades, the La Plata Basin (LPB) in South America has shown a large spatial and interannual variability of the EFTs. Those variations mean that changes in the surface physical parameters, such as albedo and roughness length, have occurred over the basin due to natural and anthropogenic activities, and might have contributed to the regional climate variability and change.

In this study, the effect of EFT changes on the climate of the LPB is investigated using the Weather and Research Forecasting (WRF) model configured on a 30/10-km two-way interactive nested grid. Four simulations are carried out consisting of September to November experiments for two contrasting years of 1988 and 1998. The influence of an EFT change applied in 1988 and in 1998 on the surface heat fluxes, 2-m temperature and humidity, 10-m winds, convective instabilities and large-scale moisture fluxes and precipitation are explored for 1988 (a dry year) and 1998 (a wet year).

Results show that the response of surface and atmospheric climate to the given same EFT changes is larger in a dry year for 2-m temperature and 10-m wind, while is larger in a wet year for 2-m water vapor mixing ratio, convective available potential energy, vertically-integrated moisture fluxes and surface precipitation. This indicates that the impact of land-cover and land-use changes on the climate of the LPB is dependent not only on the wetness of the year, but also on the meteorological or climate

variables.

Comparisons with observations show that the simulated precipitation difference induced by EFT changes produces the overall pattern of observed precipitation changes over the LPB. The results suggest that LULC changes over the LPB can partly explain and contributed the increasing trend of observed precipitation. In the case of the 2-m temperature, the simulated difference due to EFT changes is similar to the observed change in the eastern part and the southern part of the basin (especially in Uruguay), where the strongest EFT changes occurred.

Appendix A. Use of a Mixed-Physics Ensemble for Regional Climate Simulations over South America

A.1 Introduction

In general, ensemble methods are more useful in short-range limited-area and medium-range (or longer-term) global simulations and predictions, compared with a single realization using a single model. A mixed physics ensemble (MPE) is one of the approaches for constructing regional climate model ensembles. The ten simulations shown in Chapter 3 can be utilized as a MPE over South America (see Table 3.1). In this Appendix, I intended (1) to estimate the variability of simulation performance resulted from use of different model physics combinations, and (2) to evaluate the performance of ensemble mean and the characteristics of ensemble spread fields.

A.2 Method

I made two kinds of MPEs using different model parameterization schemes in the WRF limited area model. The first type is an all-physics MPE where different surface layer, boundary layer, cumulus, and microphysics schemes were used (EXP1 to 10 in Table 3.1). The second type is a cumulus-physics MPE which is composed of only four different cumulus parameterizations (EXP3, 4, 7 and 8 in Table 3.1). Interest model variables are precipitation and 2-m temperature, and the MPE simulations were conducted with a single model domain covering South America for the period of September 2002, an austral spring season.

A.3 Results and discussion

Figure A.1b represents the ensemble-mean field of precipitation, while Fig. A.1c exhibits the field of ensemble standard deviation. At each grid-point, the average of the ensembles is calculated, and the standard deviation of the ensemble members around this average. In general, the ensemble mean field shows a good agreement with satellite observation in terms of precipitation location (Figs. A.1a,b). Figure 1b shows that the locations of the main precipitation signal were captured very well by the ensemble mean in the model domain. Those include northwestern region, southeastern LPB, South Atlantic Convergence Zone, east and west seas of Southern South America. However, the intensity of the precipitation was underestimated in most regions, which include the central Brazil and a part of the ITCZ on the east of the South America continent. Such underestimation is a common deficit that most of model simulations have shown in this region until now, as mentioned in Chapter 3. On the other hand, the precipitation intensity was overestimated especially along the Andes mountain range.

The ensemble spread in Fig. A.1c measures the differences between the members in the ensemble simulation. Small spread indicates low simulation uncertainty, and large spread high simulation uncertainty. Figure A.1c shows that simulation uncertainties in LPB region were quite low compared with lower latitude regions, where atmospheric predictability was low. Within LPB, area of large uncertainties was located in southeastern area where the maximum precipitation in LPB occurred. These standard deviations indicate that the precipitation over eastern South Pacific Ocean is simulated quite consistently among the ensemble members (ensemble standard deviations

less than 1 mm day^{-1}), and the precipitation in the ITCZ and northwestern South America, where large gradients are simulated, are somewhat less certain (ensemble standard deviations greater than 3 mm day^{-1}). The bias (the difference of mean daily-precipitation and observed precipitation) indicates that the maximum deficiency of mean daily-precipitation occurs near the south eastern LPB where broadleaf evergreen forest is located.

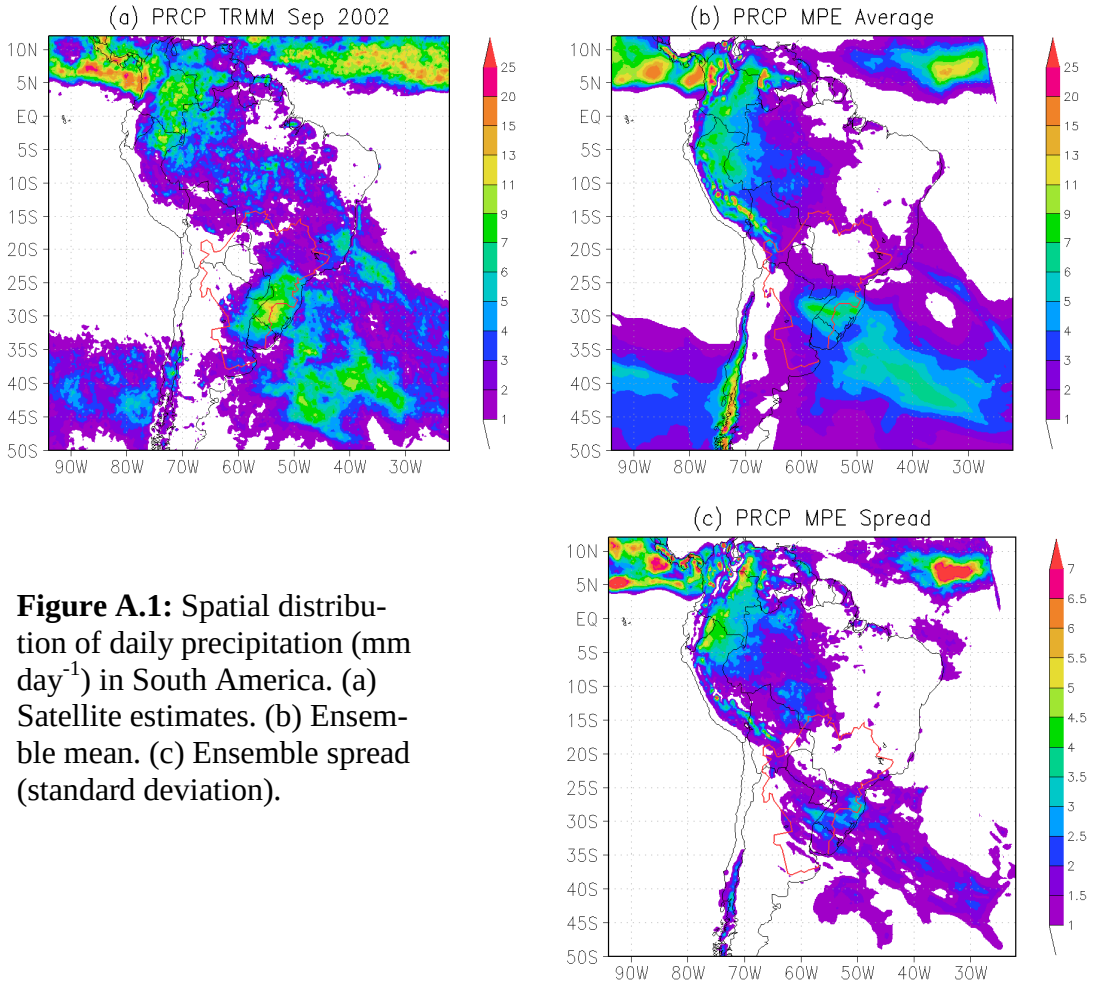

Figure A.1: Spatial distribution of daily precipitation (mm day^{-1}) in South America. (a) Satellite estimates. (b) Ensemble mean. (c) Ensemble spread (standard deviation).

Figure A.2 shows that precipitation simulation performance is very sensitive to the choice of model physics in the WRF. The ensemble spread obtained by using different moist physics schemes had as large magnitude as the spread obtained by using completely different models, i.e., multi-model ensembles (MMEs). This supports the possibility that a mixed-physics ensemble approach could be considered as a proxy for a MME (Arritt et al. 2004). The convective and grid-scale precipitation were similar in terms of accumulated rainfall amounts, and this indicates that importance of both large-scale flow and local forcing are important for precipitation in this region.

Both EXP 1 and 2 exhibit different behaviors from the other eight members in accumulated non-convective precipitation (Fig. A.2b). This implies that WSM3 microphysics should be avoided for numerical simulation of grid-scale precipitation in this region. On the other hand, EXP 2, 5, 6, 7, and 8 can be put together, in accumulated convective precipitation (Fig. A.2c), as the first group, and the other five members as the second group. Because all of the second group members use the BMJ scheme for a cumulus parameterization, this shows the best performance of the BMJ scheme for numerical simulation of convective-scale precipitation in this region.

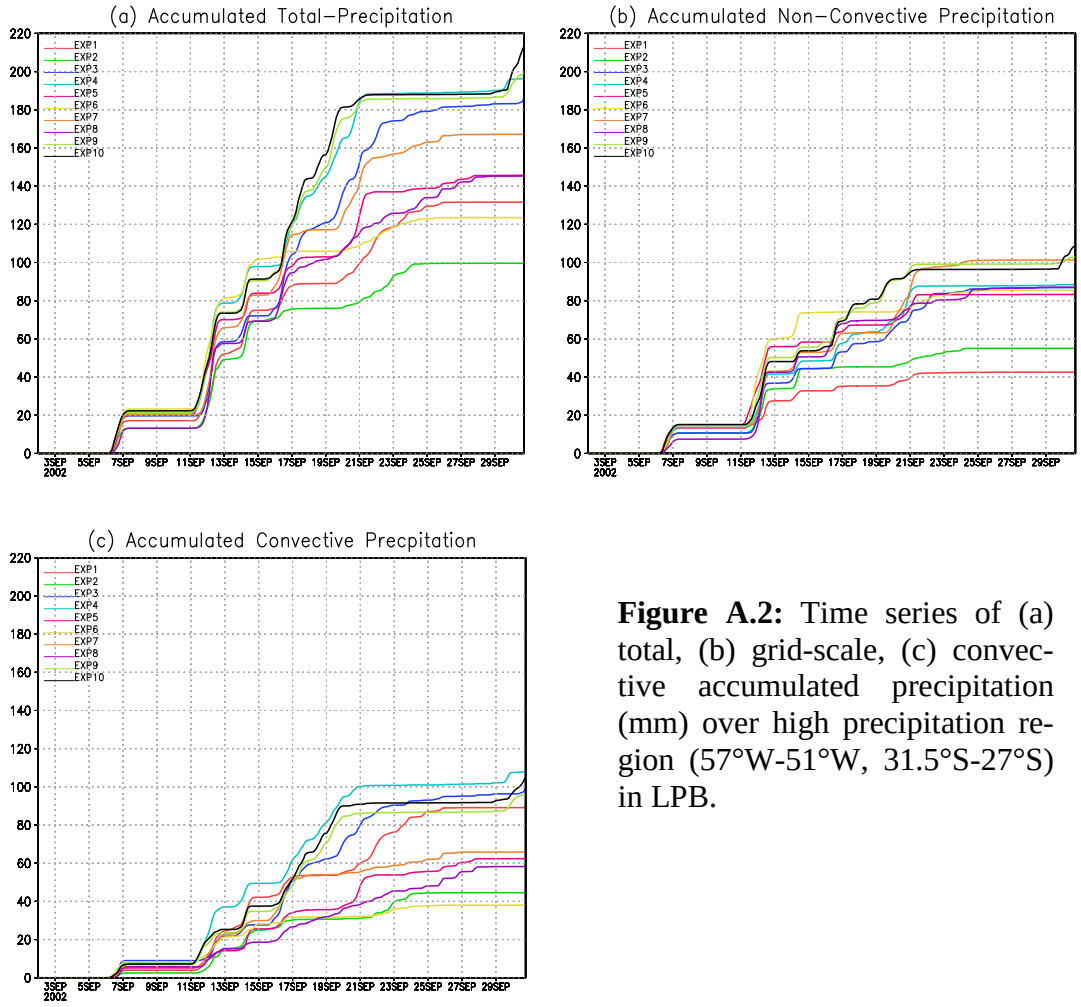

Figure A.2: Time series of (a) total, (b) grid-scale, (c) convective accumulated precipitation (mm) over high precipitation region (57°W-51°W, 31.5°S-27°S) in LPB.

Figure A.3 contains information on the simulated amount of total accumulated precipitation in South America according to the choice of model physics. It is clear that all model simulations produced smaller precipitation than observed. Use of the NOAH LSM (a thermal diffusion scheme) decreased (increased) precipitation amount (EXP3 and 8). The MOJ-MYJ surface and boundary layer scheme increased precipitation amount compared to the MO-YSU scheme (EXP 5 and 10; EXP 6 and 7). The BMJ cumulus scheme was superior to the GD scheme, which was better than the KF scheme (EXP 1 and 2; EXP 4, 7 and 8). The WSM6 microphysics scheme increased precipitation amount compared to the WSM3, WSM5 and Ferrier schemes (EXP 1

and 5; EXP 4, 9 and 10). Results show very high sensitivity to the choice of cumulus scheme (EXP 4, 7 and 8) and small sensitivity to microphysics. Also, Figure A.3 shows that the cumulus-physics ensemble outperformed the all-physics ensemble by increasing accumulated precipitation in LPB with model integration time. This suggests that the mixed-physics ensemble using different cumulus convection schemes is a more efficient method in this region.

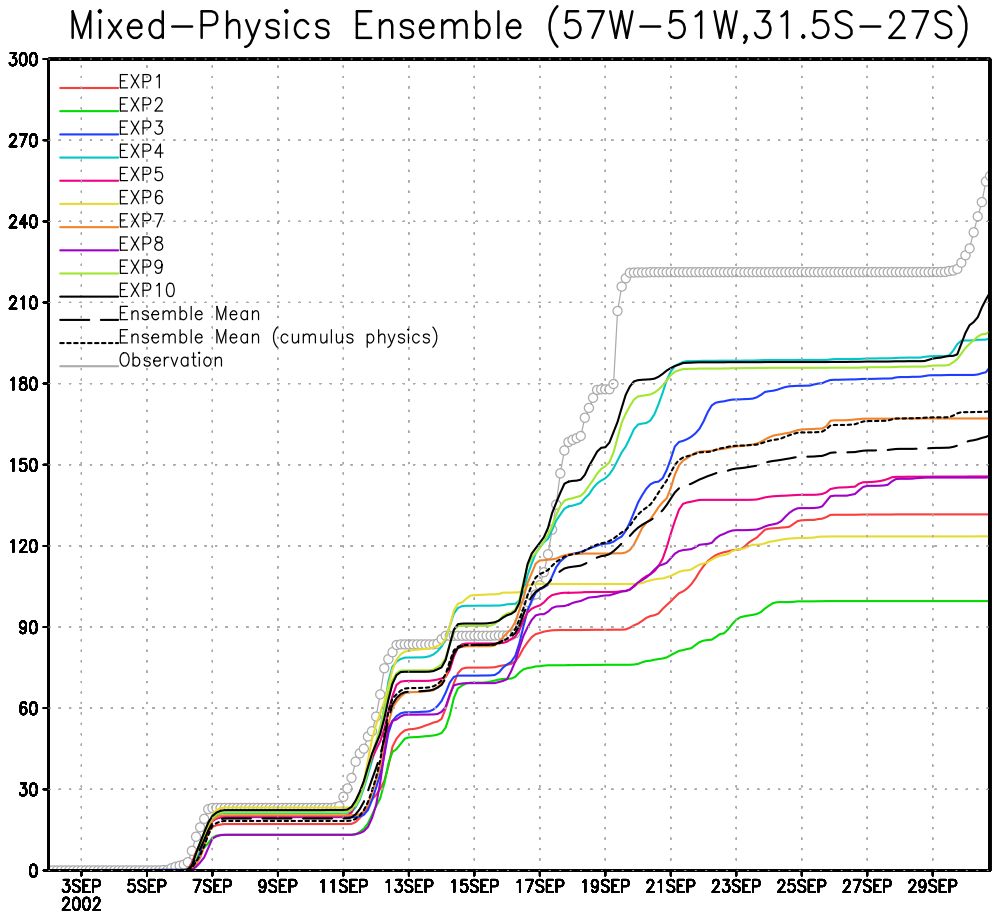

Figure A.3: Same as Fig. A.2 except for comparison of all-physics ensemble mean (long dashed black line) and cumulus-physics ensemble mean (dotted black line). Gray lines with open circles denote observed precipitation.

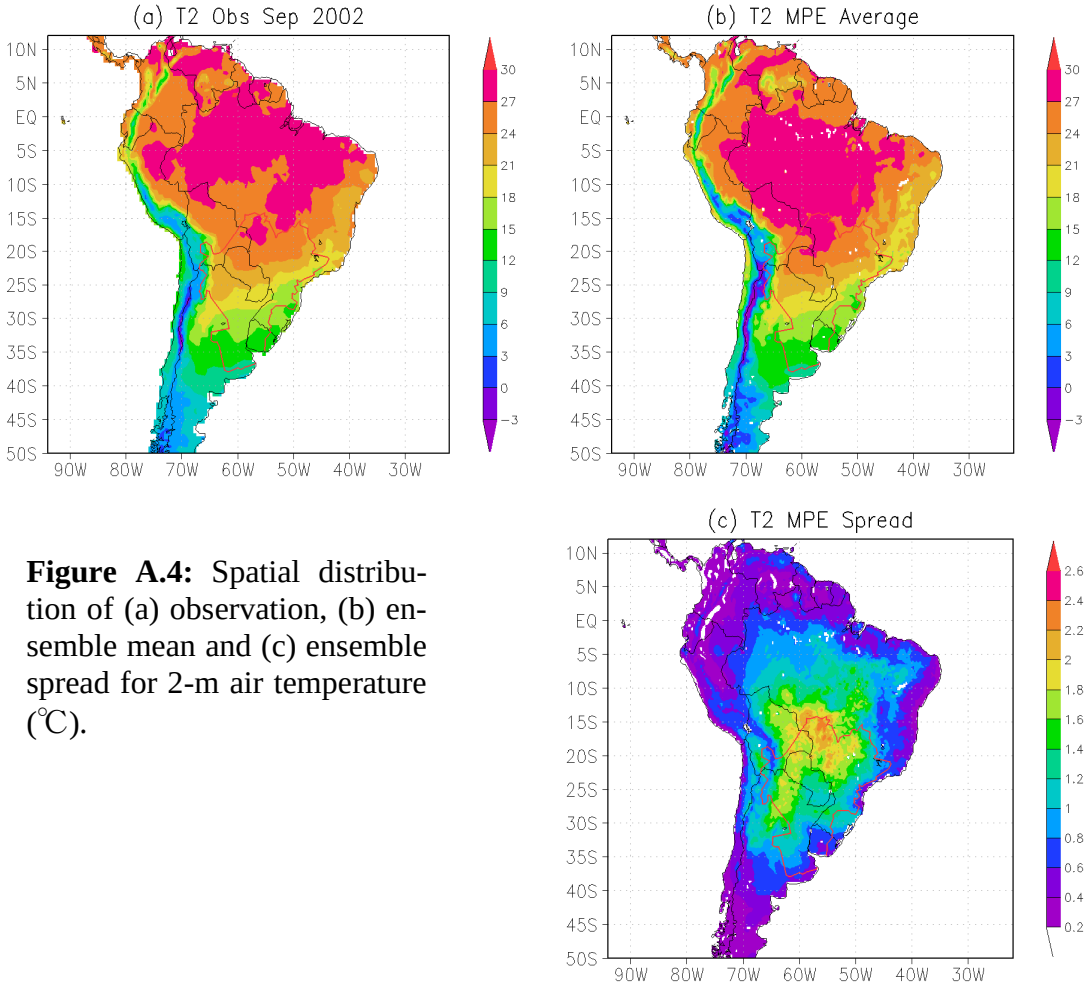

Figure A.4: Spatial distribution of (a) observation, (b) ensemble mean and (c) ensemble spread for 2-m air temperature (℃).

Figure A.4 shows that the central South America region including northern LPB region has much uncertainty in 2-m air temperature simulation. This means that region has the largest difference among the ensemble members. Also, comparison of ensemble spread distribution for 2-m air temperature (Fig. A.4b) with precipitation (Fig. A.1c) shows that there is difference in locations of maximum uncertainties between those two variables. In other words, the maximum uncertainty areas were not collocated. This indicates dependency of the ensemble spread on variables in the study area.

A.4 Summary

A mixed physics ensemble was setup using 10 different physical parameterizations listed in Table 3.1, and applied to ensemble simulations of spring 2002 over South America. First, compared with the observed precipitation for September 2002, ensemble mean precipitation captures well the occurrence of heavy precipitation in the LPB, but the spatial coverage of precipitation is small with a lower maximum value. Despite excessive precipitation along the Andes mountain range, the overall skill of ensemble mean was satisfactory. The MPE comprised of only cumulus schemes showed better skill than the one composed of all the 10 schemes. Second, simulation uncertainties in LPB region were quite low compared with lower latitude regions, and an area of large uncertainties within the LPB was located in southeastern area where broadleaf evergreen forest is located. Third, the region of the largest ensemble spread showed distinct differences between precipitation and 2-m temperature variables, and this indicates that model simulation uncertainties rely on variable types.

Appendix B. Statistical Significance for Results in Chapter 4

In order to test the equality of the two ensemble means, a hypothesis testing was conducted. It is noted that two-tailed tests are more stringent than one-tailed tests (e.g., Figs. 16-18 in Pielke et al. 2001). In Chapter 4, a two-tailed t-test statistic for the difference of CNTL and CROP was calculated using the following formulae:

$$z_n = (M_2 - M_1) / \sqrt{(S_1^2/n_1 + S_2^2/n_2)}$$

where $n_1 = n_2 = 4$ = the number of the ensemble members;

$n = n_1 + n_2 - 1 = 7$ = the degree of freedom (t-distribution Table A3 in Wilks (2006));

C_i = 3-month averaged field of an ensemble member with *current* land-cover data;

F_i = 3-month averaged field of an ensemble member with *future* land-cover data;

M = the ensemble mean ($M_1 = (\sum C_i) / n_1$ and $M_2 = (\sum F_i) / n_2$ for i=1, 2, 3, 4); and

S = the ensemble standard deviation ($S_1 = \sqrt{[\{\sum(C_i - M_1)^2\} / n_1]}$ and

$S_2 = \sqrt{[\{\sum(F_i - M_2)^2\} / n_2]}$ for i=1, 2, 3, 4).

It is assumed that the ensemble members are independent on each other and not paired. The null hypothesis is that there is no statistically significant difference between CNTL and CROP.

Figure B.1 shows the results of a t-test for the 3-month averaged 2-m temperature (Fig. 4.8b), 10-m wind (Fig. 4.9d) and surface precipitation (Fig. 4.14d). Shaded are the grid cells that are statistically significant at a chosen level. Figure B.1a shows that the comparatively strong cooling in the northern LPB is a statistically significant signal at

the 99% level of confidence. This means that if 100 tests are conducted, the true mean accuracy of the system will be located within the confidence interval band in *at least* 99 out of the 100 tests. The relatively weak warming the southern LPB is almost not statically significant at the same level. These results imply that the human land-cover modification in the LPB can counteract with the global warming environment. In particular, the Region II and the southern Paraguay, where evergreen broadleaf forest is assumed to be converted to dry cropland and pasture, would be very resistant to the global warming trend. On the other hand, Fig. B.1b shows that the 10-m wind reduction over the three land cover conversion regions is also a statistically significant signal. The null hypothesis is rejected at the 1% level of significance over all the land-cover conversion regions, i.e. Region I, II and III.

Figure B.1c show that the reduced (increased) precipitation in the northern (southern) LPB is supported by statistical significance. However, the statistical significance is somewhat low compared with 2-m temperature and 10-m wind. This can be attributed to the fact that, in general, precipitation does not necessarily follow Gaussian probability distributions. Nevertheless, statistical significance of the change in surface precipitation due to land cover conversion is over 90%, which seems to be quite acceptable level. While the impact of the land cover change in the LPB on the near-surface temperature is mainly limited within the LPB, the impact of the land cover change in the LPB on the precipitation is not restricted in the interior LPB, and is far beyond the basin. The large statistical significance exists not only over the South Atlantic Ocean (Fig. B.1c), but also near the equator, as indicated by ‘T’ in Fig. 4.12b.

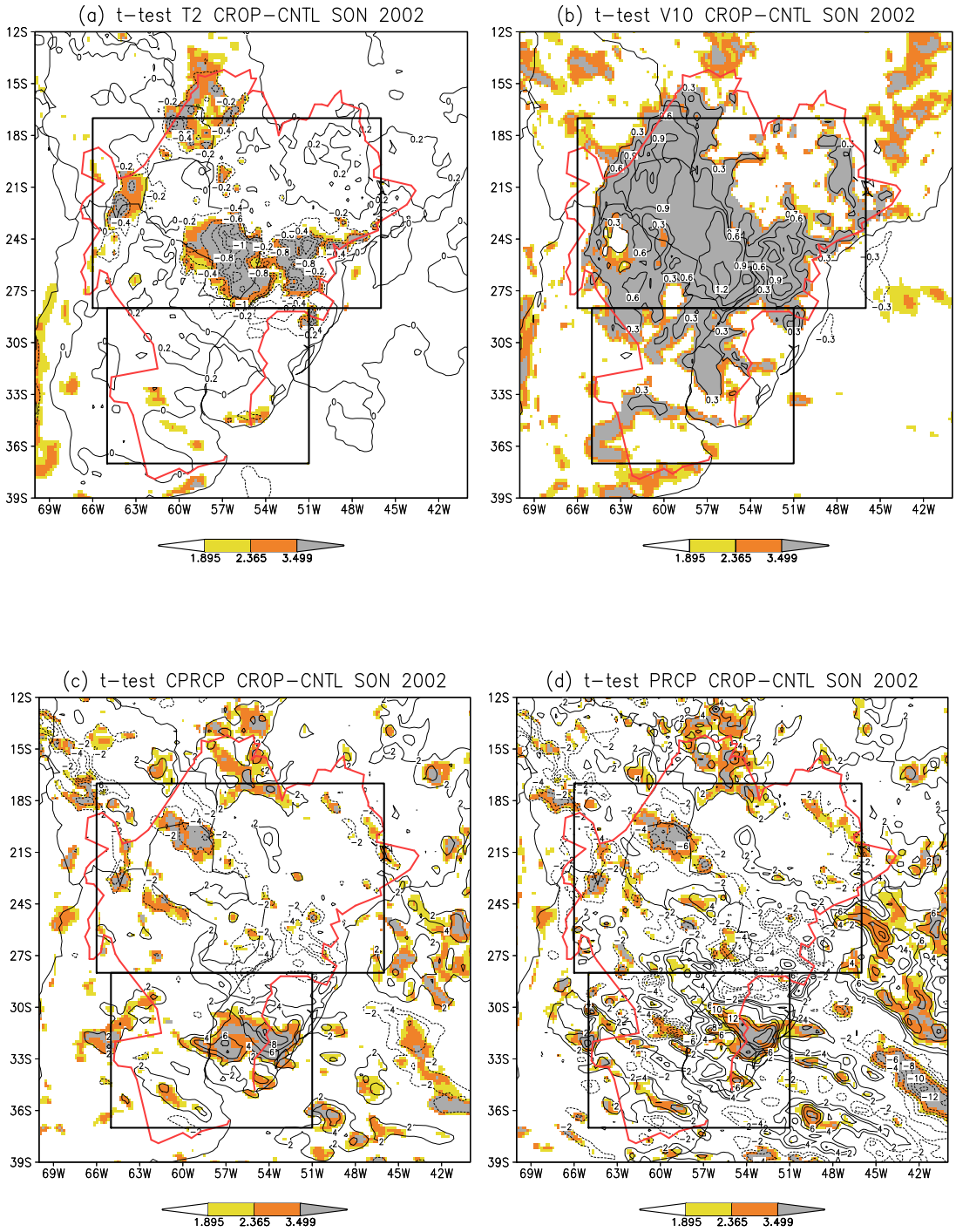

Figure B.1: Statistical significance for difference between the two ensemble means, CNTL and CROP, of (a) 2-m temperature (°C), (b) 10-m wind speed (m s^{-1}), (c) convective precipitation (0.1 mm), (d) total precipitation (0.1 mm), and (e) total precipitation (0.1 mm) in a larger domain. Shaded are the grid cells that are significant at 90, 95 and 99% levels of confidence.

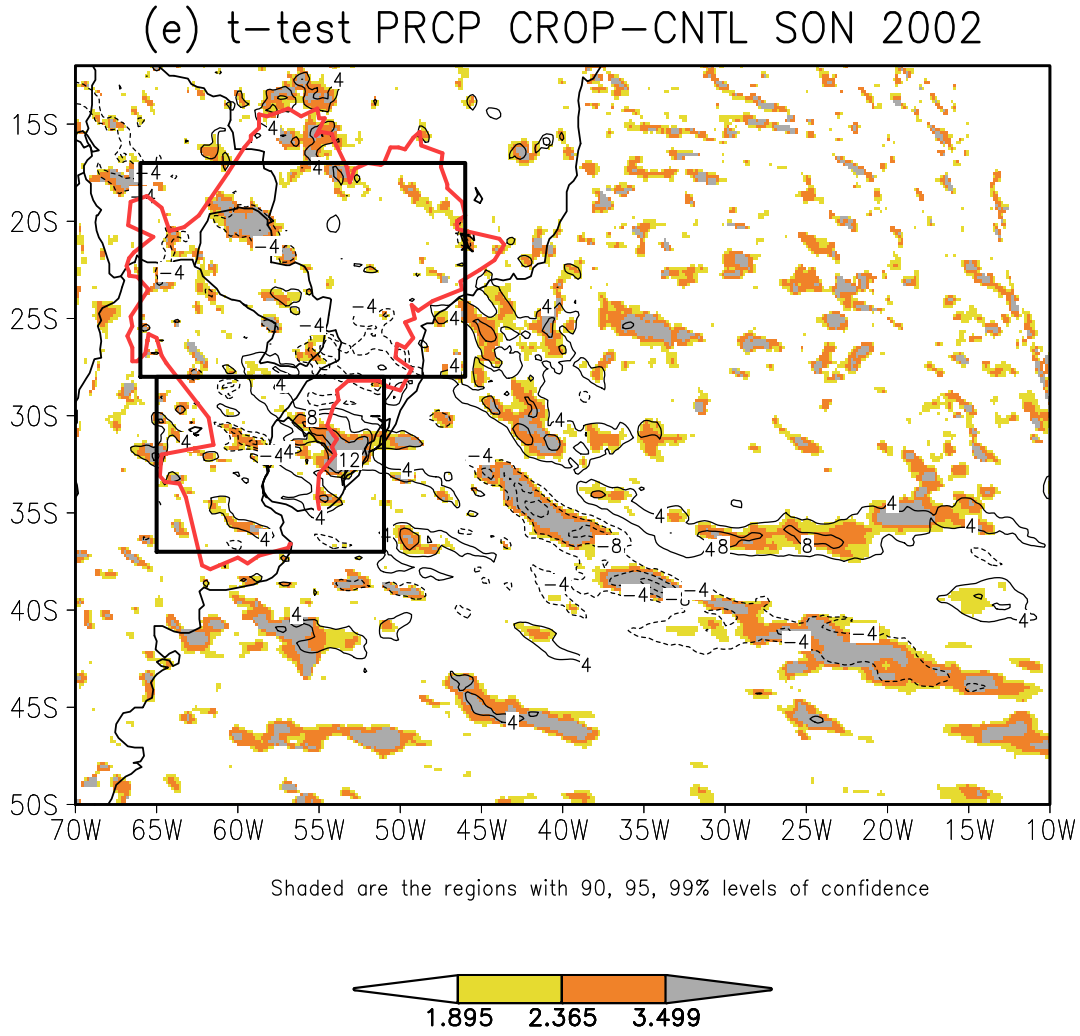

Figure B.1: (Continued.)

Figures B.2 and B.3 show time series of all ensemble members and differences between the two ensemble averages for simulated 2-m temperature (°C) and accumulated precipitation (mm), respectively.

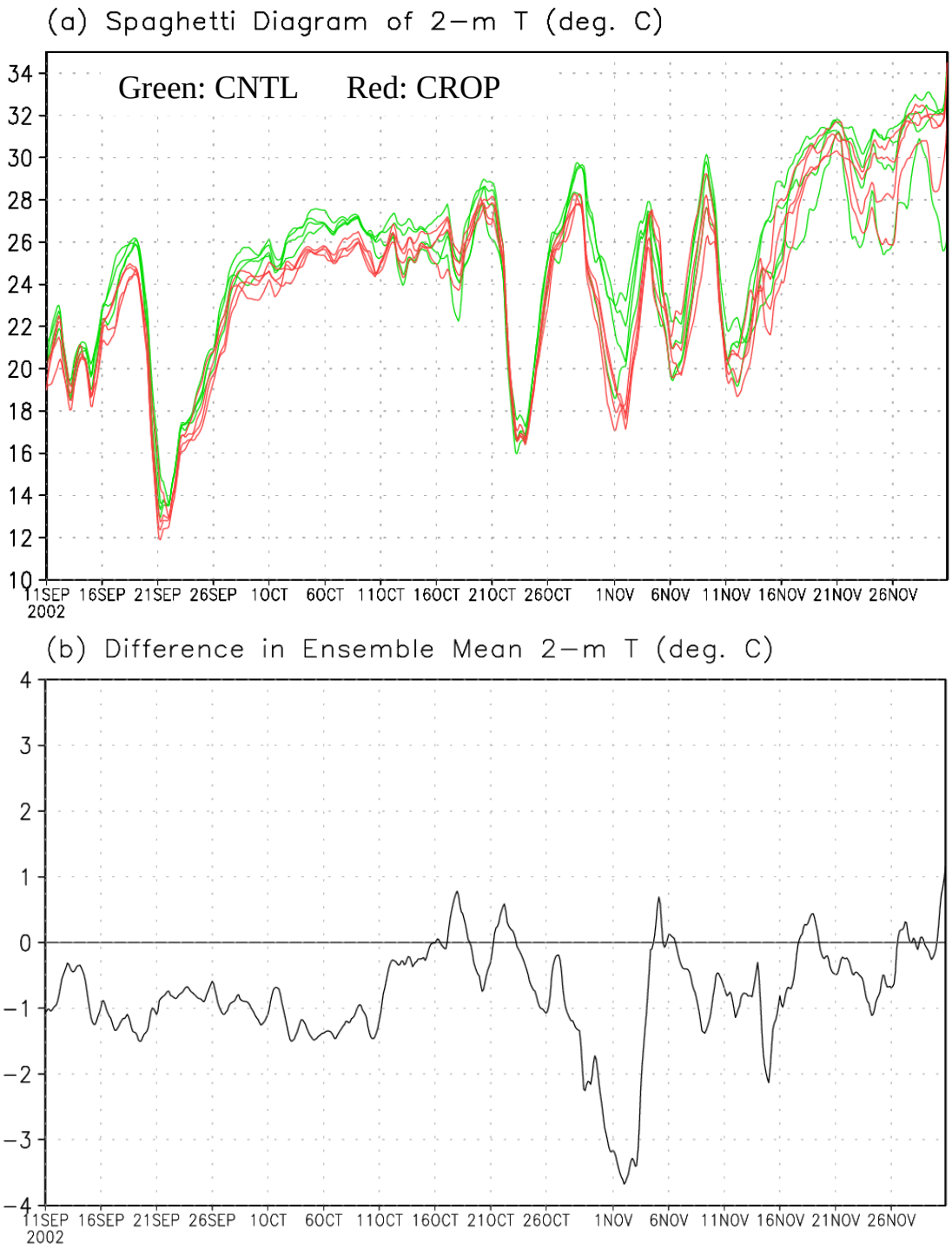

Figure B.2: Time series of 2-m temperature (°C) for (a) each ensemble member over area (58°W-50°W, 27°S-24°S) and (b) difference (CROP – CNTL) in between ensemble averages.

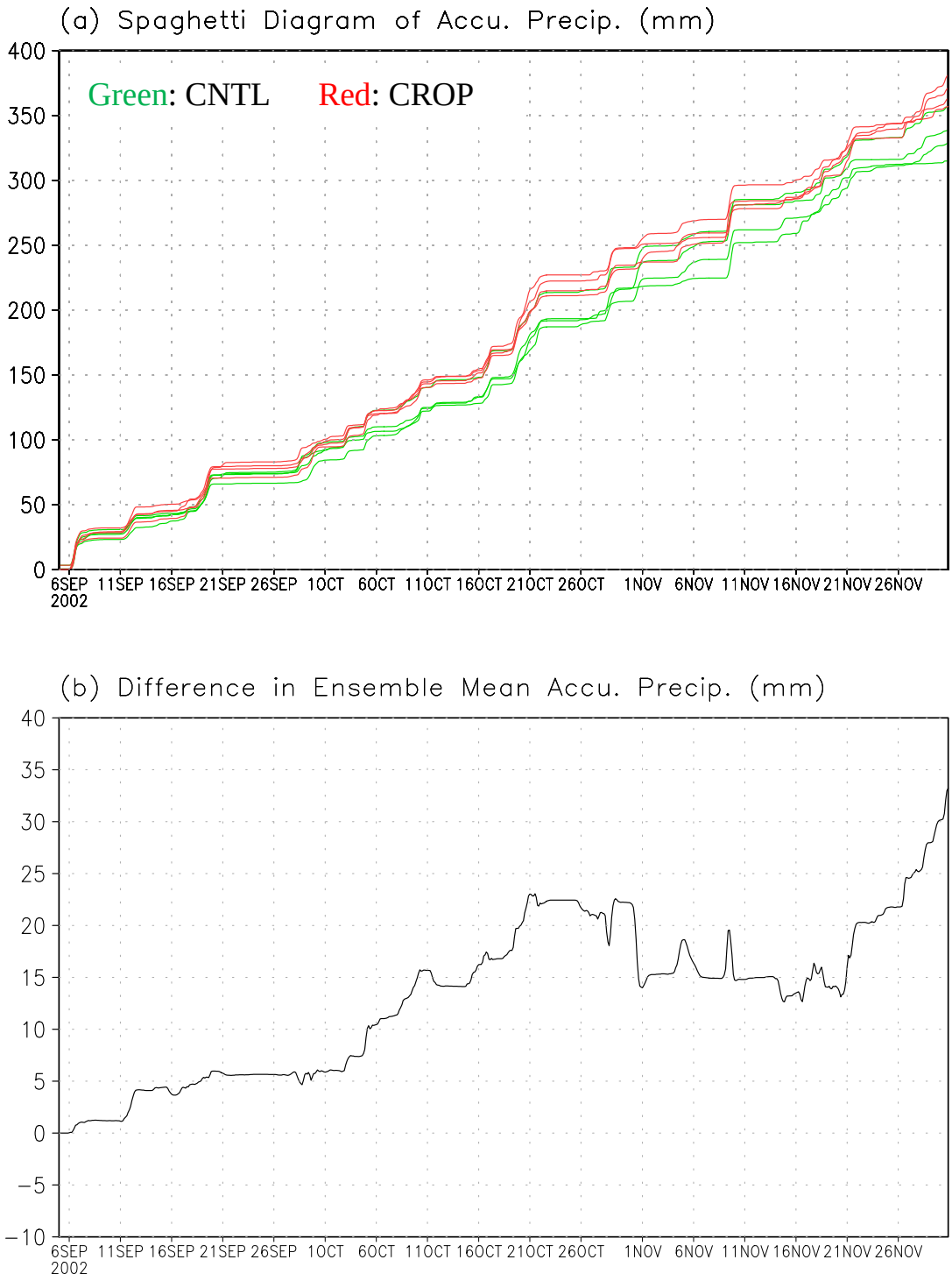

Figure B.3: Time series of accumulated precipitation (mm) for (a) each ensemble member over area (57°W-50°W, 35°S-30°S) and (b) difference (CROP – CNTL) in between ensemble averages.

Bibliography

Alcaraz-Segura, D., J. Paruelo, H. E. Epstein, E. H. Berbery, E. Kalnay, J. Cabello, and E. G. Jobbagy, 2009: Using ecosystem functional types in land-surface modeling to characterize and monitor the spatial and inter-annual variability of vegetation dynamics. *2009 American Geophysical Union Fall Meeting*, 14-18 December 2009, San Francisco, California, USA.

Alcaraz D., J. M. Paruelo, and J. Cabello, 2006: Identification of current ecosystem functional types in the Iberian Peninsula. *Global Ecology and Biogeography,* **15,** 200-212.

Anderson, J. R., Hardy, E. E., Roach J. T., and Witmer, R. E. 1976: A land use and land cover classification system for use with remote sensor data. U.S. Geological Survey Professional Paper 964, 28 pp.

Arritt, R. W. and Coauthors, 2004: Ensemble methods for seasonal limited area forecasts. *20th Conference on Weather Analysis and Forecasting/16th Conference on Numerical Weather Prediction, 10–16 January, Seattle, WA, USA*

Back, L. E., and C. S. Bretherton, 2005: The relationship between wind speed and precipitation in the Pacific ITCZ. *J. Climate*, **18**, 4317-4328.

Baethgen, W., V. Barros, E. Berbery, R. Clarke, H. Cullen, C. Ereño, B. Grassi, D. P. Lettenmaier, R. Mechoso, and P. Silva Dias, 2001: Climatology and hydrology of the Plata Basin, A document of VAMOS Scientific Study Group on the Plata Basin, WCRP/VAMOS. (Available from http://www.clivar.org/publications/wg_reports/vamos/pdf_files/laplata.pdf)

Barlow, M., S. Nigam, and E. H. Berbery, 1998: Evolution of the North American monsoon system. *J. Climate*, **11**, 2238–2257.

Barros, V., M. Gonzalez, B. Liebmann and I. Camilloni, 2000: Influence of the South Atlantic convergence zone and South Atlantic Sea surface temperature on inter-annual summerrainfall variability in Southeastern South America. *Theoretical and Applied Climatology*, **67**, 123-133.

Belward, A. S., J. E. Estes, and K. D. Kline, 1999: The IGBP-DIS global 1-km land-cover data set DISCover: A project overview. *Photogram. Eng. Remote Sens.*, **65**, 1013-1020.

Beltrán-Przekurat, A., R. A. Pielke Sr., J. L. Eastman, and M. B. Coughenour, 2010: Modeling the effects of land-use/land-cover changes on the near-surface atmosphere in southern South America. *International J. Climatology*, To be submitted.

Berbery, E. H., and coauthors, 2005: La Plata Basin (LPB) Contiental Scale Experiment – Implementation Plan. [Available from http://www.eol.ucar.edu/projects/lpb/.]

Berbery, E. H., and E. A. Collini, 2000: Springtime precipitation and water vapor flux over Southeastern South America. *Mon. Wea. Rev.*, **128,** 1328–1346.

Berbery, E. H., and V. R. Barros, 2002: The hydrologic cycle of the La Plata basin in South America. *J. Hydrometeor.*, **3**, 630-645.

Black. T. L., 1994: The new NMC mesoscale Eta model: Description and forecast experiments. *Wea. Forecasting*, **9**, 266-278.

Bluestein, H. B., 1993: *Synoptic–Dynamic Meteorology in Midlatitudes.* Vol 2. Oxford University Press, 594 pp.

Bozzano, B. and Weik, J.H. 1992: El Advance de la Deforestación y el Impacto Económico. Proyecto de Planificación del Manejo de Recursos Naturales. Asunción MAG/GP-GTZ.

Brohan, P., J.J. Kennedy, I. Harris, S.F.B. Tett and P.D. Jones, 2006: Uncertainty estimates in regional and global observed temperature changes: a new dataset from 1850. *J. Geophys. Res.,* **111**, D12106, doi:10.1029/2005JD006548

Cha, D.-H., D.-K. Lee, and Y.-H. Kuo, 2006: An implementation of spectral nudging technique to the WRF model. *7th Annual WRF User's Workshop, 19-22 June 2006, Boulder, Colorado, USA*

Champeaus, J. L., V. Masson, and F. Chauvin, 2005: ECOCLIMAP: a global database of land surface parameters at 1 km resolution. *Meteorol. Appl*., **12**, 29-32.

Chen, F., and J. Dudhia, 2001: Coupling an advanced land-surface/ hydrology model with the Penn State/ NCAR MM5 modeling system. Part I: Model description and implementation. *Mon. Wea. Rev*., **129**, 569–585.

Climate Prediction Center, 2001: U.S. temperature and precipitation trends, http://www.cpc.ncep.noaa.gov/charts.shtml.

Collini, E. A, E. H. Berbery, V. R. Barros, and M. E. Pyle, 2008: How does soil moisture influence the early stages of the South American monsoon?, *J. Climate,* **21**, 195-213.

Davies, H. C., 1976: A lateral boundary formulation for multi-level prediction models. *Q. J. R. Meteorol. Soc.,* **102**, 405-418.

Done, J., L. R. Leung, C. Davis, and B. Kuo, 2005: Understanding the value of high resolution regional climate modeling. Preprints, *Symp. on Living with a Limited Water Supply and the 19th Conf. on Hydrology*, San Diego, CA, Amer. Meteor. Soc., CD-ROM, 5.1.

Doyle, M. E., and V. R. Barros, 2002: Midsummer low-level circulation and precipitation in subtropical South America and related sea surface temperature anomalies in the South Atlantic. *J. Climate,* **15**, 3394-3410.

Dudhia, J., 1989: Numerical study of convection observed during the winter monsoon experiment using a mesoscale two-dimensional model, *J. Atmos. Sci*., **46**, 3077–3107.

Dyer, A. J., and B. B. Hicks, 1970: Flux-gradient relationships in the constant flux layer. *Quart. J. Roy. Meteor. Soc*., **96**, 715–721.

Ek, M. B., K. E. Mitchell, Y. Lin, E. Rogers, P. Grummann, V. Koren, G. Gayno, and J. D. Tarpley, 2003: Implementation of Noah land surface model advances in the National Centers for Environmental Prediction operational Mesoscale Eta Model. *J. Geophys. Res.*, **108**, 8851, doi:10.1029/2002JD003296.

Fall, S., D. Niyogi, A. Gluhovsky, R. A. Pielke Sr., E. Kalnay, and G. Rochon, 2009: Impacts of land use land cover on temperature trends over the continental United States: assessment using the North American Regional Reanalysis. *International J. of Climatology*, doi:10.1002/joc.1996.

Ge, J., J. Qi, and B. Lofgren, 2008: Use of vegetation properties from EOS observations for land-climate modeling in East Africa. *J. Geohys. Res*., **113**, D15101, doi:10.1029/ 2007JD009628.

Grell, G. A., and D. Devenyi, 2002: A generalized approach to parameterizing convection combining ensemble and data assimilation technique. *Geophys. Res. Lett*., **29(14)**, Article 1693

Grell, G. A., J. Dudhia, and D. R. Stauffer, 1994: A description of the fifth-generation Penn State/NCAR Mesoscale Model (MM5). NCAR Tech. Note NCAR/TN-3981STR, 121 pp. [Available from MMM Division, NCAR, P.O. Box 3000, Boulder, CO 80307.]

Hahmann, A. N., and R. E. Dickinson, 1997: RCCM2-BATS model over tropical South America: Application to tropical deforestation. *J. Climate*, 10, 1944-

1964.

Haylock, M. R., and Coauthors, 2006: Trends in total and extreme South American rainfall in 1960–2000 and links with sea surface temperature, *J. Climate,* **19**, 1490-1512.

Hoffman, R. N., and E. Kalnay, 1983: Lagged average forecasting, an alternative to Monte Carlo forecasting. *Tellus,* **35A**, 100-118.

Hong, S.-Y., J. Dudhia, and S.-H. Chen, 2004: A Revised Approach to Ice icrophysical Processes for the Bulk Parameterization of Clouds and Precipitation, *Mon. Wea. Rev*., **132**, 103–120.

Hong, S.-Y., and J.-O. J. Lim, 2006: The WRF Single-Moment 6-Class Microphysics Scheme (WSM6), *J. Korean Meteor. Soc*., **42**, 129–151.

Hong, S.-Y., Y. Noh, and J. Dudhia, 2006: A new vertical diffusion package with an explicit treatment of entrainment processes. *Mon. Wea. Rev*., **134**, 2318-2341.

Huffman, G.J., R.F. Adler, D.T. Bolvin, G. Gu, E.J. Nelkin, K.P. Bowman, Y. Hong, E.F. Stocker, D.B. Wolff, 2007: The TRMM multi-satellite precipitation analysis: quasi-global, multi-year, combined-sensor precipitation estimates at fine scale. *J. Hydrometeor*., **8**, 38-55.

Intergovernmental Panel on Climate Change (IPCC), 2007: *Climate change 2007 – The physical science basis*. Contribution of Working Group I to the Fourth Assessment Report of the IPCC, edited by S. Solomon et al., Cambridge Univ. Press, Cambridge, U. K. [Available at http://ipcc-wg1.ucar.edu/wg1/wg1-report.html.]

Janjic, Z. I., 1990*:* The step-mountain coordinate: physical package. *Mon. Wea. Rev.*, **118**, 1429–1443.

Janjic, Z. I., 1994: The step-mountain eta coordinate model: further developments of

the convection, viscous sublayer and turbulence closure schemes. *Mon. Wea. Rev*., **122**, 927–945.

Janjic, Z. I., 1996: The surface layer in the NCEP Eta Model. *11th Conference on Numerical Weather Prediction, 19–23 August, Norfolk, VA, USA*

Janjic, Z. I., 2000: Comments on "Development and evaluation of a convection scheme for use in climate models", *J. Atmos. Sci*., **57**, 3686.

Janjic, Z. I., 2002: Nonsingular implementation of the Mellor–Yamada level 2.5 scheme in the NCEP Meso model, *NCEP Office Note*, No. 437, 61 pp.

Kain, J. S., and J. M. Fritsch, 1990: A one-dimensional entraining/detraining plume model and its application in convective parameterization, *J. Atmos. Sci*., **47**, 2784–2802.

Kain, J. S., and J. M. Fritsch, 1993: Convective parameterization for mesoscale models: The Kain-Fritcsh scheme. The representation of cumulus convection in numerical models. *Meteor. Monogr.*, No. 24, Amer. Meteor. Soc., 165-170.

Kalnay, E., and Coauthors, 1996: The NCEP/NCAR 40-year reanalysis project. *Bull. Amer. Meteor. Soc.,* **77**, 437–471.

Kurkowski, N. P., D. J. Stensrud, and M. E. Baldwin, 2003: Assessment of implementing satellite-derived land cover data in the Eta Model. *Wea. Forecasting*, **18**, 404-416.

Labraga, J. C., O. Frumento, and M. Lopez, 2000: The atmospheric water vapor cycle in South America and the tropospheric circulation. *J. Climate*, **13**, 1899-1915.

Lapola, D. M., M. D. Oyama, C. A. Nobre, and G. Sampaio, 2008: A new world natural vegetation map for global change studies. *Annals of the Brazilian Academy of Sciences*, **80**, 397-408.

Leung, L. Ruby, J. Done, J. Dudhia, T. Henderson, M. Vertenstein, and B. Kuo, 2005:

Preliminary results of WRF for regional climate simulations. *Workshop on Research Needs and Directions of Regional Climate Modeling Using WRF and CCSM*, Boulder, CO.

Leung, L. Ruby, Y.-H. Kuo, and J. Tribbia, 2006: Research needs and directions of regional climate modeling using WRF and CCSM. Amer. Meteor. Soc., 1747-1751

Lins, H., and J.R. Slack, 1999: Streamflow trends in the United States. *Geophys. Res. Lett.*, **26**, 227-230.

Loveland, T. R., and A. S. Belward, 1997: The IGBP-DIS global 1-km land cover data set, DISCover: First results. *Int. J. Remote Sens.,* **18**, 3291-3295.

Marengo, J. A., W. R. Soares, C. Saulo, and M. Nicolini, 2004: Climatology of the low-level jet east of the Andes as derived from the NCEP-NCAR reanalyses: Characteristics and temporal variability. *J. Climate*, **17**, 2261-2280.

Marland, G., and Coauthors, 2003: The climatic impacts of land surface change and carbon management, and the implications for climate-change mitigation policy. *Climate Policy*, **3**, 149-157.

Marshall, C. H., and R. A. Pielke Sr., L. T. Steyaert, and D. A Willard, 2004: The impact of anthropogenic land-cover change on the Florida Peninsula sea breezes and warm season sensible weather. *J. Climate*, **132**, 28-52.

McAlpine, C. A., J. Syktus, R. C. Deo, P. J. Lawrence, H. A. McGowan, I. G. Watterson, and S. R. Phinn, 2007: Modeling the impact of historical land cover change on Australia's regional climate. *Geophys. Res. Lett.*, **34**, L22711, doi:10.1029/2007GL031524.

Michalakes, J., S. Chen, J. Dudhia, L. Hart, J. Klemp, J. Middlecoff, and W. Skamarock, 2001: Development of a next generation regional weather research and

forecast model. *Developments in Teracomputing: Proceedings of the Ninth ECMWF Workshop on the Use of High Performance Computing in Meteorology*. Eds. Walter Zwieflhofer and Norbert Kreitz. World Scientific, 2001, pp. 269-276.

Miguez-Macho, G., G. L. Stenchikov, and A. Robock, 2005: Regional climate simulations over North America: Interaction of local processes with improved large-scale flow. *J. Climate*, **18**, 1227-1246.

Mlawer, E. J., S. J. Taubman, P. D. Brown, M. J. Iacono, and S. A. Clough, 1997: Radiative transfer for inhomogeneous atmosphere: RRTM, a validated correlated-k model for the longwave. *J. Geophys. Res*., **102** (D14), 16663–16682.

Misra, V., P. A. Dirmeyer, B. P. Kirtman, H.-M. Henry Juang, M. Kanamitsu, 2002: Regional simulation of interannual variability over South America. *J. Geophys. Res*, **107**, D20, 10.1029/2001JD900216.

Narisma, G. T., and A. J. Pitman, 2003: The impact of 200 years of land cover change on the Australian near-surface climate, *J. Hydrometeor*., **4**, 424-436.

Negri, A. J., R. F. Adler, E. J. Nelkin, and G. J. Huffman, 1994: Regional rainfall climatologies derived from Special Sensor Microwave/Imager (SSM/I) data. *Bull. Amer. Meteor. Soc.*, **75,** 1165–1182.

Nobre, C. A., P. J. Sellers, and J. Shukla, 1991: Amazonian Deforestation and Regional Climate Change. *J. of Climate,* **4**, 957–988.

Nuñez, M. N., H. H. Ciapessoni, and A. Rolla, E. Kalnay, and M. Cai, 2008: Impact of land use and precipitation changes on surface temperature trends in Argentina *J. Geophys. Res*, **113**, D06111, doi:10.1029/2007JD008638.

Oleson, K. W., K. L. Driese, J. A. Maslanik, W. J. Emery, and W. A. Reiners, 1997: The sensitivity of a land surface parameterization scheme to the choice of re-

motely sensed land-cover datasets. *Mon. Wea. Rev.*, **125**, 1537-1555.

Paegle, J., C. E. Ereño, and E. A. Collini, 1978: Variaciones diurnas de tormentas y convergencia en la capa lı´mite sobre Argentina. *Meteorologica*, **8/9**, 456–463.

Paruelo, J. M., E. G. Jobbagy, and O. E. Sala, 2001: Current distribution of ecosystem functional types in temperate South America. Ecosystem, 683-698.

Paruelo, J. M., J. P. Guerschman, and S. R. Verón, 2005: Expansión agrícola y cambios en el uso del suelo. *Ciencia Hoy,* **15**(87), 14-23.

Pielke, R. A., 2001: Influence of the spatial distribution of vegetation and soils on the prediction of cumulus convective rainfall. *Rev. Geophys.*, **39**, 151-177.

Pielke, R. A., and Coauthors, 1992: A comprehensive meteorological modeling system – RAMS. *Meteorol. Atmos. Phys.*, **49**, 69-91.

Pielke, R. A., and Coauthors, 2007: An overview of regional land-use and land-cover impacts on rainfall. *Tellus*, **59B**, 587-601.

Pongratz, J., L. Bounoua, R. S. DeFries, D. C. Morton, and L. O. Anderson, W. Mauser, and C. A. Klink, 2006: The impact of land cover change on surface energy and water balance in Mato Grosso, Brazil. *Earth Interaction*, **10**, 1-17.

Raymond, D. J., S. K. Esbensen, M. Gregg, and C. S. Bretherton, 2004: EPIC 2001 and the coupled ocean–atmosphere system of the tropical east Pacific. *Bull. Amer. Meteor. Soc.,* **85,** 1341–1354.

Rojas, M., and A. Seth, 2003: Simulation and sensitivity in a nested modeling system for South America. Part II: GCM boundary forcing. *J. of Climate*, **16**, 2454-2471.

Roy, S. B., G. C. Hurtt, C. P. Weaver, and S. W. Pacala, 2003: Impact of historical land cover change on the July climate of the United States. *J. Geophys. Res., **108*****(D24)***, 4793, doi:10.1029/2003JD003565.

Saurral, R. I., V. R. Barros, and D. P. Lettenmaier, 2008: Land use impact on the Uruguay River discharge, *Geophys. Res. Lett.*, **35**, L12401, doi:10.1029/2008GL033707.

Scepan, J., 1999: Thematic validation of high-resolution gloabal land-cover data sets. *Photogram. Eng. Remote Sens.*, **65**, 1051-1060.

Seth, A., and M. Rojas, 2003: Simulation and sensitivity in a nested modeling system for South America. Part I: Reanalyses boundary forcing. *J. of Climate*, **16**, 2437-2453.

Shi, W., R. W. Higgins, E. Yarosh, and V. E. Kousky, 2000: The annual cycle and variability of precipitation in Brazil. NCEP/Climate Prediction Center ATLAS No. 9. [Available online document available at: http://www.cpc.ncep.noaa.gov/research_papers/ ncep_cpc_atlas/9/.]

Silva, V. B. S., and E. H. Berbery, 2006: Intense rainfall events affecting the La Plata basin. *J. Hydrometeor*., **7**, 769-787.

Skamarock, W. C., J. B. Klemp, J. Dudhia, D. O. Gill, D. M. Barker, W. Wang, and J. G. Powers, 2008: A description of the advanced research WRF version 3. NCAR Tech. Note TN-475, 113 pp.

Soriano, A., and J. M. Paruelo, 1992: Biozones: vegetation units defined by functional characters identifiable with the aid of satellite sensor *images. Global Ecology and Biogeography Letters*, **2**, 82-89.

Stohlgren, T. J., T. N. Chase, R. A. Pielke Sr., T. G. F. Kittel, and J. S. Baron, 1998: Evidence that local land use practices influence regional climate, vegetation, and stream flow patterns in adjacent natural areas. *Global Change Policy*, **4**, 495-504.

Tucci, C. E. M., and R. T. Clarke, 1998: Environmental issues in the La Plata Basin.

Water Resources Development, **14**, 157-174.

Vera, C., and Coauthors, 2006: Toward a unified view of the American monsoon systems, *J. Climate*, **19**, 4977-5000.

von Storch, H., H. Langenberg, and F. Feser, 2000: A spectral nudging technique for dynamical downscaling purposes. *Mon. Wea. Rev*., **128**, 3664- 3673.

Vukicevic, T., and R. M. Errico 1990: The influence of artificial and physical factors upon predictability estimates using a complex limited area model. *Mon. Wea. Rev*., **118**, 1460-1482.

Waldron, K. M., J. Paegle, and J. D. Horel, 1996: Sensitivity of a spectrally filtered and nudged limited area model to outer model options. *Mon. Wea. Rev*., **124**, 529-547.

Werth, D., and R. Avissar, 2002: The local and global effects of Amazon deforestation. *J. Geophys. Res*., **107**, D20, doi:10.1029/2001JD000717.

Wilks, D. S., 2006: *Statistical Methods in the Atmospheric Sciences*, 2nd Ed., Academic Press, 627 pp.

Xie, P., and P. A. Arkin, 1997: Global precipitation: A 17-year monthly analysis based on gauge observations, satellite estimates, and numerical model outputs. *Bull. Amer. Meteor. Soc.*, **78,** 2539–2558.

Yucel, I., 2006: Effects of implementing MODIS land cover and albedo in MM5 at two constrasting U.S. Regions. *J. Hydrometeor*., **7**, 1043-1060.

Zeng, N., and J. D. Neelin, 1999: A land-atmosphere interaction theory for the tropical deforestation problem. *J. Climate*, **12**, 857-872.

Zipser, E. J., D. J. Cecil, C. Liu, S. W. Nesbitt, and D. P. Yorty, 2006: Where are the most intense thunderstorms on Earth? *Bull. Am. Meteorol. Soc.*, **87**, 1057–1071.